UNIVERSITY OF IOANNINA
PHYSICS DEPARTMENT

MSc DISSERTATION

VASILEIOS SOUKERAS

Elastic scattering for the system ^{20}Ne + ^{28}Si at near barrier energies

Supervisor: Athena Pakou
Professor of Physics
University of Ioannina

Ioannina, June 2013

Review Committee

A. Pakou, Professor, Physics Department, University of Ioannina (Supervisor).

E. Stiliaris, Associate Professor, Physics Department, Unversity of Athens.

X. Aslanoglou, Assistant Professor, Physics Department, University of Ioannina.

ΠΑΝΕΠΙΣΤΗΜΙΟ ΙΩΑΝΝΙΝΩΝ
ΤΜΗΜΑ ΦΥΣΙΚΗΣ

ΜΕΤΑΠΤΥΧΙΑΚΗ ΕΡΓΑΣΙΑ

ΒΑΣΙΛΕΙΟΣ ΣΟΥΚΕΡΑΣ

Ελαστική σκέδαση για το σύστημα ^{20}Ne + ^{28}Si σε ενέργειες κοντά στο φράγμα Coulomb

Επιβλέπουσα: ***Αθηνά Πάκου***
Καθηγήτρια Φυσικής
Πανεπιστήμιο Ιωαννίνων

Ιωάννινα, Ιούνιος 2013

Εξεταστική επιτροπή

Α. Πάκου, Καθηγήτρια, Τμήμα Φυσικής, Πανεπιστήμιο Ιωαννίνων (Επιβλέπουσα).

Ε. Στυλιάρης, Αναπληρωτής Καθηγητής, Τμήμα Φυσικής, Πανεπιστήμιο Αθηνών.

Ξ. Ασλάνογλου, Επίκουρος Καθηγητής, Τμήμα Φυσικής, Πανεπιστήμιο Ιωαννίνων.

Acknowledgements

At this point, I would like to thank all of those who have supported and assisted me during my graduate studies.

First of all, my supervisor, Professor of Nuclear Physics A. Pakou, for suggesting the subject, introducing me to the appropriate experimental and theoretical techniques and also for her guidance during my studies.

I would like to extend my sincere thanks to the members of the review committee: Professor A. Pakou, Associate Professor E. Stiliari and Assistant Professor X. Aslanoglou for their useful comments.

Also, I express my gratitude to the members of the Hellenic Institute of Nuclear Physics Professor A. Pakou, Associate Professor E. Stiliari, Lecturer N. Patroni, PhD candidate K. Zerva and my fellow worker Mr. O. Sgouro for their unreserved assistance throughout the experiment.

I would like to express the deepest appreciation to the director of the Heavy Ion Laboratory of University of Warsaw (HIL), Professor K. Rusek, for making available the ICARE facility for the needs of our experiment as well as for his great support and generous hospitality during our stay in Warsaw.

I extend my sincere and warm thanks to: PhD candidate I. Strojek, Dr. A. Trzciska and Dr. E. Piasechi for their great support at the preparation and the performance of the experiment. I would also like to warmly thank the technical staff of HIL for providing the beam and for the support with electronics and the acquisition. Their help was more than useful.

I warmly thank Dr. M. Mazzocco from the University of Padova for his unreserved assistance during the preparation of the experiment and Mr. Massimo Loriggiola from Laboratori Nazionali di Legnaro for providing the silicon targets.

It would be incredible near – sighted of me to neglect Professor K. Rusek and Professor A. Pakou for introducing me in the FRESCO and ECIS calculations.

Moreover, I am thankful to Dr. N. Keeley for the theoretical support.

Also, I would like to thank Associate Professor E. Stiliari and his students M. Mikeli, A. N. Rapsomaniki and M. Zioga for their help with the simulation code GATE.

Last but not least, I thank my beloved parents for their love and unreserved support during my studies.

This work was performed as a part of the postgraduate program that has been co-financed as a part of the **«Scholarship Program by the National Scholarship Foundation, academic year 2011-2012»** by funds of the Operation Program "Education and Lifelong Learning" of the European Social Fund and the National Strategic Reference Framework (NSRF).

Ευχαριστίες

Σε αυτό το σημείο θα ήθελα να ευχαριστήσω όλους όσους με υποστήριξαν και με βοήθησαν κατά την διάρκεια των μεταπτυχιακών μου σπουδών.

Καταρχήν, την επιβλέπουσα της εργασίας, Καθηγήτρια Πυρηνικής Φυσικής Α. Πάκου, για την επιλογή του θέματος, επειδή με εισήγαγε στις κατάλληλες πειραματικές και θεωρητικές τεχνικές και επίσης για την καθοδήγηση κατά την διάρκεια των σπουδών μου.

Θα ήθελα επίσης να εκφράσω τις ειλικρινές μου ευχαριστίες στα μέλη της εξεταστικής επιτροπής: Καθηγήτρια Α. Πάκου, Αναπληρωτή Καθηγητή Ε. Στυλιάρη και Επίκουρο Καθηγητή Ξ. Ασλάνογλου για τα χρήσιμα σχόλια τους.

Επίσης, εκφράζω την ευγνωμοσύνη μου στα μέλη του Ελληνικού Ινστιτούτου Πυρηνικής Φυσικής (ΕΙΠΦ): Καθηγήτρια Α. Πάκου, Αναπληρωτή Καθηγητή Ε. Στυλιάρη, Λέκτορα Ν. Πατρώνη, υποψήφια διδάκτορα Κ. Ζέρβα και τον συμφοιτητή μου Ο. Σγούρο για την αμέριστη υποστήριξη από την αρχή έως το τέλος του πειράματος.

Θα ήθελα να εκφράσω τις βαθιές μου ευχαριστίες στον διευθυντή του Εργαστηρίου Βαρέων Ιόντων του Πανεπιστημίου της Βαρσοβίας, Καθηγητή K. Rusek, για την διάθεση της πειραματικής διάταξης ICARE για τους σκοπούς του πειράματος καθώς και για την μεγάλη υποστήριξη και την ευγενική φιλοξενία κατά την διάρκεια της διαμονής μας στην Βαρσοβία.

Εκφράζω τις ειλικρινές μου και θερμές ευχαριστίες στους: Υποψήφια διδάκτορα I. Strojek, Δρ. A. Trzcinska και Δρ. E. Piasecki για την μεγάλη υποστήριξη στην προετοιμασία και την διενέργεια του πειράματος. Θα ήθελα επίσης να ευχαριστήσω θερμά το τεχνικό προσωπικό του HIL για την παροχή της δέσμης και για την υποστήριξη με τα ηλεκτρονικά και την ανάλυση. Η βοήθειά τους ήταν περισσότερο από χρήσιμη.

Ευχαριστώ θερμά τον Δρ. M. Mazzocco από το Πανεπιστήμιο της Πάδοβα για την αμέριστη βοήθεια κατά την διάρκεια της προετοιμασίας του πειράματος και τον κ. Massimo Loriggiola από το Εθνικό Εργαστήριο του Legnaro της Ιταλίας για την διάθεση των στόχων πυριτίου.

Δεν θα μπορούσα να παραλείψω τον Καθηγητή K. Rusek και την Καθηγήτρια Α. Πάκου που με εισήγαγαν στους υπολογιστικούς κώδικες FRESCO και ECIS.

Επιπλέον, είμαι ευγνώμων στον Δρ. N. Keeley για την θεωρητική υποστήριξη.

Επίσης, θα ήθελα να ευχαριστήσω τον Αν. Καθηγητή Ε. Στυλιάρη και τους φοιτητές του Μ. Μικέλη, Α.-Ν. Ραψωμανίκη και Μ. Ζιόγα για την βοήθειά τους με τον κώδικα προσομοιώσεων GATE.

Τελευταία αλλά όχι λιγότερο, ευχαριστώ τους αγαπημένους μου γονείς για την αγάπη και αμέριστη στήριξη τους καθόλη την διάρκεια των σπουδών μου.

Η ολοκλήρωση της εργασίας αυτής έγινε στο πλαίσιο της υλοποίησης του μεταπτυχιακού προγράμματος το οποίο συγχρηματοδοτήθηκε μέσω της Πράξης **«Πρόγραμμα χορήγησης υποτροφιών Ι.Κ.Υ. με διαδικασία εξατομικευμένης αξιολόγησης ακαδ. έτους 2011-2012»** από πόρους του Ε.Π. «Εκπαίδευση και Δια Βίου Μάθηση» του Ευρωπαϊκού Κοινωνικού Ταμείου (ΕΚΤ) και του ΕΣΠΑ, του 2007-2013».

Contents

Abstract

This Master dissertation refers to the study of the ^{20}Ne + ^{28}Si elastic scattering at near barrier energies, and includes a description of the experimental setup and the analysis of experimental data at three energies, namely 42.5, 52.3 and 70.0 MeV.

The experimental setup was visualized in ICARE facility of the Heavy Ion Laboratory in the University of Warsaw. ICARE includes two rotating platforms and several rings for setting up numerous detectors or telescopes. Four telescopes, comprised of two parts, were used in the present experiment. The first part is a gas detector (C_4H_{10}) with thickness 47mm and a gas pressure of 11.25 Torr, while the second one is a Silicon detector with a thickness of 500μm. The first part of the telescope absorbs a part of the recoil ions, allowing a Z separation via the conventional ΔE-E technique. Furthermore, several single silicon detectors, 40μm thick, were placed at the more backward angles, while two of them were set at forward symmetrical positions, $\pm 20^{o}$, serving as flux monitors and for correcting beam misalignments. The ^{28}Si targets with thicknesses of ~ 132 μg/cm^2 and ~ 200 μg/cm^2 were set perpendicular to the beam and were bombarded by a ^{20}Ne beam delivered by the U-200P Cyclotron.

The energy calibration for the detectors and the telescopes was based on measurements via an ^{241}Am source and a pulser. Also, the solid angles of the detectors were determined by the known activity of ^{241}Am source as well as through a Monte – Carlo simulation using the program GATE. The data analysis was performed using the program PAW while, the identification of the elastic channel was performed via the ΔE-E technique, taking into account the kinematics of the colliding ions and the energy losses, using the programs LISE++ and NRV.

The theoretical analysis of the data was performed in the optical model framework. Two macroscopic potentials of Woods – Saxon type were adopted, one with a deep and one with a shallow depth for the real part taking into account as initial values the parameters obtained by the Lee – Chan and the Christensen potential, respectively. A third microscopic potential was also adopted taking into account the BDM3Y1 interaction. In all three cases, the imaginary part was described by a Woods – Saxon form factor. For the easiness of the reader the BDM3Y1 interaction was also parameterized by a Woods – Saxon form factor. The data were described adopting the same optical potential for all energies but with small variations, mainly at the imaginary part of it. Also, as to determine the sensitive radial range, where the deep or the shallow potential is unique, the “Crossing point method” was applied.

The main conclusion of the analysis is that the experimental cross sections at backward angles and at near barrier energies, even with a heavy projectile like ^{20}Ne, present an anomalous increase with oscillating trend.

Two macroscopic and one microscopic potential were also deduced, by fitting adequately well the experimental data. However, the most appropriate were chosen to be the shallow depth macroscopic potential and the microscopic one – BDM3Y1 interaction, the last giving by far the appropriate oscillating phase at least for the data at 52.3 MeV.

Finally, Coupled Reaction Channels calculations, performed by Nick Keeley, present evidence that the ^{8}Be – elastic transfer process from ^{28}Si to ^{20}Ne is the main mechanism to produce the oscillatory structure of the data.

Περίληψη

Η παρούσα μεταπτυχιακή εργασία αναφέρεται στην μελέτη της ελαστικής σκέδασης για το σύστημα ^{20}Ne + ^{28}Si σε ενέργειες κοντά στο φράγμα Coulomb, περιλαμβάνοντας την περιγραφή της πειραματικής διαδικασίας και την ανάλυση των πειραματικών δεδομένων στις ενέργειες 42.5, 52.3 και 70.0 MeV.

Το πείραμα έλαβε χώρα στην πειραματική διάταξη ICARE του Εργαστηρίου Βαρέων Ιόντων του Πανεπιστημίου της Βαρσοβίας. Το ICARE περιλαμβάνει δύο περιστρεφόμενες πλατφόρμες και αρκετούς δακτυλίους κατάλληλους για την τοποθέτηση πλήθους ανιχνευτών ή τηλεσκοπίων. Στο συγκεκριμένο πείραμα χρησιμοποιήθηκαν τέσσερα τηλεσκόπια, τα οποία αποτελούνται από δύο μέρη. Το πρώτο μέρος είναι ο ανιχνευτής αερίου (ισοβουτάνιο) με πάχος 47 χιλιοστά και πίεση αερίου 11.25 Torr, ενώ το δεύτερο μέρος είναι ένας ανιχνευτής πυριτίου πάχους 500 μικρομέτρων. Το πρώτο μέρος του τηλεσκοπίου απορροφά ένα μέρος της ενέργειας του διερχόμενου σωματίου, επιτρέποντας έτσι τον διαχωρισμό των σωματίων με βάση τον ατομικό τους αριθμό, σύμφωνα με την γνωστή τεχνική ΔΕ-Ε. Επιπλέον, αρκετοί ανιχνευτές πυριτίου, πάχους 40 μικρομέτρων, τοποθετήθηκαν σε μεγάλες γωνίες, ενώ δύο από αυτούς τοποθετήθηκαν σε συμμετρικές θέσεις, στις μπροστινές γωνίες ±20^{o}, λειτουργώντας ως εργαλείο υπολογισμού της ροής της δέσμης και διόρθωσης τυχόν ασυμμετρίας της. Οι στόχοι πυριτίου, πάχους περίπου 132 και 200 μικρογραμμαρίων ανά τετραγωνικό εκατοστό αντίστοιχα, τοποθετήθηκαν κάθετα στην πορεία της δέσμης ^{20}Ne και βομβαρδίστηκαν από αυτήν. Η δέσμη ήταν διαθέσιμη από το Κυκλοτρόνιο U-200P του εργαστηρίου της Βαρσοβίας.

Η ενεργειακή βαθμονόμηση για τους ανιχνευτές και τα τηλεσκόπια βασίστηκε σε μετρήσεις με μια ραδιενεργή πηγή ^{241}Am και μία παλμογεννήτρια. Επίσης οι στερεές γωνίες των ανιχνευτών προσδιορίστηκαν χρησιμοποιώντας την ανωτέρω πηγή γνωστής ενεργότητας αλλά, και μια Monte – Carlo προσομοίωση χρησιμοποιώντας το πρόγραμμα GATE. Η ανάλυση των πειραματικών δεδομένων έγινε με το πρόγραμμα PAW ενώ, η ταυτοποίηση του ελαστικού καναλιού επετεύχθη με την χρήση της τεχνικής ΔΕ-Ε, λαμβάνοντας υπόψη της κινηματικές των συγκρουόμενων σωματιδίων και τις απώλειες ενέργειας μέσα στον στόχο ή στον ανιχνευτή, χρησιμοποιώντας τα προγράμματα LISE++ και NRV.

Η θεωρητική ανάλυση των δεδομένων πραγματοποιήθηκε στα πλαίσια του οπτικού μοντέλου. Στα πλαίσια αυτά υιοθετήθηκαν δύο μακροσκοπικά δυναμικά τύπου Woods – Saxon, ένα με μεγάλο και ένα με μικρό βάθος του πραγματικού μέρους του δυναμικού, λαμβάνοντας υπόψη ως αρχικές τιμές τις παραμέτρους που προέκυψαν από το δυναμικό Lee – Chan και το δυναμικό Christensen, αντίστοιχα. Υιοθετήθηκε επίσης ένα τρίτο μικροσκοπικό δυναμικό λαμβάνοντας υπόψη την αλληλεπίδραση BDM3Y1. Και στις τρεις περιπτώσεις το φανταστικό μέρος του

δυναμικού περιγράφηκε από ένα συντελεστή τύπου Woods – Saxon. Για ευκολία του αναγνώστη η αλληλεπίδραση BDM3Y1 παραμετροποιήθηκε από ένα συντελεστή τύπου Woods – Saxon. Θα πρέπει να τονιστεί, ότι τα πειραματικά δεδομένα περιγράφηκαν υιοθετώντας σε όλες τις ενέργειες το ίδιο οπτικό δυναμικό αλλά, με μικρές αλλαγές όπου ήταν απαραίτητο, κυρίως όμως στο φανταστικό μέρος του δυναμικού. Τέλος, εφαρμόστηκε η "μέθοδος του σημείου τομής'' στα πλαίσια του προσδιορισμού της ακτινικής περιοχής όπου το βαθύ ή το ρηχό δυναμικό είναι μοναδικό.

Το βασικό συμπέρασμα της ανάλυσης είναι ότι οι πειραματικές ενεργές διατομές στις μεγάλες γωνίες και σε ενέργειες κοντά στο φράγμα Coulomb, ακόμα και με μία δέσμη βαρέων ιόντων όπως είναι το ^{20}Ne, παρουσιάζει μια ανώμαλη αύξηση με παράλληλη τάση δημιουργίας διακυμάνσεων.

Ένα μικροσκοπικό και δύο μακροσκοπικά δυναμικά προέκυψαν μετά από μια αρκετά καλή προσαρμογή στα πειραματικά δεδομένα. Παρόλα αυτά ως καταλληλότερα προτείνονται, το δυναμικό Woods-Saxon με μικρό βάθος του πραγματικού μέρους καθώς και το μικροσκοπικό δυναμικό που στηρίζεται στην αλληλεπίδραση BDM3Y1. Το τελευταίο παρουσιάζει μακράν την καταλληλότερη φάση στις διακυμάνσεις που εμφανίζονται στις μεγάλες γωνίες, τουλάχιστον στα δεδομένα που έχουμε στην ενέργεια των 52.3 MeV.

Τέλος, πραγματοποιήθηκαν από τον Nick Keeley, υπολογισμοί που στηρίζονται στην τεχνική των συζευγμένων καναλιών αντιδράσεων. Οι συγκεκριμένοι υπολογισμοί αποδεικνύουν ότι η σύζευξη στο ελαστικό κανάλι, αντιδράσεων μεταφοράς είναι σημαντική και ιδιαίτερα η σύζευξη με την ελαστική αντίδραση μεταφοράς όπου ένας ολόκληρος πυρήνας ^{8}Be μεταφέρεται από το στόχο ^{28}Si στο βλήμα ^{20}Ne είναι ο βασικός μηχανισμός ερμηνείας των διακυμάνσεων στην πειραματική ενεργό διατομή.

Introduction

This work is part of the curriculum of the Postgraduate Program of the Department of Physics, University of Ioannina. The research area belongs to the basic direction of Nuclear Physics and in particular on the subject of elastic scattering for determining the optical potential.

Research for the optical nuclear potential at near Coulomb barrier energies has been popular for many years in the Nuclear Physics community[1-4]. The optical model is a simple model with an impressive success in the last six decades and it is able to give precision fits to elastic scattering cross sections[2,5-9], polarizations[10,11], reaction cross sections[12-14] and also total cross sections[2,10]. In the optical model framework, both macroscopic and microscopic potentials have been used to describe the real and the imaginary part of the potential. In the microscopic approach the potential is obtained by assuming a nucleon-nucleon effective interaction, while in the macroscopic approach we take into account the nucleus as a whole system. Into this content, elastic scattering of heavy ions is the main tool for investigating the optical potential.

The team of the Nuclear Physics Laboratory (NPL) at the Physics Department of the University of Ioannina in recent years is dealing with the optical potential of weakly bound nuclei at near barrier energies[15-31]. While such studies are still in progress, the interest of the group is focused also in projectiles with a clustering structure. In particular, the elastic scattering of systems with a cluster structure is very interesting, as the oscillatory pattern together with a rise of the cross section, observed at backward angles, present a challenge to different models of the underlying mechanism[4]. It should be noted that, the clustering (with hierarchy[32]: α, ^{8}Be, ^{12}C e.t.c.) is a very important aspect in the structure of nuclei with a prominent impact on the genesis of heavier systems. Moreover, the excited state of ^{12}C, known as the “Hoyle state”, continues to be a challenge in nuclear physics[33-35]. On the other hand, the main mechanism responsible for the rising and the oscillatory behavior at backward angles in elastic scattering involving nuclei with clustering structure, by itself attracts the interest of the community as the subject is still open. Several approaches have been proposed in order to interpret this type of anomaly. Especially at higher energies, a semiclassical approach was introduced and it appears as an interference phenomenon between near-side and far-side scattering[7,36-40]. The near-side trajectories correspond to a repulsive potential or a reflection while the far-side ones correspond to attractive interactions and diffractions[40]. Furthermore, a comprehensive analysis was also performed by W. von Oertzen et al. assuming molecular orbits and alpha – clustering for the involved nuclei[41-43]. Nevertheless, at near barrier energies, some other mechanisms based on reaction couplings, nucleus or elastic transfer and anti-symmetrization effects may be more prominent[8,32,44-49].

Especially for projectiles like ^{12}C and ^{16}O, due to alpha clustering, coupling effects to the elastic scattering are significant and appear as an increase in cross sections at backward angles, which for projectiles with a simple structure is not observable[4,6-8,32,50-56]. Into this content, in order to describe the oscillatory pattern and the cross section rise at systems with projectiles like ^{12}C and ^{16}O, several potentials were adopted such as the Lee – Chan[51,57-58], the Kobos – Satchler[7] and the Ginocchio potential[9]. It should be mentioned, that in some potentials, like the Kobos – Satchler, some supplementary surface terms, besides the volume terms, have also been taken into account, to simulate couplings to peripheral reaction mechanisms like nucleon, nucleus or elastic transfer[45,46,49].

Coupling effects due to alpha clustering structure of the target are also significant. In that case, it is known that there is a limit on Z (Z≥20) where this anomaly stops to exist[4,59]. So, the main question is if the increase of cross section at backward angles is persistent for heavier projectiles.

Considering all the above and as the team of the Nuclear Physics Laboratory (NPL) is dealing with such issues[15-30], it was proposed the investigation of the elastic scattering of the system ^{20}Ne + ^{28}Si at three near barrier energies, namely 42.5, 52.3 and 70.0 MeV. The ^{20}Ne nucleus is heavier than ^{12}C and ^{16}O and the effect of its cluster structure may not be as strong. So the question is if the increase of cross sections at backward angles is persistent for ^{20}Ne. The experimental data were collected in Heavy Ion Laboratory, University of Warsaw[60-61] while, the analysis of the data was completed at the NPL – Ioannina[15]. This work includes:

- A chapter with the theoretical background, necessary for the theoretical analysis (Chapter 1).
- The description of the experimental setup (Chapter 2).
- The data reduction (Chapter 3) and in particular the energy calibration (3.1), the identification of the reaction channels (3.2) and the determination of the cross sections (3.3).
- The theoretical analysis (Chapter 4) in the optical model framework (4.1-4.3) adopting a microscopic and two macroscopic potentials, one with a deep and one with a shallow depth, as well as some CRC calculations performed by Nick Keeley in the CRC framework[62-63] (4.4).
- The conclusions (Chapter 5).

This work also contains an appendix with:

- the error calculation of σ/σ_{Ruth} ratio,
- a Monte Carlo simulation[64-66] for the solid angle determination,
- some information about the ECIS code[67] and
- tables related to the platform and energy calibration as well as the identification of the reaction channels.

1. Theory

1.1. Elastic scattering

Scattering theory is the standard tool in the basic direction of Nuclear Physics. It is known that several discoveries in Nuclear Physics have been performed via scattering experiments. In that process, a beam of particles is scattered from a target with possible outcomes the Elastic scattering, the Inelastic scattering and the absorption. This dissertation focuses on Elastic scattering in which energy, momentum and particle number are conserved while, on inelastic scattering only the momentum is conserved in general.

Scattering is characterized by the differential and the total cross section. The differential cross section is given as:

$$\frac{d\sigma}{d\Omega} = \left| f(\theta,\phi) \right|^2 \tag{1.1}$$

where *f(*θ,ϕ*)* is the scattering amplitude while, total cross section is given by the formula:

$$\sigma = \int \frac{d\sigma}{d\Omega} d\Omega = \int_0^{2\pi} d\phi \int_0^{\pi} \frac{d\sigma}{d\Omega} \sin\theta d\theta \tag{1.2}$$

The most famous classical scattering phenomenon is the Coulomb scattering. Assuming the Schrödinger equation and the wavefunction for a Coulomb potential:

$$\left[-\frac{\hbar^2}{2m}\nabla + \frac{Z_1 Z_2 e^2}{r} \right] \Psi(r) = E\Psi(r) \tag{1.3}$$

and

$$\Psi = e^{ikz} + \frac{f(\theta,\phi) e^{ik'r}}{r} \tag{1.4}$$

where Z_1, Z_2 are the atomic number of the projectile and the target, e the charge of the proton, m the mass of the projectile, Ψ the wavefunction, E>0 the center of mass energy and k, k' the incident and scattering wavenumbers, it is possible to lead to the Rutherford cross section. The *f(*θ,ϕ*)* quantity, applied the Born approximation, behave as:

$$f(\theta,\phi) = -\frac{2m}{\hbar^2}\frac{1}{q}\int_0^{\infty} V(r)\, r \sin(qr) dr \Rightarrow \tag{1.5}$$

$$\Rightarrow f(\theta,\phi) = -\frac{2m}{\hbar^2}\frac{1}{q}\int_0^{\infty} \frac{Z_1 Z_2 e^2}{r}\, r \sin(qr) dr \Rightarrow \tag{1.6}$$

$$\Rightarrow f(\theta,\phi) = -\frac{2mZ_1Z_2e^2}{\hbar^2}\frac{1}{q}\int_0^\infty \sin(qr)dr \qquad (1.7)$$

where

$$q = k - k' \ , \quad |k| = |k'| \qquad (1.8)$$

Using the integral:

$$\int_0^\infty e^{-ar}\sin(qr)dr \xrightarrow{\alpha\to 0} \frac{1}{q} \qquad (1.9)$$

the formula (1.7) can be written as:

$$f(\theta,\phi) = -\frac{2mZ_1Z_2e^2}{\hbar^2}\frac{1}{q^2} \qquad (1.10)$$

On the other hand, the $|q^2|$ quantity can be written as:

$$|q^2| = (k-k')(k-k') = (k')^2 + k^2 - 2k\cdot k' \Rightarrow \qquad (1.11)$$

$$\Rightarrow |q^2| = 2k^2(1-\cos\theta) \Rightarrow 4k^2\sin^2\frac{\theta}{2} \qquad (1.12)$$

where θ is the scattering angle.
Then, the scattering amplitude is given by the following formula:

$$f(\theta) = -\frac{2mZ_1Z_2e^2}{4k^2\hbar^2\sin^2\frac{\theta}{2}} \qquad (1.13)$$

Finally, the Rutherford cross section is given by the formula below:

$$\frac{d\sigma}{d\Omega} = |f(\theta,\phi)|^2 = \left(\frac{Z_1Z_2e^2}{4E}\right)^2 \frac{1}{\sin^4\left(\theta/2\right)} \qquad (1.14)$$

where the energy *E* is given as:

$$E = \frac{\hbar^2k^2}{2m} \qquad (1.15)$$

In a quantum mechanical description[68], the elastic scattering cross section may be calculated from an optical potential V(r) by solving the Schrödinger equation:

$$\nabla^2\Psi(r,\theta,\phi) + \frac{2m}{\hbar^2}(E - V(r))\Psi(r,\theta,\phi) = 0 \qquad (1.16)$$

assuming the wavefunction (1.4). It is important to note that, if the potential V(r) is real, only elastic scattering can take place.

The solution of eq. (1.16) is given by the formula:

$$\Psi(r,\theta,\phi)=\sum_{L=0}^{\infty}a_L R_L(r)Y_{L,m}(\theta,\phi) \tag{1.17}$$

where α_L is the amplitude of L^{th} partial wave and L is the orbital angular momentum quantum number. Considering system independence of the azimuthal angle ϕ, only spherical harmonics with m=0 are involved. The spherical harmonic $Y_{L0}(\phi)$ is an eigenfunction of the angular part of eq. (1.16) with eigenvalue L(L+1) so, the radial wavefunction is given by the equation:

$$\frac{\hbar^2}{2m}\left[\frac{1}{r^2}\frac{d}{dr}r^2\frac{d}{dr}-\frac{L(L+1)}{r^2}\right]R_L(r)+V(r)R_L(r)=ER_L(r) \tag{1.18}$$

Define as:

$$u_L(r)=rR_L(r) \tag{1.19}$$

The equation (1.18) could be written as:

$$\frac{d^2u_L(r)}{dr^2}-\left[\frac{L(L+1)}{r^2}+\frac{2m}{\hbar^2}V(r)-k^2\right]u_L(r)=0 \tag{1.20}$$

where:

$$k^2=\frac{2mE}{\hbar^2} \tag{1.21}$$

In an asymptotic region ($r\to\infty$), the differential equation (1.20) leads to the following simple second – order differential equation:

$$\frac{d^2u_L(r)}{dr^2}-k^2u_L(r)=0 \tag{1.22}$$

The solution for $r\to\infty$ is written as:

$$u_L(r)\to A_L\sin\left(kr-\frac{L\pi}{2}\right)+B_L\cos\left(kr-\frac{L\pi}{2}\right) \tag{1.23}$$

or

$$u_L(r)\to C_L\sin\left(kr-\frac{L\pi}{2}+\delta_L\right) \tag{1.24}$$

where A_L, B_L and C_L are constants and δ_L is the phase shift. Taking into consideration all the above, the eq. (1.17) may be written as:

$$\Psi(r,\theta)\xrightarrow{r\to\infty}\sum_{L=0}^{\infty}a_L'Y_{L,0}(\theta)\frac{1}{r}\sin\left(kr-\frac{L\pi}{2}+\delta_L\right) \tag{1.25}$$

where the α_L' quantity can be determined as:

$$a_L'=i^Le^{i\delta_L}\sqrt{4\pi(2L+1)} \tag{1.26}$$

The scattering amplitude is given by the formula:

$$f(\theta)=\frac{\sqrt{4\pi}}{2ik}\sum_{L=0}^{\infty}\sqrt{2L+1}\left(e^{2i\delta_L}-1\right)Y_{L0}(\theta)\Rightarrow \quad (1.27)$$

$$\Rightarrow f(\theta)=\frac{\sqrt{4\pi}}{k}\sum_{L=0}^{\infty}Y_{L0}(\theta)\left(\sqrt{2L+1}\right)e^{i\delta_L}\sin\delta_L \quad (1.28)$$

and the differential scattering cross section:

$$\frac{d\sigma}{d\Omega}=\frac{4\pi}{k^2}\left|\sum_{L=0}^{\infty}Y_{L0}(\theta)e^{i\delta_L}\sin\delta_L\sqrt{2L+1}\right|^2 \quad (1.29)$$

1.2. Optical potential

The basic idea of the optical model is that a nucleon incident on a nucleus may be elastically scattered or it may create a variety of reactions[2]. In this framework the interaction between two nuclei is represented by a complex potential. The real part is referred to the refraction while the imaginary part accounts for the loss of flux going to any other open channel. At low energies the attenuation of the incident wave is predominant near the nuclear surface, due to the fact that the imaginary part of the potential may be large near the surface. As the incident energy increases, this phenomenon may become less important while, the absorption of the incident wave may take place throughout the whole nuclear volume[69]. In general, the potential is given by the form[70]:

$$V=V_0+iW_0 \quad (1.30)$$

where V_0, W_0 are the real and the imaginary part of the potential, respectively.

In this framework, both macroscopic and microscopic potentials can be used. In the microscopic approach the potential is obtained by assuming a nucleon-nucleon effective interaction, while in the macroscopic approach we take into account the nucleus as a whole system. The problem of this approach is that many different sets of parameters can be found to give good fits to the experimental data. This raises the question which physical content is correct.

It is known from previous heavy ion scattering experiments[4,7,51,57,58], relevant to the present investigation for the system ^{20}Ne+^{28}Si with cluster structure, that the cross section presents an oscillating behavior at backward angles. Into this context, several potentials like the Lee – Chan potential[51,57-58], the Ginocchio potential[9] and the Kobos – Satchler potential[7] were introduced to describe this behavior.

In this dissertation, two macroscopic potentials were used, one with a deep and one with a shallow depth of the real part. These potentials were based on a Woods – Saxon form factor[2] taking into account as initial values the parameters

obtained by the Lee – Chan[51,57-58] and the Christensen[71] potential, respectively. A microscopic potential based on the BDM3Y1 interaction[72] was also considered, while the ambiguities of the potentials were searched via a crossing point approach to be described in a following chapter. Finally, the optical model calculations were performed using the code ECIS[67], of which details are presented at the Appendix C.

1.3. The Woods – Saxon potential

The Woods – Saxon potential is a phenomenological potential proportional to the density of nucleons:

$$\rho(r) = \frac{\rho_0}{1+e^{(r-R)/a}} \tag{1.31}$$

and it is given by the following formula:

$$V(r) = \frac{V_0}{1+e^{(r-R)/a}} \tag{1.32}$$

where V_0 (MeV) represents the potential depth, $R=r_0A^{1/3}$ (fm) the nuclear radius and α (fm) the diffusivity. Also, A is the mass number and r_0~1.25 fm[2].

The Woods – Saxon potential is an attractive potential (increase with distance) and it is approximately flat in the center, for large A. Usually, in optical model framework, this potential is used to describe both a real and an imaginary part, according to the following formula:

$$V_{opt}(r) = \frac{V_0}{1+e^{(r-R_V)/a_V}} + i\frac{W_0}{1+e^{(r-R_W)/a_W}} \tag{1.33}$$

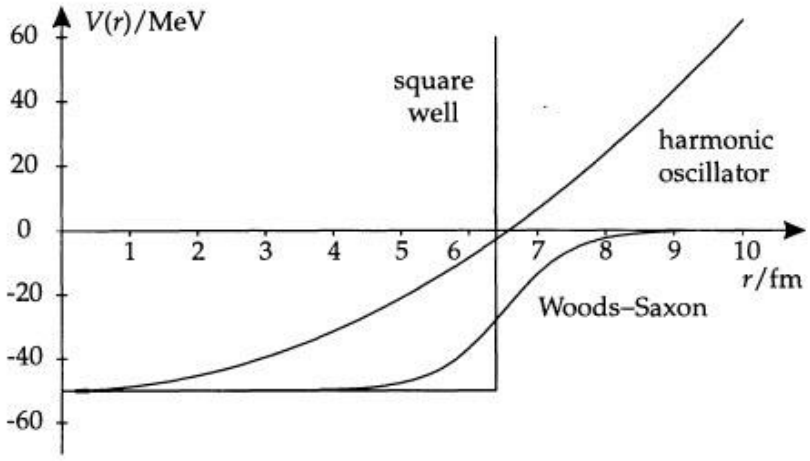

Figure 1.1: *A comparison between the Woods – Saxon potential, the harmonic oscillator and the square well.*

1.4. The Lee – Chan potential

The Lee – Chan (LC) potential was introduced by Lee and Chan in 1977 [51]. This optical potential was applied describing the elastic scattering data for the system $^{16}O+^{28}Si$ with satisfactory results, principally at lab energy of about 55 MeV (E_{cm}=35MeV)[58]. The LC potential is given by the formula bellow:

$$V(r) = -(V_0 + iW_0)\left[1 + \beta e^{\frac{r-R}{\alpha}} + e^{\frac{r-R}{b}}\right]^{-1} \qquad (1.34a)$$

where

$$R = r_0\left(A_1^{1/3} + A_2^{1/3}\right) \qquad (1.34b)$$

while, A_1 and A_2 are the mass numbers of the projectile and the target, respectively. For the system $^{16}O+^{28}Si$ the parameters are presented at the following table[57]:

V_0	W_0	β	α	b	r_0
286.5 MeV	19.7 MeV	0.99	3.7 fm	0.49 fm	1.122 fm

Also, the Coulomb radius was set r_C=1.2 fm.

It should be noted that, this potential is very interesting in the present study because it refers to a system similar to $^{20}Ne+^{28}Si$, that is to $^{16}O+^{28}Si$, and also at energies similar to the present study. It should be also noted that for β=0, the formula (1.34) drops to the usual Woods – Saxon formula[51,57-58].

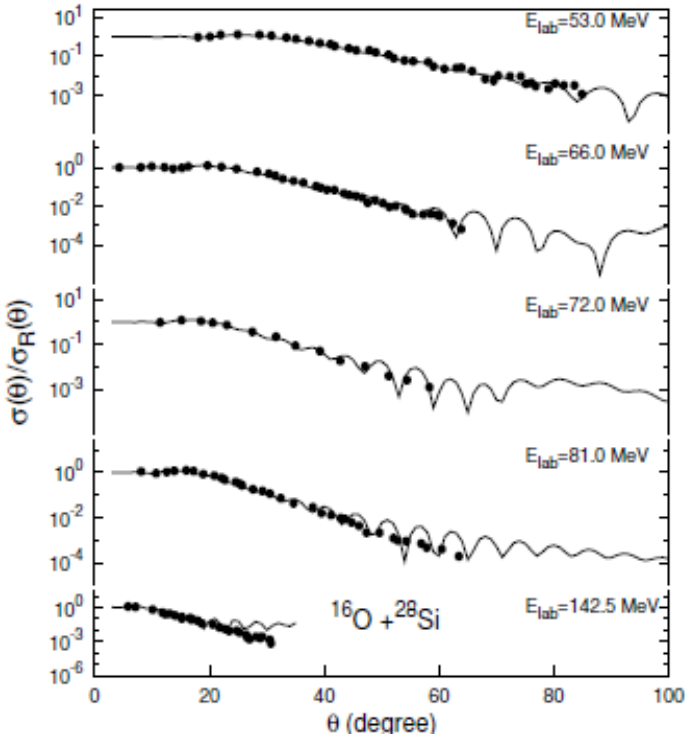

Figure 1.2: *Elastic scattering data of $^{16}O+^{28}Si$ at five different energies. Solid lines represent calculated results using the Lee – Chan potential (figure from S. K. Agarwalla et al,* ***J. Phys. G Nucl. Part. Phys. 32****, 165 (2006)).*

1.5. The Christensen potential

P.R. Christensen and A.Winther proposed an empirical potential in 1976. Using the formula bellow, they calculated the nuclear potential at the sensitive radius (further details about the sensitive radius in chapter 1.8) for various heavy ion collisions. After that, they performed a comparison between their potential and several potentials used in experimental data describing these collisions. It was found that for light projectiles ($5 \le Z_P \le 10$) and various targets ($5 \le Z_T \le 82$), the variation between the Christensen potential and the experimental potentials was very small[71]. The Christensen potential is given by the following formula, where R_P and R_T are the radius of projectile and the target respectively[71]:

$$U_N(r) = 50 \frac{R_P R_T}{R_P + R_T} e^{-\frac{r - R_P - R_T}{a}} \qquad (1.35a)$$

with

$$R_i = 1.233 A_i^{1/3} - 0.978 A_i^{-1/3} \ , \ i = P, T \qquad (1.35b)$$

and α=0.63 fm.

1.6. Microscopic potentials

A microscopic potential of interest is obtained in a double folding model, by using an effective nucleon-nucleon (NN) interaction folded over matter densities of the interacting nuclei[73]. For complex nuclei the total double folding potential is given by the formula:

$$U(r_P) = \iint \rho_P(r_1) \rho_T(r_2) u(r_{12}) dr_1 dr_2 \qquad (1.36)$$

where $r_{12}=r_p-r_1+r_2$, ρ_P is the density distribution of the projectile, ρ_T is the density distribution of the target and $u(r_{12})$ is the effective interaction and it has the form:

$$u(r_{12}) = u_{00} + u_{01} \tau_1 \cdot \tau_2 + u_{10} \sigma_1 \cdot \sigma_2 + u_{11} \sigma_1 \cdot \sigma_2 \tau_1 \cdot \tau_2 \qquad (1.37)$$

with **σ** and **τ** the Pauli and Isospin matrixes, respectively.

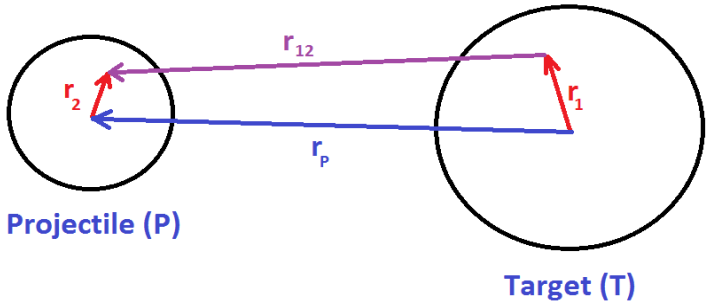

Figure 1.3: *Coordinates of the surface intergral (1.36).*

The most famous effective interaction is the M3Y interaction, where the two first terms of equation (1.37) are given as (in MeV)[73]:

$$u_{00}(r) = 7999\frac{e^{-4r}}{4r} - 2134\frac{e^{-2.5r}}{2.5r} \quad (1.38)$$

$$u_{01}(r) = -4886\frac{e^{-4r}}{4r} + 1176\frac{e^{-2.5r}}{2.5r} \quad (1.39)$$

It is known, that the wave function of N identical fermions has to be antisymmetric. So, the wave functions of the projectile and the target have to be antisymmetric. However, the term that describes the effective interaction between two nearby nucleons in the same nucleus is not antisymmetric. Taking this fact into account, an additional correction term should be added and then the effective interaction u_{00} is given by one of the following formulas[53,73]:

$$u_{00}(r) = 7999\frac{e^{-4r}}{4r} - 2134\frac{e^{-2.5r}}{2.5r} - 276\left(1 - 0.005\frac{\mathrm{E}}{\mathrm{A}}\right)\delta(r) \quad (1.40)$$

$$u_{00}(r) = 7999\frac{e^{-4r}}{4r} - 2134\frac{e^{-2.5r}}{2.5r} - 262\delta(r) \quad (1.41)$$

This model, with M3Y interaction, can reproduce the scattering of many different systems in the bombarding energy range of 5 to 20 MeV per nucleon[3]. Also, the real part of the potential in order to fit the data should be renormalized by a factor of 1.11±0.13 (with two exceptions: ^{6}Li and ^{9}Be)[3]. Apart from that, only the real part of the optical model potential can be described from the M3Y interaction and the imaginary part should be treated phenomenologically.

M3Y interaction has no energy or density dependence. A DDM3Y (Density Dependent M3Y) interaction takes into account the nuclear density. In particular, it is used a density range, approximately the 1/3 of the density of a normal nuclear matter. This density is introduced via the function:

$$f(\rho, E) = C(E)\left[1 + a(E)e^{-\beta(E)\rho}\right] \quad (1.42)$$

where ρ is the density of nuclear matter in which the interacting nucleons are embodied and C(E), α(E), β(E) are energy dependent parameters. Then, the first term of the interaction is given by the formula:

$$u_{00}^{DD}(r, \rho, E) = f(\rho, E)u_{00}(r) \quad (1.43)$$

where u_{00} is the original M3Y interaction.

Also, W.D. Myers[74], Dao T. Koa and W. von Oertzen[72] introduce a more realistic function for the density:

$$f(\rho) = C\left[1 - a\rho^{\beta}\right] \quad (1.44)$$

where C, α, β are parameters. This interaction was called BDM3Y and the relation (1.36) was changed accordingly. Some typical parameters for different types of the BDM3Y interaction are given at the following table[72].

Table 1.1: *Applied parameters for the four different types of the BDM3Y interaction.*

Interaction	C	α	β
BDM3Y0	1.3827	1.1135 fm^2	**2/3**
BDM3Y1	1.2253	1.5124 fm^3	**1.0**
BDM3Y2	1.0678	5.1069 fm^6	**2.0**
BDM3Y3	1.0153	21.073 fm^9	**3.0**

1.7. The Kobos – Satchler potential

The Kobos – Satchler potential was introduced by A.M.Kobos and G.R.Satchler in 1984 describing the elastic scattering data for the system $^{16}O+^{28}Si$ [7]. This system is similar to the $^{20}Ne+^{28}Si$ system, the system under investigation in the present work so, the behavior of this potential is very interesting for us.

For the real part of the potential, a microscopic term was used, described by an M3Y effective nucleon-nucleon interaction[73,75]. The renormalization factor was set equal to 0.96. The systematic behavior of the experimental data at different energies indicated that some additional terms should be taken into account. Into this context, the optical model analysis yields better fits to the data when two surface terms were added to the M3Y volume term. Both terms were described by the first derivative of a Woods-Saxon potential. As a result, two small "pockets" were created (figure 1.4) to the overall nuclear potential with an important impact to the interference between the barrier and the internal waves[56]. Therefore, the energy-independent real surface potential is given by the following expression:

$$\Delta U(r) = \sum_{i=1}^{2} U_i(r) \qquad (1.45a)$$

where:

$$U_i(r) = 4V_i a_i \frac{df(r, R_i, a_i)}{dr} \qquad (1.45b)$$

$$f(r, R_i, a_i) = \frac{1}{1 + e^{(r-R_i)/a_i}} \qquad (1.45c)$$

taking into consideration the convention that $R_2<R_1$. The radial range was found to be satisfactory between 5 and 10 fm after preliminary tests.

On the other hand, the imaginary part was chosen to have the following form:

$$W(r) = -W_V f(r, R_V, a_V) + 4W_D a_D \frac{df(r, R_D, a_D)}{dr} \qquad (1.46)$$

with the factor f given by eq. (1.45c). In addition, Kobos and Satchler impose a limitation on imaginary radii R_V, R_D according to the formula:

$$R_j = R_{0j}\left[1 + a(E - E_0)\right], \quad j = V, D \qquad (1.47)$$

where E is the center of mass bombarding energy (in MeV) and E_0=26.2MeV is an arbitrary parameter. Finally, a Coulomb potential with radius 7.79 fm was added.

The problem of this potential is the big number of parameters. It is obvious that the potential contains 13 parameters, V_1, R_1, α_1, V_2, R_2, α_2 for the surface real terms, W_V, R_{0V}, α_V, W_D, R_{0D}, α_D for the imaginary part and the α factor that determines the energy dependence of the R_V and R_D. The parameters are shown at table 1.2. Comparisons between the experimental data and the fits are shown in Figure 1.5, where the agreement is satisfactory.

Table 1.2: *Optical potential parameters for $^{16}O+^{28}Si$ scattering. Set I refers to center of mass energies from 18.67 to 26.2 MeV while, set II refers to energies from 31.6 to 34.8MeV (table from A. M. Kobos and G. R. Satchler,* ***Nucl. Phys. A 427****, 589 (1982)).*

	V_1 (MeV)	R_1 (fm)	a_1 (fm)	V_2 (MeV)	R_2 (fm)	a_2 (fm)	W_V (MeV)	R_{0V} (fm)	a_V (fm)	W_D (MeV)	R_{0D} (fm)	a_D (fm)	α (MeV^{-1})	E_0 (MeV)
set I	10.14	6.068	0.167	3.17	7.412	0.371	59.9	1.040	0.127	46.2	4.113	0.286	0.0585	26.2
set II	17.69	6.198	0.200	9.57	7.148	0.359	9.26	1.447	0.542	28.8	3.195	0.583	0.0502	26.2

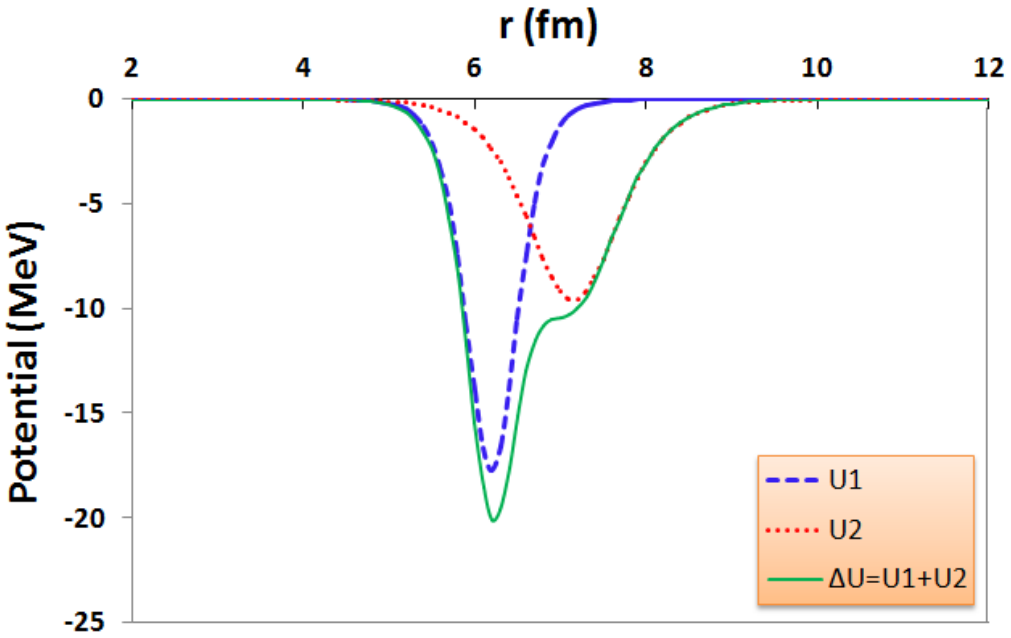

Figure 1.4*: The surface terms of the real part of the Kobos – Satchler potential U1, U2 and ΔU as a function of the radius.*

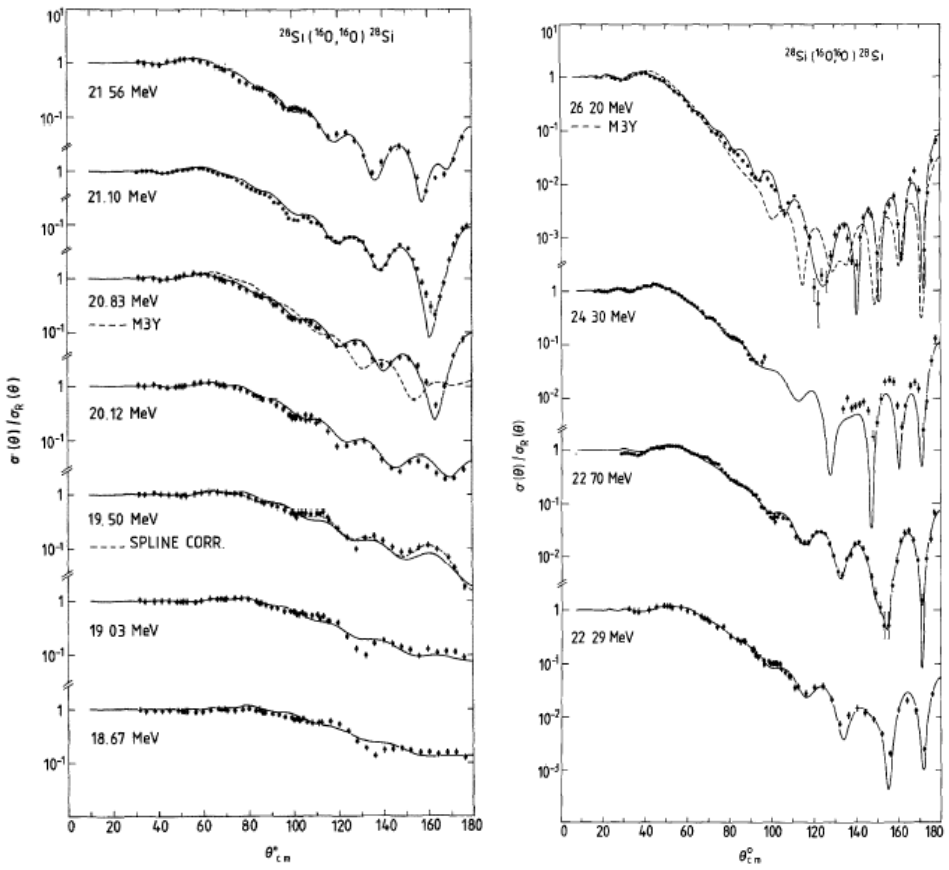

Figure 1.5: *Comparison of cross sections calculated using the optical parameters from set I (solid curves) with the experimental data. Predictions using the microscopic M3Y potential, without the surface factor ΔU, represented with the dashed lines at 20.83 and 26.2MeV (figure from A. M. Kobos and G. R. Satchler,* ***Nucl. Phys. A 427****, 589 (1982)).*

1.8. Ambiguity and sensitivity tests

Both discrete and continuous ambiguities may exist in an optical model determination. The first one refers to different families of potential depths that may give equivalent fits to the experimental data. The second one refers to a continuous ambiguity which arises when a small variation of one parameter can be compensated by adjusting one or more parameters of the optical potential to give equivalent fits to the data[76]. However, there is a radial range, near the nuclear surface, where the potential determination is accomplished accurately. As to determine this range, two different sensitivity tests were introduced: the "Crossing point method"[23,76-78] and the "Notch Perturbation method"[79].

In particular, assuming a typical case with a Woods – Saxon optical potential:

$$V_{opt} = \frac{V_0}{1+e^{(r-R_V)/a_V}} + i\frac{W_0}{1+e^{(r-R_W)/a_W}} = V_{WS} + iW_{WS} \quad (1.48)$$

and working separately for the real and the imaginary part, it is easy to determine the sensitive radial range using the "Crossing point method"[23,77]. As it was mentioned, many different potentials provide equivalent fits to the experimental data. Plotting these potentials as a function of radius, they cross each other at a specific radial point. In the vicinity of this crossing point, the nuclear potential can be determined in a unique way. As an example, the V_{WS} quantity as a function of radius r, for the system $^{20}Ne+^{28}Si$, is presented in figure 1.6 where, the sensitive radius or the crossing point is about 8.04 fm. Further details of this procedure are presented in chapter 4.

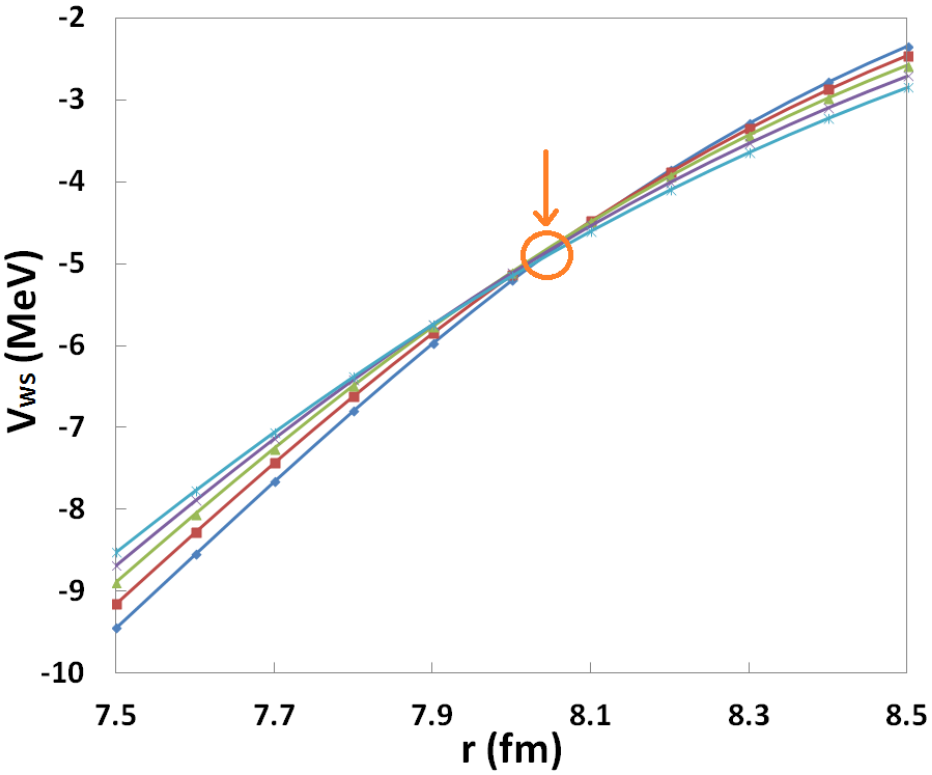

Figure 1.6: *The real part of an optical potential, for the system $^{20}Ne+^{28}Si$, as a function of radius for five different values of diffusivities α: 0.50, 0.55, 0.60, 0.65 and 0.70 with the blue, red, green, violet and turquoise blue line, respectively. The circled area presents the crossing point appeared at r=8.04 fm.*

On the other hand, the "Notch Perturbation method"[79] is based on the introduction of a localized perturbation (notch) into the radial real or imaginary optical potential and the observation of the effect of such a perturbation on the predicted cross section as the perturbation is moved systematically through the potential. This approach can be accomplished, decreasing the potential in a small region and then increasing it in the normal value (figure 1.7). There are two different

techniques for obtaining this. The first one is based on a Woods – Saxon form factor perturbation:

$$g(R',a',d,r)=1-\{f(R',a',r)d[1-f(R',a',r)]\} \qquad (1.49)$$

where *f* (R',α',r) is the Woods – Saxon form factor given by the formula (1.45c). Then, assuming a Woods – Saxon potential, the potential could be written as:

$$V(r)=V_0 f(R,a,r)g(R',a',d,r) \qquad (1.50)$$

where R, α are the known Woods – Saxon parameters and R', α' determines the position and the width of the notch, respectively. The d parameter is the fraction by which the potential is reduced.

On the other hand, according to the second technique, the nuclear potential is reduced by a factor of (1-d). Both techniques give similar results.

In summary, this sensitivity test is based on the fact that, at positions where the calculation strongly depends on the details of the potential, the calculation will be changed by the perturbation while, at radial positions where the calculation has no sensitivity to the parameters of the potential, the perturbation will have no effect to the calculation.

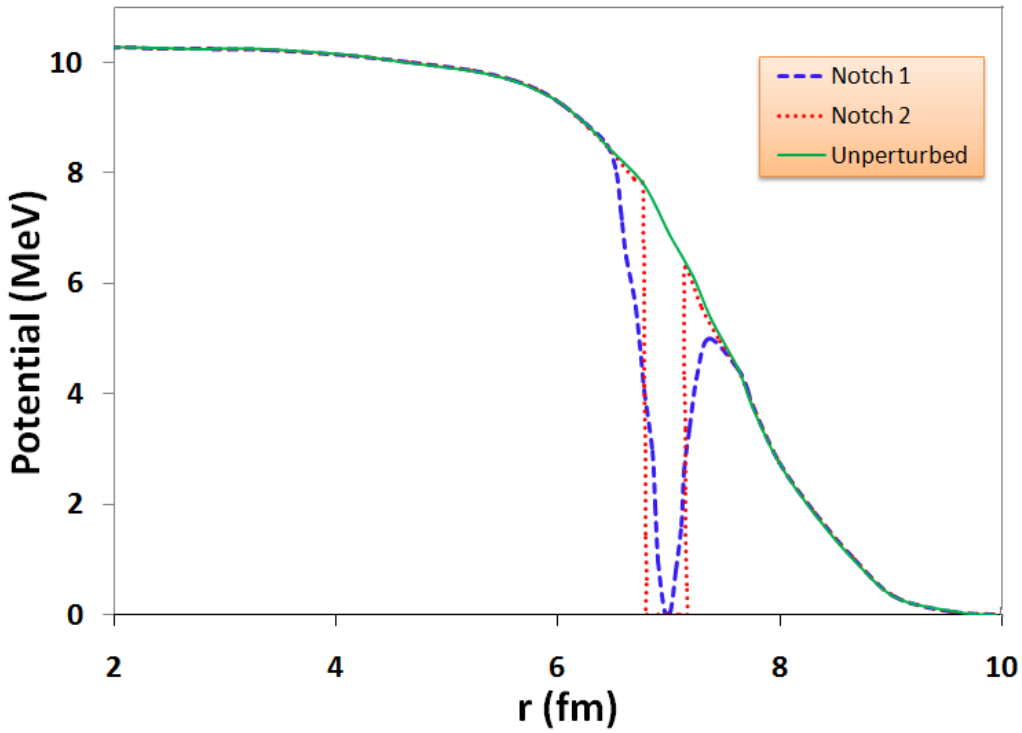

Figure 1.7: *Comparison of unperturbed potential with the two techniques of the "notch perturbation method" described above. The Woods – Saxon notch, the step function notch and the unperturbed potential presented with the blue dashed, the red dotted and the green solid line respectively (potential from John G. Cramer and Ralph M. DeVries,* ***Phys. Rev. C 22****, 91 (1980)).*

2. Experimental setup

2.1. The ICARE chamber

The experimental setup was visualized in the ICARE facility of the Heavy Ion Laboratory (H.I.L.) in Warsaw, using a ^{20}Ne beam delivered by the U-200P cyclotron and a ^{28}Si target. The setup is described in details below. ICARE is a charged particle detection system, initially builted in the IReS (Strasbourg). It consists of 1m diameter reaction chamber with various facilities for setting up numerous silicon detectors and telescopes (up to 48)[60]. In this respect, the chamber includes two platforms (A and B) and several rings that allow us to place many detectors. ICARE is supported by the vacuum and gas systems, electronics and data acquisition systems.

Inside the ICARE chamber, a motherboard is attached, which includes the preamplifiers (Figure 2.1). After that, the analog and logical signals are fed to the appropriate electronics and in particular the amplifiers, the discriminators and the ADC's, to be modified properly and finally to be handled by the "Midas" acquisition system. "Midas" system provides also a facility for monitoring the performance for the electronics and power supplies.

Some details of the ICARE facility are presented in Figures 2.1 – 2.3.

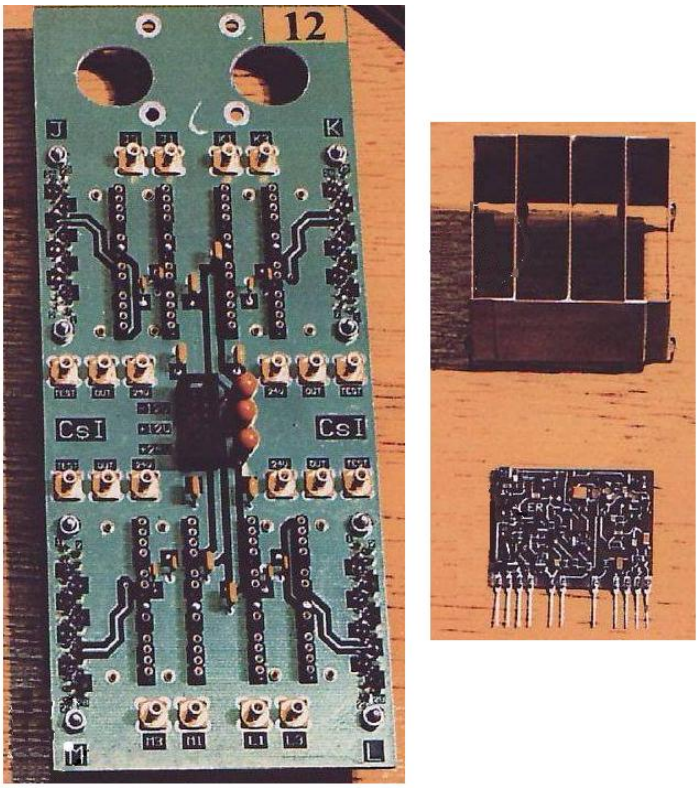

Figure 2.1: *The main electronics devices attached to ICARE chamber: motherboard [left] and preamplifier with its cover [right] (photo from I. Strojek: private communication).*

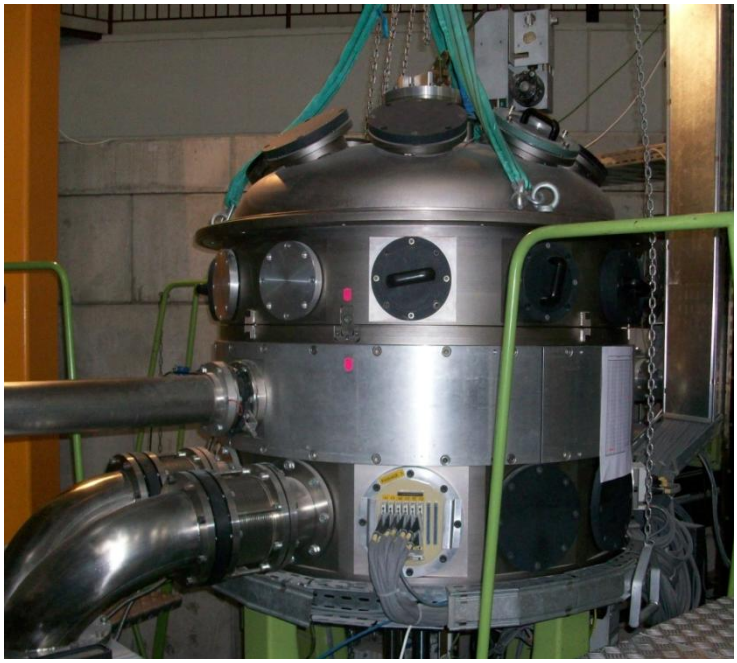

Figure 2.2: *The ICARE chamber.*

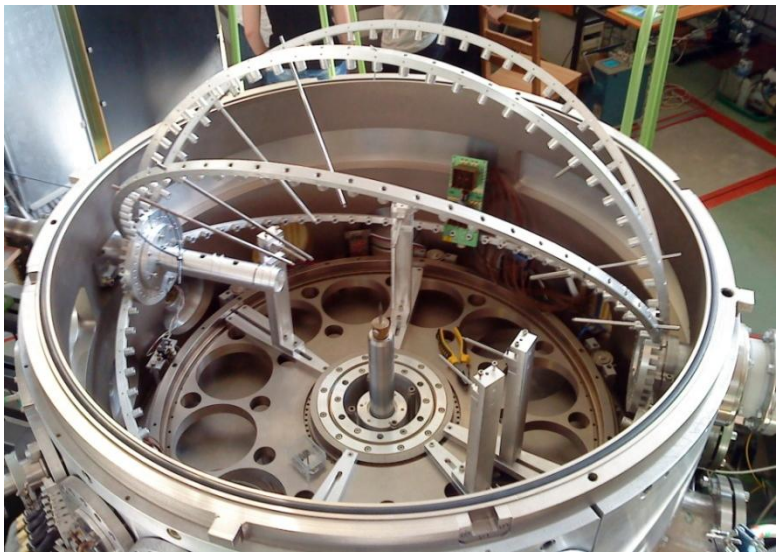

Figure 2.3: *The ICARE chamber.*

A general description for silicon (Si) and gas detectors is given below.

2.2. Silicon detectors

A Si surface barrier detector (semiconductor detector) is based on a p-n junction. The p – n junction is the border between a “p” and an “n” type zone. Both sides are electrically neutral, but they have different concentration of electrons (n-type) or holes (p-type). The free electrons from the n-type material begin to diffuse across the p – n junction between the two materials and fill some of the holes in the

p-type material. This procedure stops when the system equilibrates and that leads to the formation of a – charge free – depletion region between the p and n type zone.

When an incident radiation passes through the depletion region, pairs of holes and electrons are created. Under the influence of an electric field, electrons and holes move towards the electrodes creating a pulse proportional to the total number of electrons – holes pairs. So, this pulse is proportional to the energy of the incident particle. Also, by raising the bias, the depletion zone is broadened leading to an increase in the flux of the electrons and holes pairs. This procedure increases the collection rate.

In particular, in this experiment, we used surface barrier silicon detectors. These ones are the most usual Si detectors and they are very useful for measuring the energy loss of passing charged particles. These detectors have a much higher resolution in tracking charged particles than older technologies such as cloud chambers but, the disadvantages are that surface barrier Si detectors are much more expensive than older detectors and they are sensitive to light and to surface contaminations [81-83].

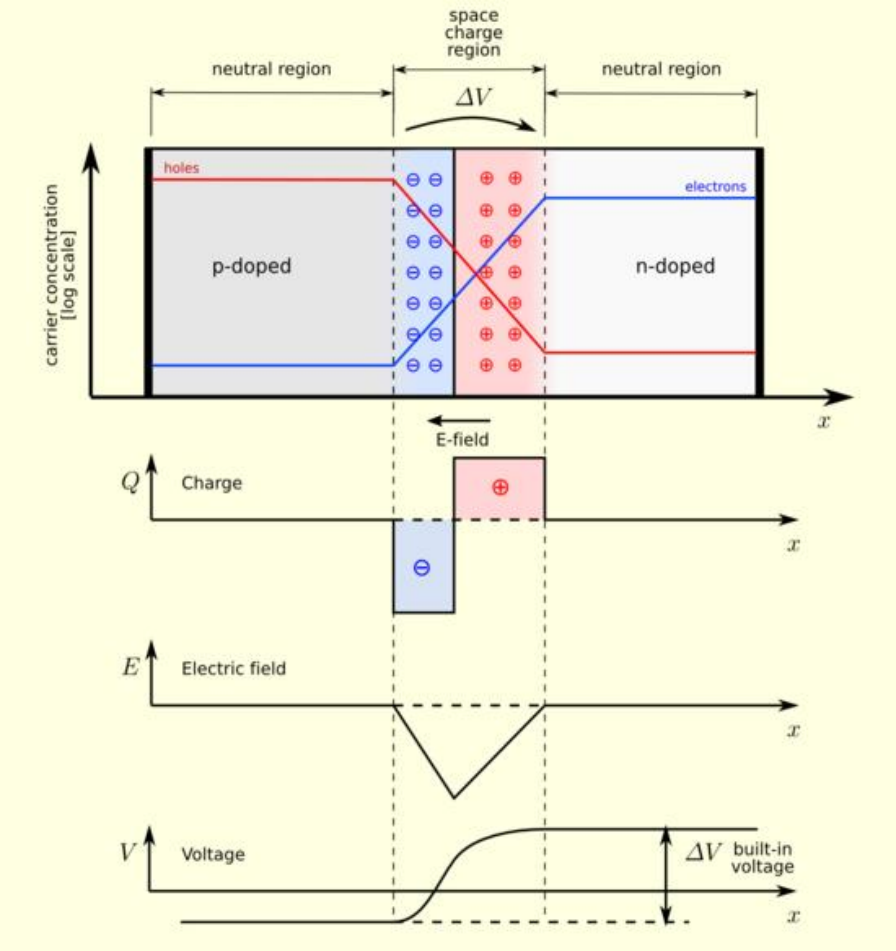

Figure 2.4: *A p–n junction in thermal equilibrium with zero-bias voltage applied. Under the junction, plots for the charge density, the electric field and the voltage are reported. Electrons and holes concentration are reported with blue and red lines, respectively.*

2.3. Gas detectors

A typical gas detector is based on the ionization phenomenon and consists of a cylinder, filled with an applicable gas, and a conducting wire is placed along its axis to which a positive potential difference is applied. Therefore, a radial electrical field is produced and when a charged particle crosses the detector, a number of pairs of positive and negative charged ions are formed along its orbit. The negative ions (electrons) are forced to move to the anode while, the positive ones move to the cathode. Also, in this experiment, the gas detectors were used as ionization chambers. The basic construction of a gas detector is presented at figure 2.5 [81].

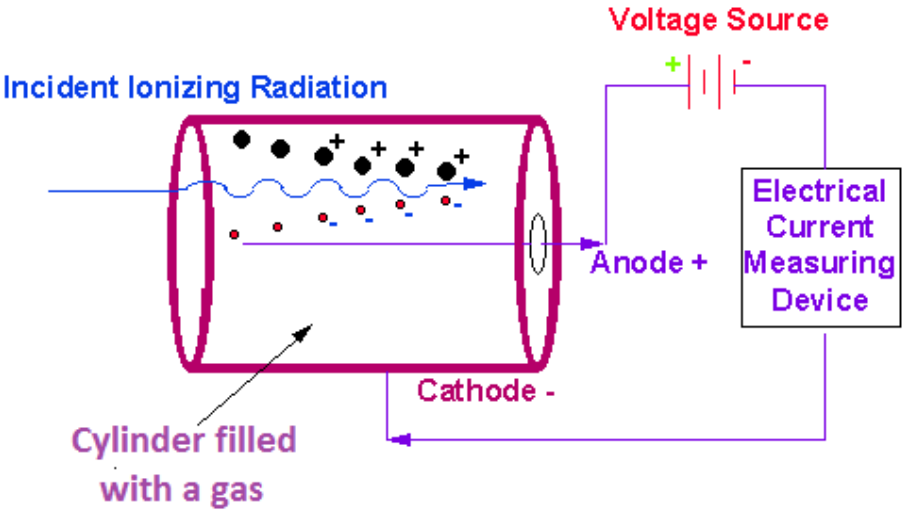

Figure 2.5: *Basic construction of a simple gas ionization detector.*

2.4. Detectors – Telescopes

In this experiment both single silicon detectors and telescopes were used. The thickness of the single detectors was 40μm. The structure of Si detectors is shown in Figure 2.6.

On the other hand, the telescopes were consisting of two parts. The first part was the gas detector (C_4H_{10}) with thickness 47mm and a gas pressure at 11.25Torr, while the second part was a Si detector with thickness 500μm. The telescope window is a Mylar foil with thickness 2.5μm. The structure of telescopes is shown in Figure 2.7 [80,84]. The first part of the telescope absorbs a part of the recoil ion, allowing a Z separation via ΔE-E technique.

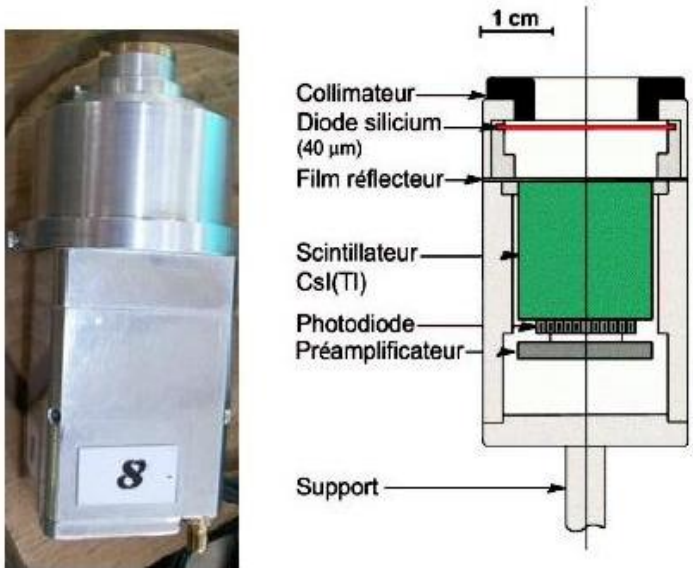

Figure 2.6: *The Si detector's structure.*

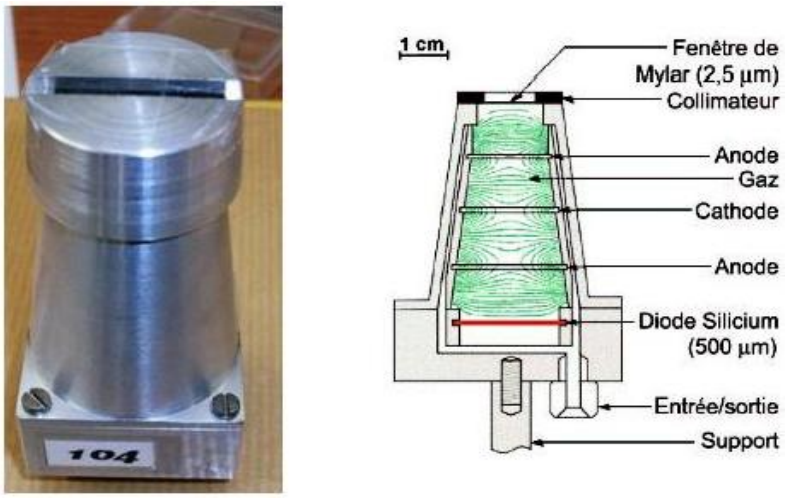

Figure 2.7: *The telescope's structure.*

2.5. Details of the setup

In this experiment, the ^{20}Ne+^{28}Si elastic scattering was studied at energies of **42.5, 52.3** and **70.0 MeV** using silicon targets with thicknesses of **~132 µg/cm^2** and **~200 µg/cm^2**.

2.5.1. Detector's position

Taking into consideration an expected angular distribution, the theoretical calculations performed by N. Keeley concerning the system of ^{20}Ne + ^{28}Si [62] and the elastic scattering experiments of ^{16}O + ^{28}Si [4,7,53,57], the position of the detectors and the telescopes was decided to be as in the lay out presented in Figures 2.8 and 2.9:

- **Platform A:** In this platform (Side A), a telescope (T1) was placed which is scanning the angular range between 25^o and 85^o in steps of 5 degrees. In the same platform, a single detector (S1) is set such as to rotate between 75^o and 135^o.
- **Platform B:** In platform B (Side B), two telescopes (T2 and T3) were scanned the angular range 37^o - 60^o and 57^o - 80^o, respectively.
- **Rings:** Eight single silicon detectors were placed at fixed positions at the rings. In forward angles two monitors (M1, M2) were set in symmetrical positions, at $\pm 20^o$, for correcting beam misalignments. Finally, in order to "capture" the elastic part of the reaction at backwards angles six detectors (S2, S3, S4, S5, S6,S7) were placed at $+55^o$, $+85^o$, $+125^o$, -45^o, -75^o, -100^o respectively.
- **Distances between detectors – target:** The distances between detectors/telescopes and target were adjusted as shown at table 2.1. The error concerning the distance measurements is ± 0.1cm.

It should be noted however that, in this experiment, the telescopes were the main tools to perform the angular distribution and also to separate the elastic channel from the other reaction products.

Table 2.1: *Detectors' distances from the target.*

Detector Name	*Detector ID*	*Distance from the target (cm)*
M1	**8**	**31.5**
M2	**26**	**31.5**
T1	**104**	**11.5**
T2	**106**	**11.5**
T3	**107**	**11.4**
S1	**19**	**11.1**
S2	**11**	**11.5**
S3	**23**	**11.5**
S4	**24**	**11.5**
S5	**13**	**11.6**
S6	**16**	**13.5**
S7	**9**	**11.6**

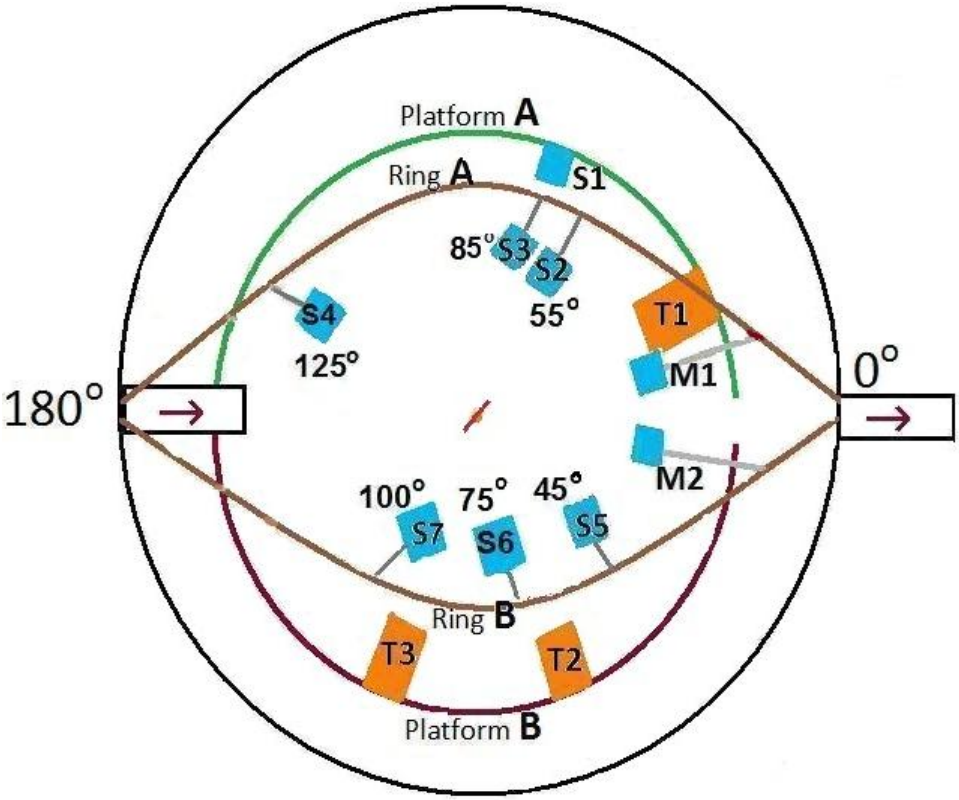

Figure 2.8: *Schematical details of the setup.*

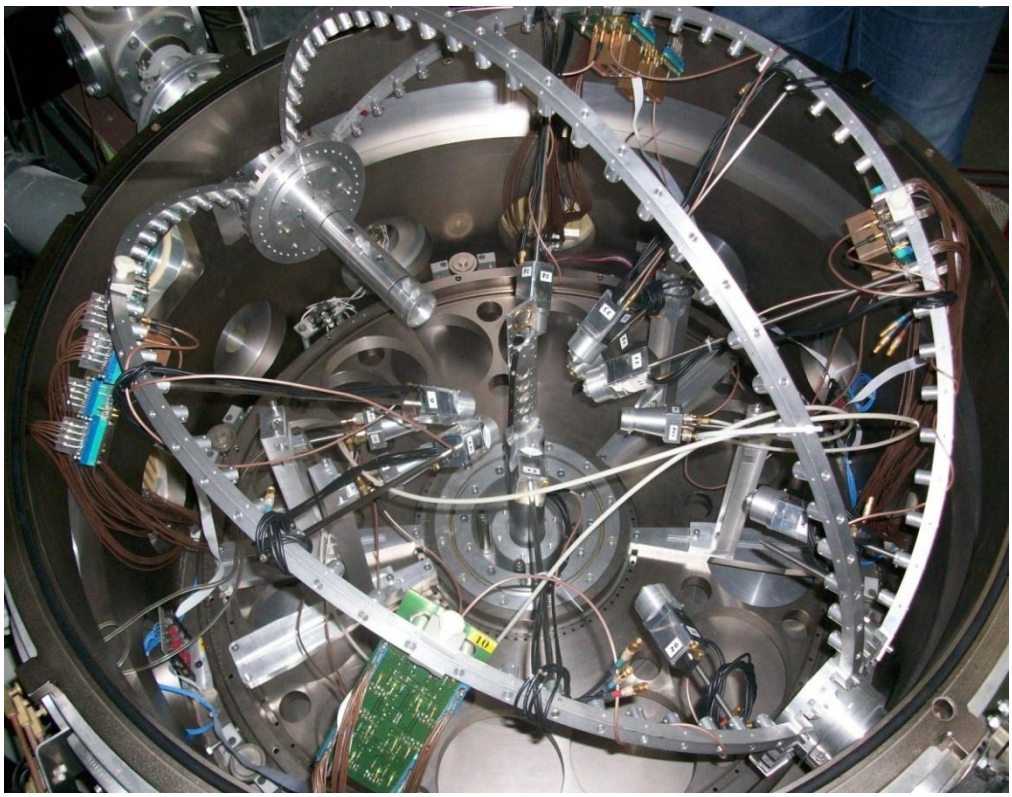

Figure 2.9: *Experimental design: Photo of ICARE chamber, with the present setup.*

2.5.2. «Masks»

Masks were placed in front of the detectors for defining in a more accurate way their solid angle. The dimensions of the masks for all the single silicon detectors were (4x7) mm^2, while for the monitors were (2x7) mm^2 and for the telescopes were (3.5x10.5) mm^2.

2.5.3. Target position

A target holder was set at the middle of the chamber. The target holder is shown in Figure 2.10 with all the details of the targets. A quartz was also placed for defining the beam position.

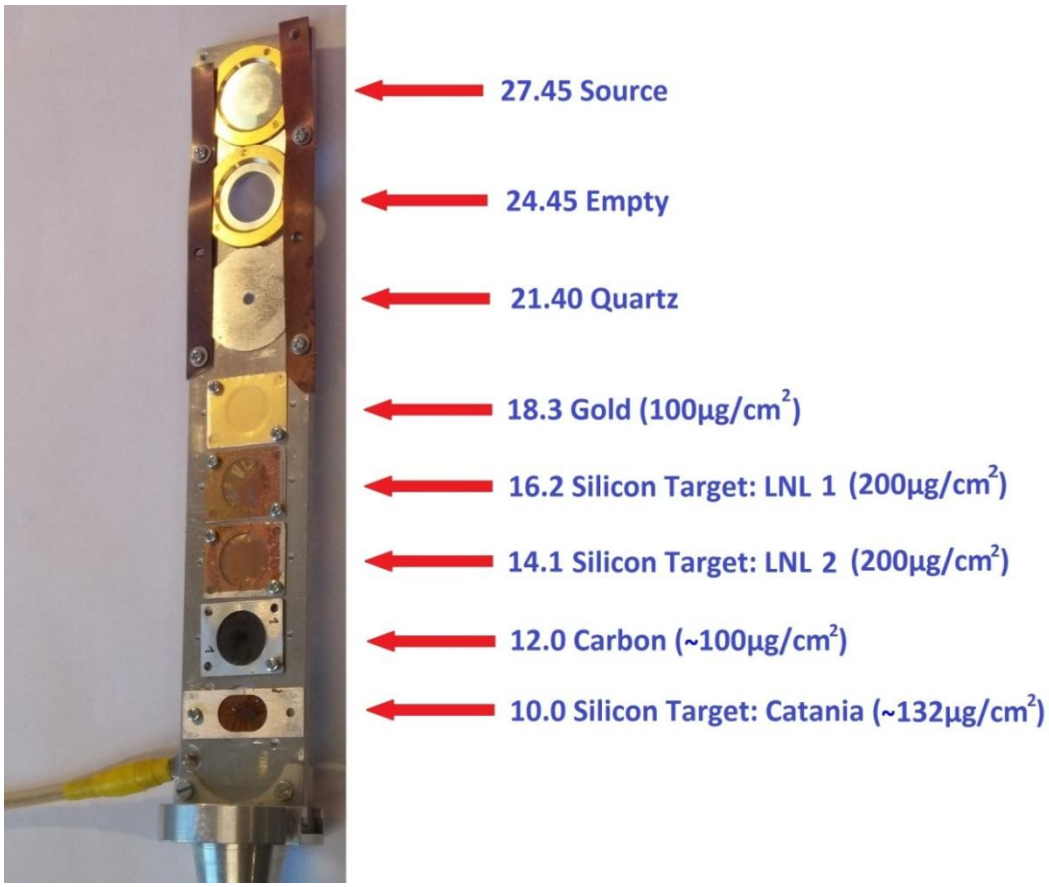

Figure 2.10: *The target holder.*

2.5.4. Platform's calibration

The rotation of platforms was calibrated in degrees before the experiment and the data are shown at tables T2.1a and T2.1b [80].

3. Data reduction

3.1. Energy calibration

The main step for an accurate data reduction is a good energy calibration. The energy calibration for each detector was based on measurements via an ^{241}Am source with an α-peak at 5.486 MeV and a pulser (Figure 3.1 and table T3.1).

In particular, the pulser was calibrated through the alpha source (table T3.2) and the detectors were calibrated via the pulser in a large energy range (table T3.3 and Figure 3.2) according to the formula:

$$Energy = A*(channel) + B \quad (3.1)$$

where *A, B* parameters given at table T3.3.

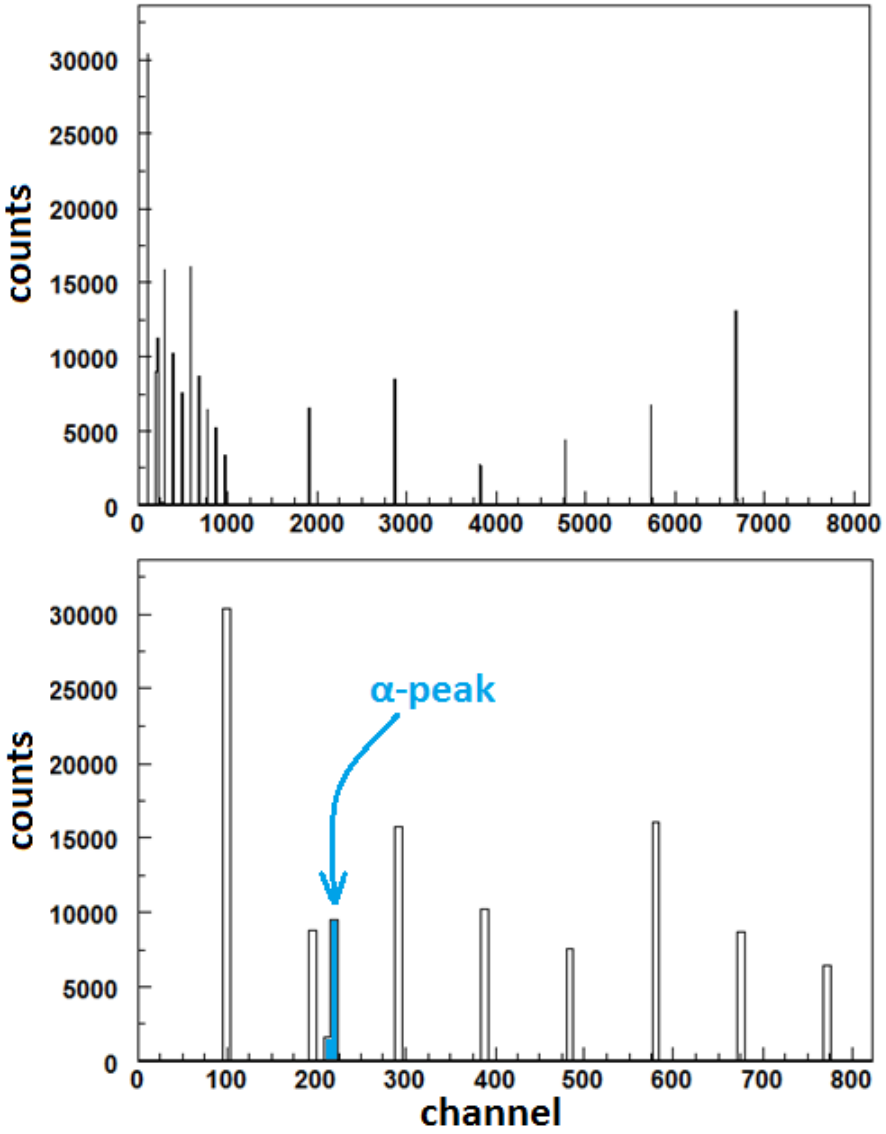

Figure 3.1: *Spectrum with pulser and alphas peaks used in energy calibration.*

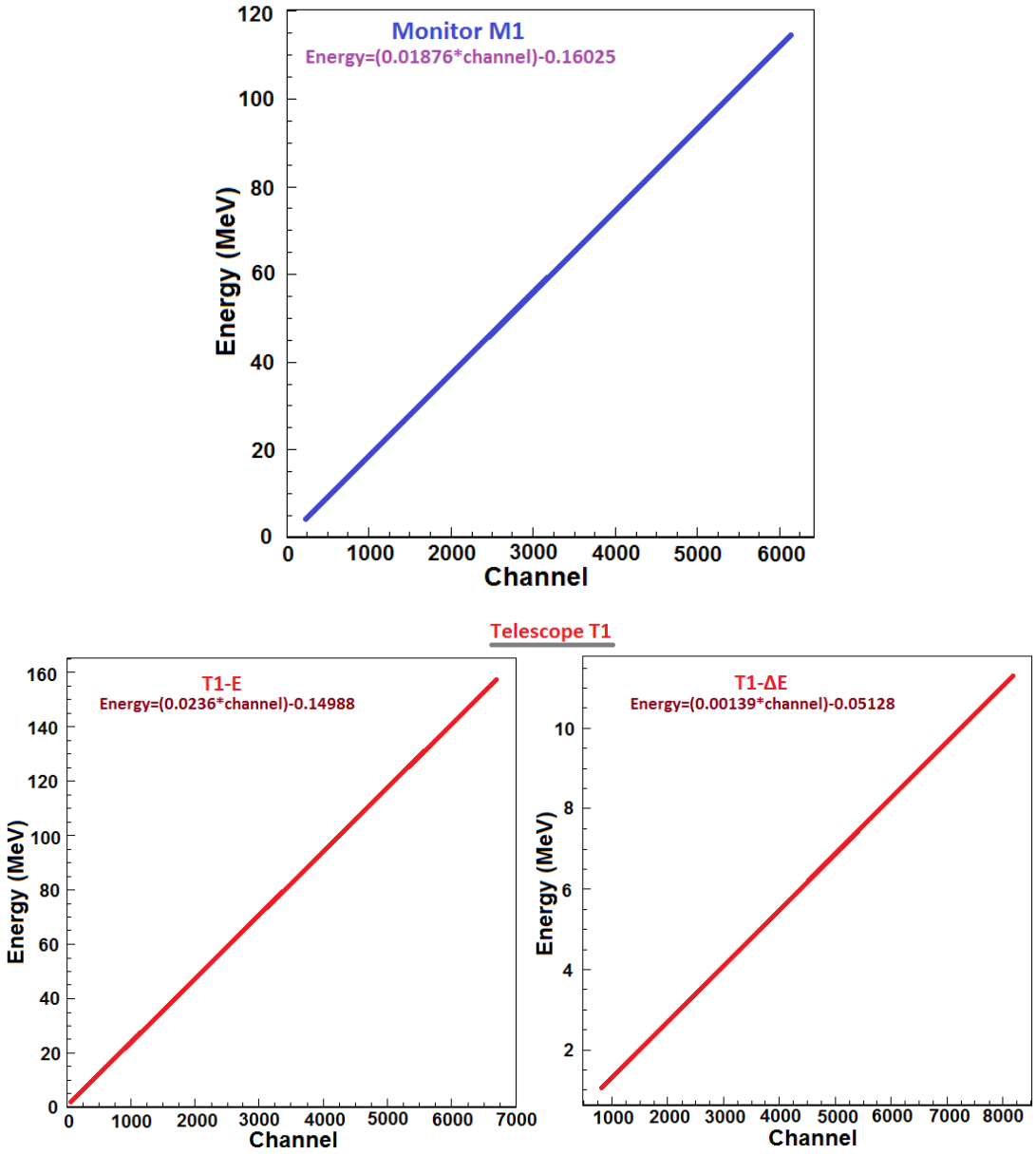

Figure 3.2: *Energy as a function of the channel for three representative detectors: M1, T1-Si and T1-gas.*

3.2. Identification of reaction channels

The data analysis was performed with the program PAW[85]. Taking into account the kinematics of the colliding ions and the energy losses, using the programs LISE++[86] and NRV[87], the identification of the reaction channels was performed as appears at the table 3.1. In particular, for the input channel ^{20}Ne+^{28}Si of interest, four output channels were observed: the elastic scattering **^{28}Si(^{20}Ne,^{20}Ne)^{28}Si**, the one – alpha transfer reactions **^{28}Si(^{20}Ne,^{16}O)^{32}S** (stripping reaction) and **^{28}Si(^{20}Ne,^{24}Mg)^{24}Mg** (pick-up reaction) and the ^{8}Be-transfer reaction

^{28}Si(^{20}Ne,^{12}C)^{36}Ar (stripping reaction). Some typical spectra are presented at figures 3.3-3.5.

Table 3.1: *The identification of the reaction channels observed at the experiment. The observed quantity is represented with the blue color at the output channel's column.*

Input channel	Output channel	Q value	42.5 MeV	52.3 MeV	70.0 MeV	Notation
^{20}Ne + ^{28}Si	**^{20}Ne** + ^{28}Si	0.00 MeV	X	X	X	Elastic scattering
^{20}Ne + ^{28}Si	**^{16}O** + ^{32}S	2.22 MeV		X	X	One alpha transfer, stripping
^{20}Ne + ^{28}Si	**^{24}Mg** + ^{24}Mg	-0.67 MeV		X	X	One alpha transfer, pick-up
^{20}Ne + ^{28}Si	**^{12}C** + ^{36}Ar	1.70 MeV		X	X	Two alpha transfer, stripping
^{20}Ne + ^{24}Mg	**^{24}Mg** + ^{20}Ne	0.00 MeV		X	X	Impurities, elastic scattering recoil
^{20}Ne + ^{24}Mg	**^{16}O** + ^{28}Si	5.25 MeV		X	X	Impurities, one alpha transfer
^{20}Ne + ^{16}O	**^{20}Ne** + ^{16}O	0.00 MeV			X	Target oxidation, elastic scattering
^{20}Ne + ^{16}O	**^{16}O** + ^{20}Ne	0.00 MeV		X	X	Target oxidation, elastic scattering recoil
^{20}Ne + ^{16}O	**^{12}C** + ^{24}Mg	2.15 MeV		X	X	Target oxidation, one alpha transfer
^{20}Ne + ^{16}O	**^{24}Mg** + ^{12}C	2.15 MeV			X	Target oxidation, one alpha transfer
^{20}Ne + ^{12}C	**^{12}C** + ^{20}Ne	0.00 MeV		X	X	Contamination, elastic scattering recoil
^{20}Ne + ^{120}Sn	**^{20}Ne** + ^{120}Sn	0.00 MeV	X	X	X	Impurities, elastic scattering
^{20}Ne + ^{197}Au	**^{20}Ne** + ^{197}Au	0.00 MeV	X	X	X	Impurities, elastic scattering
^{20}Ne + ^{208}Pb	**^{20}Ne** + ^{208}Pb	0.00 MeV	X	X	X	Impurities, elastic scattering

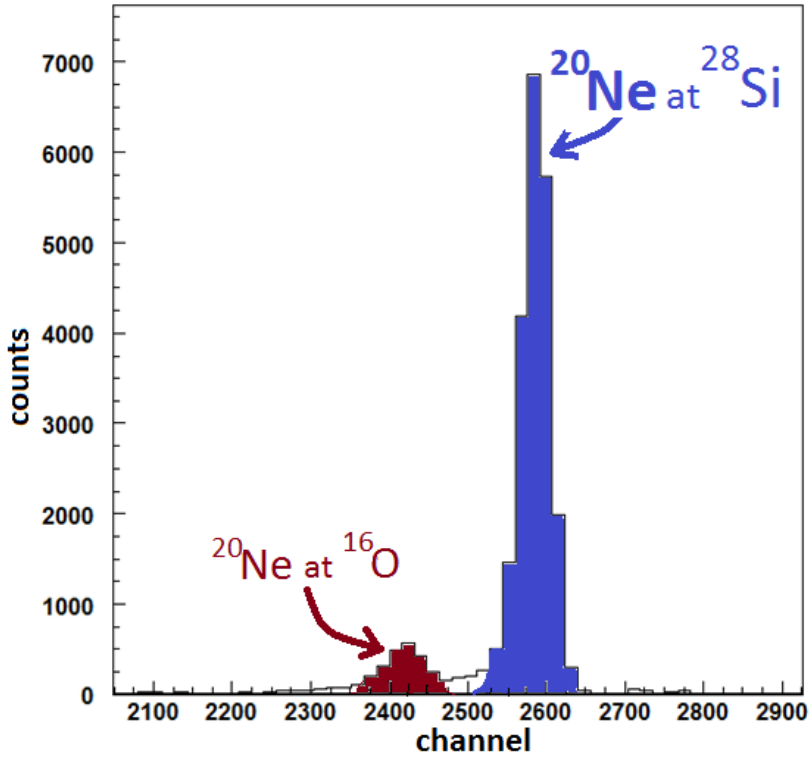

Figure 3.3: *A typical 1d spectrum from the monitor M1 (20deg) at energy of 52.3 MeV.*

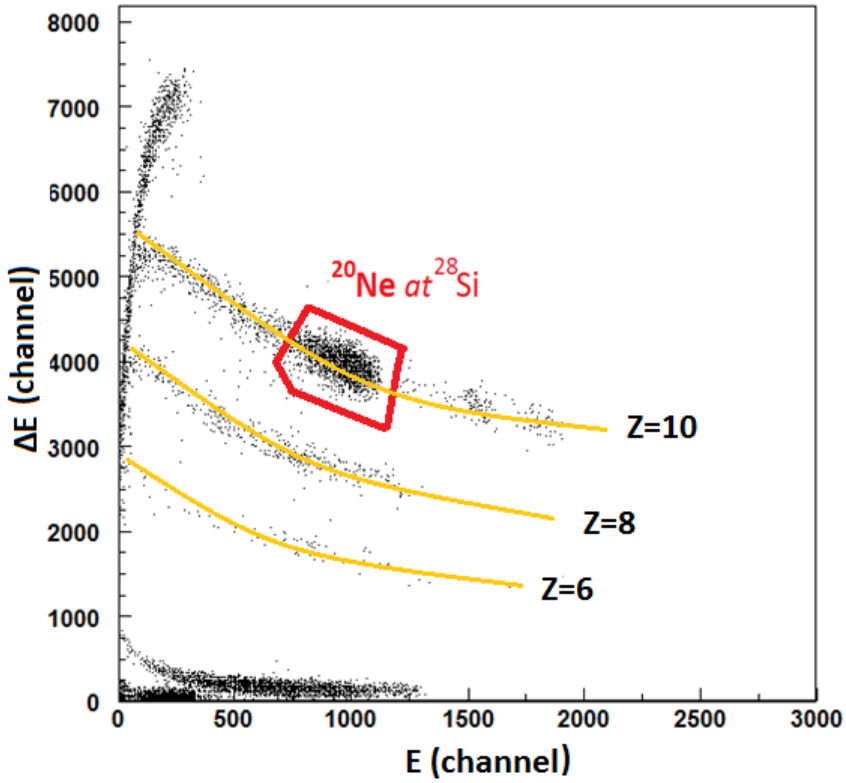

Figure 3.4: *A typical 2d spectrum from T1 telescope at 45deg and at energy of 52.3 MeV. The circled area presents ^{20}Ne from the elastic scattering ^{28}Si(^{20}Ne,^{20}Ne)^{28}Si. The solid lines are there to guide the eye.*

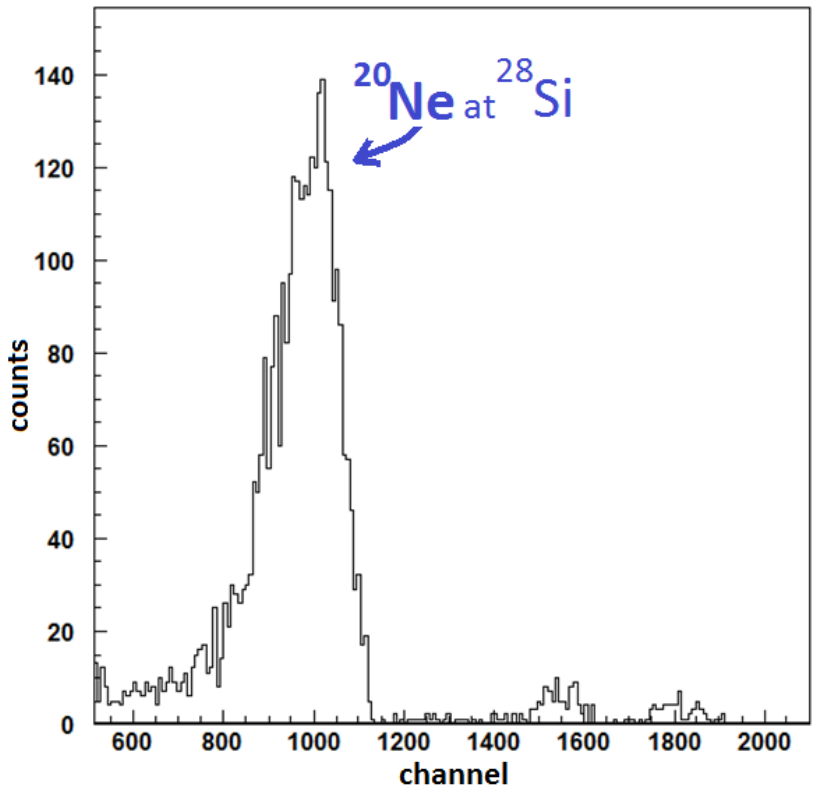

Figure 3.5: *The projection of figure 3.4 on E - axis (T1- E, 45deg, 52.3MeV). The smaller peaks at the right side of the spectrum present elastic scattering to heavier impurities.*

In contour with Z=10, except of the main peak (coming from the ^{20}Ne+^{28}Si elastic scattering), four other peaks were observed due to target oxidation (^{20}Ne+^{16}O) or impurities (^{20}Ne+^{120}Sn, ^{197}Au, ^{208}Pb).

3.3. Determination of cross section

The cross section gives us the probability for a reaction to take place. The differential cross section is given by the following formula:

$$\sigma(\theta) = \frac{N}{(D\Phi)\Omega} \qquad (3.2)$$

where:

σ(θ) is the cross section

N represents the number of counts,

Ω is the solid angle,

Φ is the flux of the beam and

D are the scattering centers.

The $(D\Phi)$ quantity is calculated via the monitors' information (±20°), by the known Rutherford scattering using the formula:

$$D\Phi = \left(\frac{N}{\sigma\Omega}\right)_{Ruth} = \frac{N_m}{\sigma_{Ruth}\Omega_m} \qquad (3.3)$$

where:

N_m is the number of counts of the monitor,

σ_{Ruth} is the Rutherford scattering cross section and

Ω_m is the solid angle of the monitor.

The σ_{Ruth} calculations were performed by the program LISE++[86], assuming that the reaction took place at the middle of the target. The DΦ quantity is determined with a low error because at 20° where the monitors were placed, the statistical errors were not significant. Also, the two monitors at symmetric positions minimize the error due to the asymmetry of the beam.

Using the formulas (3.2) and (3.3) the final expression for the differential cross section is given by the formula below:

$$\sigma(\theta) = \frac{N\sigma_{Ruth}\Omega_m}{\Omega N_m} \qquad (3.4)$$

The above formula does not depend on the flux of the beam or the thickness of the target.

The Ω quantity was determined by the known activity of ^{241}Am source given by the formula below:

$$\Omega_a = \frac{4\pi}{R}\frac{N_\alpha}{t} = \frac{4\pi}{(40000Bq)}\frac{N_\alpha}{t} \qquad (3.5)$$

where:

N_a is the number of counts of alpha source,

R is the activity of the source (40kBq) and

t is the time of the measurement.

The solid angle was also calculated by the program GATE[64-66]. GATE is a simulation toolkit based on Geant4 Monte Carlo simulation, details of which are presented in appendix B. We assumed a cylindrical isotropic alpha source (^{241}Am) with radioactivity 40kBq and the geometry presented at table 3.2. Simulated and actual values of the solid angle used in the experimental analysis are presented at table 3.3. Although the variation between the experimental and the simulated solid angle values is significant, at the cross section expression (3.4), the variations in the ratio Ω_m/Ω, which is introduced in our calculations is more acceptable. This variation between the experimental and the simulated Ω_m/Ω ratio is presented at table 3.4.

Table 3.2: *Geometry for the Monte Carlo simulation.*

Detector	*Distance from the source (cm)*	*Mask (mm^2)*	*Thickness of the detector*	*Radius of the source (mm)*	*Thickness of the source (mm)*
M1	31.5	2x7	40μm	1.5	0.1
M2	31.5	2x7	40μm	1.5	0.1
T1-gas	11.5	3.5x10.5	47 mm	1.5	0.1
T2-gas	11.5	3.5x10.5	47 mm	1.5	0.1
T3-gas	11.4	3.5x10.5	47 mm	1.5	0.1
T1-Si	17.1	3.5x10.5	500μm	1.5	0.1
T2-Si	17.1	3.5x10.5	500μm	1.5	0.1
T3-Si	17.0	3.5x10.5	500μm	1.5	0.1
S3	11.5	4x7	40μm	1.5	0.1
S4	11.5	4x7	40μm	1.5	0.1
S5	11.6	4x7	40μm	1.5	0.1
S6	13.5	4x7	40μm	1.5	0.1
S7	11.6	4x7	40μm	1.5	0.1

Table 3.3: *A comparison between the solid angle values calculated by the known activity of Americium source (Ω_α) and via GATE simulation (Ω_{GATE}) for the detectors used in the experimental analysis. Also, N_α is the number of counts of the alpha peak and t is the time of the measurement.*

Detector	t [sec]	N_α [Counts]	Ω_α [sr]	Ω_{GATE} [sr]	Variation
M1	1080	429	**1.247E-04**	1.774E-04	29.7%
M2	1080	395	**1.148E-04**	1.774E-04	35.2%
T1-E	1680	11260	**2.105E-03**	2.584E-03	18.5%
T2-E	1260	8888	**2.215E-03**	2.582E-03	14.2%
T3-E	840	4673	**1.747E-03**	2.621E-03	33.3%

Table 3.4: *A comparison between the ratio Ω_m/Ω, calculated by the known activity of Americium source [$(\Omega_m/\Omega)_\alpha$] and via GATE simulation [$(\Omega_m/\Omega)_{GATE}$] for the detectors used in the experimental analysis.*

Detector	$(\Omega_m/\Omega)_\alpha$	$(\Omega_m/\Omega)_{GATE}$	Variation
T1-E	5.927E-02	6.864E-02	-13.7%
T2-E	5.185E-02	6.868E-02	-24.5%
T3-E	6.574E-02	6.767E-02	-2.8%

The σ and σ/σ_{Ruth} quantities for the elastic scattering **^{28}Si(^{20}Ne,^{20}Ne)^{28}Si** were determined using the formulas (3.4) and (3.5) at the near barrier energies of 52.3, 42.5 and 70.0 MeV (tables T3.4 – T3.6). The uncertainties were calculated via the formula below and are included at tables T3.4 – T3.6.

$$\sigma_{\sigma/\sigma_{Ruth}} = \frac{\sigma}{\sigma_{Ruth}}\left[\frac{1}{N}+\frac{1}{\mathrm{N}_m}+\frac{t^2+\mathrm{N}_\alpha\sigma_t^2}{t^2\mathrm{N}_\alpha}+\frac{t_m{}^2+\mathrm{N}_{\alpha m}\sigma_{tm}^2}{t_m{}^2\mathrm{N}_{\alpha m}}\right]^{1/2} \qquad (3.6)$$

where:

N is the number of counts of ^{20}Ne from the elastic scattering,

N_α is the number of counts of alpha source,

t is the time of the measurement,

σ_t is the error at the time measurement (±30 sec)

The index *m* refers to the monitor. It should be noted that the last two terms of equation (3.6) refer to the solid angle error. Further details are shown at the appendix A.

The cross sections were determined via information of detectors placed at symmetrical positions as the weighted mean of σ/σ_{Ruth} ratio and its error were estimated, according to the following formulas [81]:

$$f_{mean} = \frac{\sum_i \left(f_i/\sigma_i^2 \right)}{\sum_i \left(1/\sigma_i^2\right)} \qquad (3.7)$$

$$\sigma_{mean} = \frac{1}{\sum_i \frac{1}{\sigma_i^2}} \qquad (3.8)$$

where $f = \sigma/\sigma_{Ruth}$ and σ_{mean} is the error on the weighted mean f_{mean}.

In some cases, an additional error term, due to the angle uncertainty (about ±2°), was necessary because in some angles the peak width was not accurately determined. The final results for σ/σ_{Ruth} ratio are presented at tables 3.5, 3.6 and 3.7 for the energies of 52.3, 42.5 and 70.0 MeV, respectively.

Table 3.5: *Ratio σ/σ_{Ruth} for the elastic scattering $^{28}Si(^{20}Ne,^{20}Ne)^{28}Si$ at bombarding energy of 52.3 MeV.*

Lab Energy of 52.3 MeV (E_{cm}=30.5MeV)				
θ_{lab} [deg]	θ_{cm} [deg]	σ/σ_{Ruth}	error	error %
20.00	**34.16**	**1.000E+00**	3.267E-02	3.27%
25.00	**42.60**	**1.299E+00**	5.552E-02	4.27%
27.00	**45.96**	**1.135E+00**	6.731E-02	5.93%
30.00	**50.96**	**1.098E+00**	6.517E-02	5.94%
33.00	**55.94**	**7.663E-01**	4.543E-02	5.93%
35.00	**59.23**	**7.032E-01**	4.177E-02	5.94%
37.00	**62.51**	**3.125E-01**	1.979E-02	6.33%
40.00	**67.38**	**2.236E-01**	8.270E-03	3.70%
45.00	**75.39**	**1.238E-01**	5.764E-03	4.65%
47.00	**78.55**	**8.614E-02**	5.475E-03	6.36%
50.00	**83.23**	**6.399E-02**	2.528E-03	3.95%
55.00	**90.87**	**2.980E-02**	2.370E-03	7.95%
57.00	**93.86**	**2.430E-02**	1.956E-03	8.05%
60.00	**98.27**	**2.273E-02**	1.217E-03	5.35%
62.00	**101.16**	**3.514E-02**	3.303E-03	9.40%
65.00	**105.40**	**1.735E-02**	1.309E-03	7.54%
67.00	**108.17**	**1.649E-03**	5.578E-04	33.82%
70.00	**112.22**	**8.917E-03**	1.383E-03	15.51%
75.00	**118.68**	**2.809E-03**	8.222E-04	29.27%

Table 3.6: *Ratio σ/σ_{Ruth} for the elastic scattering $^{28}Si(^{20}Ne,^{20}Ne)^{28}Si$ at bombarding energy of 42.5 MeV.*

Lab Energy of 42.5 MeV (E_{cm}=24.8MeV)				
θ_{lab} [deg]	θ_{cm} [deg]	σ/σ_{Ruth}	Error	Error %
20.00	**34.16**	**1.000**	0.057	5.67%
25.00	**42.60**	**1.082**	0.066	6.06%
30.00	**50.96**	**1.093**	0.084	7.64%
35.00	**59.22**	**1.131**	0.078	6.92%
40.00	**67.37**	**1.122**	0.074	6.57%
45.00	**75.38**	**0.850**	0.045	5.27%
50.00	**83.22**	**0.629**	0.039	6.12%
55.00	**90.86**	**0.472**	0.034	7.15%
60.00	**98.26**	**0.334**	0.027	7.96%
65.00	**105.39**	**0.164**	0.022	13.12%

Table 3.7: *Ratio σ/σ_{Ruth} for the elastic scattering $^{28}Si(^{20}Ne,^{20}Ne)^{28}Si$ at bombarding energy of 70.0 MeV.*

Lab Energy of 70.0 MeV (E_{cm}=40.8MeV)				
θ_{lab} [deg]	**θ_{cm} [deg]**	**σ/σ_{Ruth}**	**error**	**error %**
20.00	**34.16**	**1.000E+00**	4.000E-02	4.00%
25.00	**42.60**	**4.868E-01**	2.902E-02	5.96%
30.00	**50.96**	**1.490E-01**	8.954E-03	6.01%
35.00	**59.22**	**4.712E-02**	2.845E-03	6.04%
40.00	**67.38**	**1.425E-02**	7.304E-04	5.13%
45.00	**75.39**	**8.016E-03**	3.996E-04	4.99%
50.00	**83.23**	**3.257E-03**	1.691E-04	5.19%
55.00	**90.87**	**4.875E-03**	2.435E-04	4.99%
60.00	**98.27**	**4.020E-03**	2.579E-04	6.42%
65.00	**105.40**	**2.419E-03**	3.036E-04	12.55%
70.00	**112.22**	**9.991E-04**	5.559E-04	55.64%
75.00	**118.68**	**9.024E-04**	5.270E-04	58.40%

4. Theoretical analysis

The goal of the theoretical analysis was the deduction of the optical potential. For that, the experimental results were compared with calculations performed with the code ECIS[67], adopting various optical potentials as will be explained in detail below.

Initially, the Lee – Chan potential[51,57-58] and the Kobos – Satchler potential[7] were used, since these potentials were extracted from a similar system and energy range to ours. For the easiness of the procedure these potentials were fitted with a Woods – Saxon form factor[2] following a minimization procedure with the code PAW[85]. Subsequently by using the code ECIS, differential cross sections were calculated and compared with our elastic scattering data. Unfortunately, the calculated results were far out from the experimental ones.

Therefore, subsequently, we have proceeded with an analysis, adopting two phenomenological potentials of Woods – Saxon type, one with a deep depth and one with a shallow depth for the real part as well as a third potential adopting for the real part a microscopic BDM3Y1 interaction[72-74]. In all cases, the imaginary part was described by a Woods – Saxon form factor. For the fitting procedure and deduction of the macroscopic potentials in general the following steps were implemented in a minimization procedure with the code ECIS:

1. For the deep and shallow depth potentials the fit started taking into account for the real part the Lee – Chan[51,57-58] and the Christensen[71] potentials and fitting the three parameters for the imaginary part. So, the imaginary part was deduced freely fitting the experimental data.
2. Changing manually in small steps the depth of the real part, the previous step was repeated until we have achieved a reasonable fit to the experimental data.
3. Finally, in order to optimize the fit, we changed manually the depth of the imaginary part.

For the third potential, where a microscopic interaction was adopted, we added to the real part an imaginary Woods – Saxon form factor. Initially, a fit was performed with free parameters the normalization factor and the depth of the imaginary part, while in a second step the other two parameters were freely fitted. The best fitted normalization factors of the real part was N_V=0.484 for 42.5 MeV, N_V=0.351 for 52.3 MeV and N_V=0.198 for 70.0 MeV. Additionally, for the easiness of the reader, the BDM3Y1 interaction was parameterized with a Woods – Saxon form factor and changing the parameters of the imaginary part a new fit was performed.

4.1. ^{20}Ne+^{28}Si elastic scattering at 52.3 MeV

The experimental results at 52.3 MeV were compared with different calculations performed with the code ECIS.

4.1.1. The macroscopic potentials

The deep potential (Set 1)

The elastic scattering data were compared with an optical model calculation based on a phenomenological Woods – Saxon potential consisted of a real and an imaginary volume part. In the fit to the experimental data, as initial values to the Woods – Saxon form factor were taken parameters obtained by the Lee – Chan potential using the methodology, described in the previous chapter. The deduced parameters of this deep potential are shown in table 4.2 under the label Set 1, while the calculated cross sections are compared with the data in Figure 4.1.

The shallow potential (Set 2)

A second calculation was also performed using as initial values for the real volume part the term obtained by fitting the (pure real) global Christensen potential with a Woods – Saxon form factor (table 4.1). Using the same methodology as before a shallow potential was obtained. The results of the optical model calculation are presented in figure 4.1 while, the relevant parameters are presented at table 4.2 under the label Set 2.

4.1.2. The BDM3Y1 microscopic potential (Set 3 and Set 4)

The experimental data were also compared with an optical model calculation using for the real part the BDM3Y1 microscopic interaction[72-74]. Using the ECIS code a fit was performed with two free parameters: the normalization factor in the real part and the depth of the Woods-Saxon imaginary part. In a second step the other two parameters of the imaginary part (radius, diffusivity) were freely fitted. The best fit for the energy of 52.3 MeV gave a normalization factor equal to 0.351. The parameters for the imaginary part are presented at table 4.2 (Set 3).

After that, for convenience of the reader, the BDM3Y1 interaction was parameterized with a Woods – Saxon form factor using the program PAW. Unfortunately, a Woods – Saxon form factor is not able to fit exactly, the BDM3Y1 interaction. Therefore a fit to the elastic scattering data, changing the imaginary parameters, was also performed and the results are presented as set 4 to table 4.2.

4.1.3. The bare potential (Set 5)

Finally, an optical potential, describing the behavior of the first data points, was extracted from these data and was taken as the bare potential that is the potential without couplings to other degrees of freedom. This was done, taking the parameters of the real part from Set 1 and adjusting the imaginary part to the first

13 experimental data points. It is very interesting to note that this obtained potential is capable for describing the behavior of the first data points at all energies. The results for the energies 52.3 MeV, 70.0 MeV and 42.5 MeV are presented in figures 4.1, 4.9 and 4.11, respectively, while the parameters are presented at table 4.2 as Set 5.

The optical model calculations adopting the sets mentioned above are presented in figure 4.1. It is obvious that, at forward angles all the potentials provide equivalent fits to the data, while at more backward angles, where the cross section appears an anomalous increase, only the calculation based on the BDM3Y1 interaction (Set 3 and Set 4) presents the appropriate phase. In all three cases, the depth of the imaginary part of the potential was shallow, indicating that peripheral reactions may be the most dominant. Also, it should be noted that, in order to optimize the fits, a surface real term was taken into account but, with no important impact to the calculation, probably due to the limited angular range of the experimental data. So, this term was not further considered.

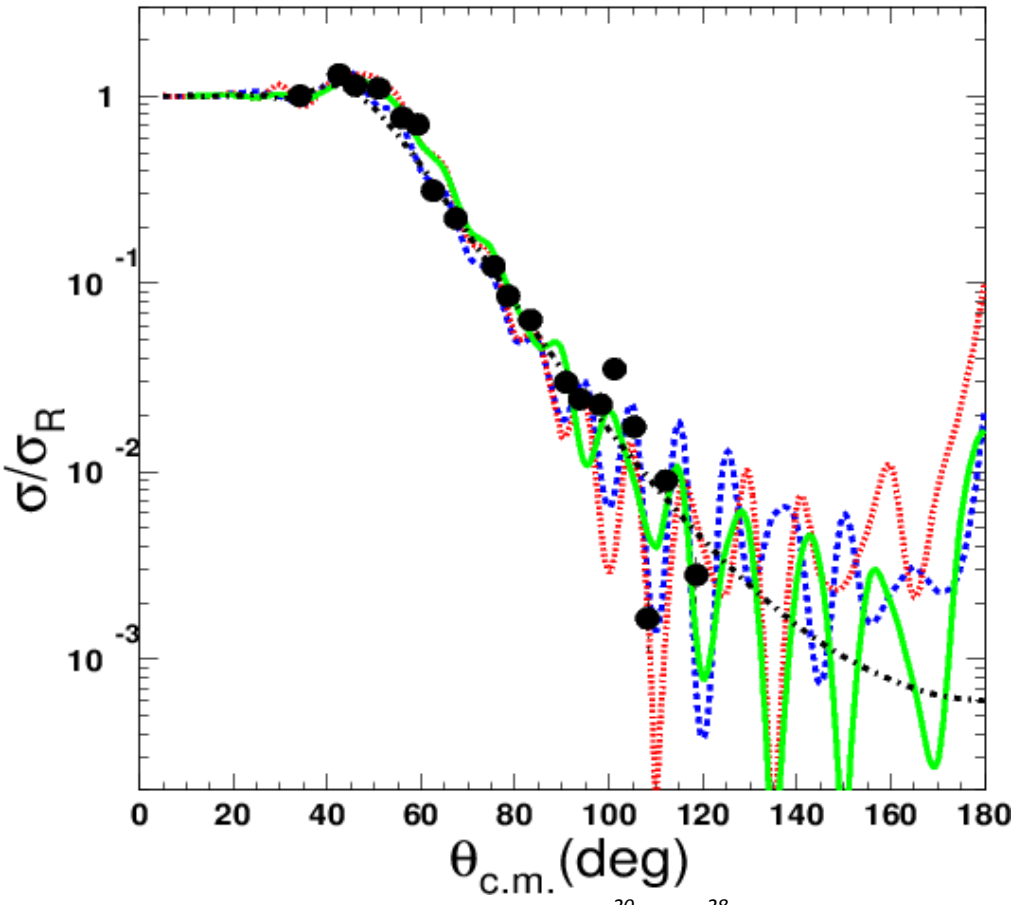

Figure 4.1: *Elastic scattering data for the system ^{20}Ne + ^{28}Si at energy of 52.3 MeV are compared with phenomenological calculations. Results using Sets 1, 2 and 3 are denoted with the blue dashed, the red dotted and the green solid line respectively, while the prediction using a bare potential is denoted with the black dashed – dotted line.*

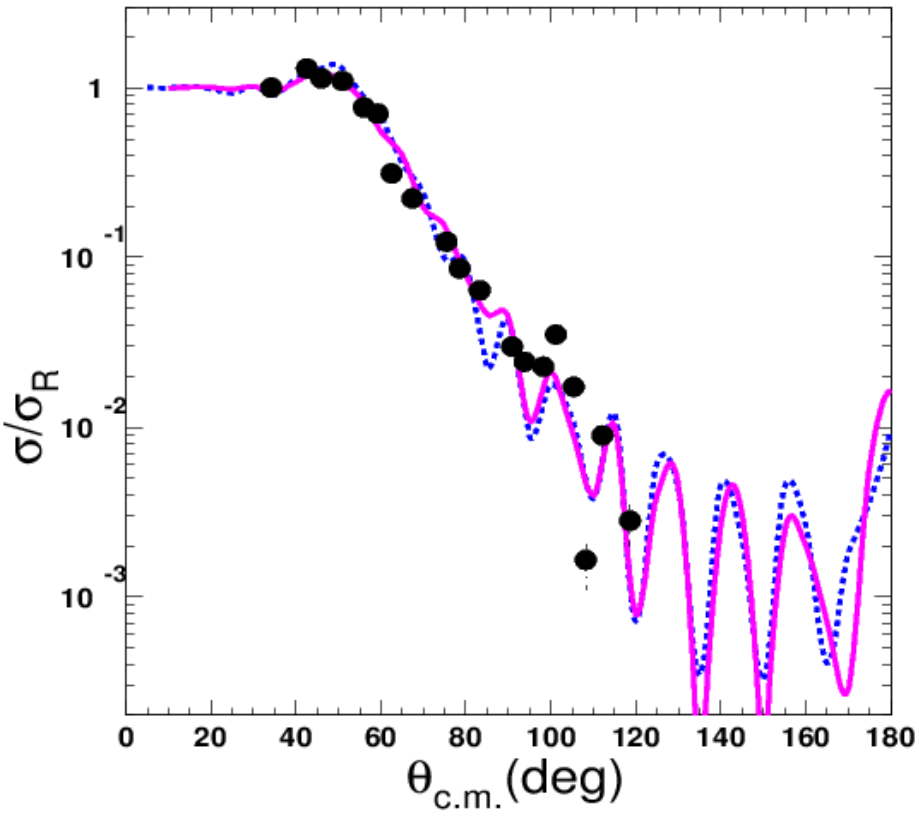

Figure 4.2: *Angular distribution data for the system ^{20}Ne + ^{28}Si at energy of 52.3 MeV are compared with optical model calculations. Results using Set 3 and Set 4 are denoted with the magenta solid line and the blue dashed line, respectively.*

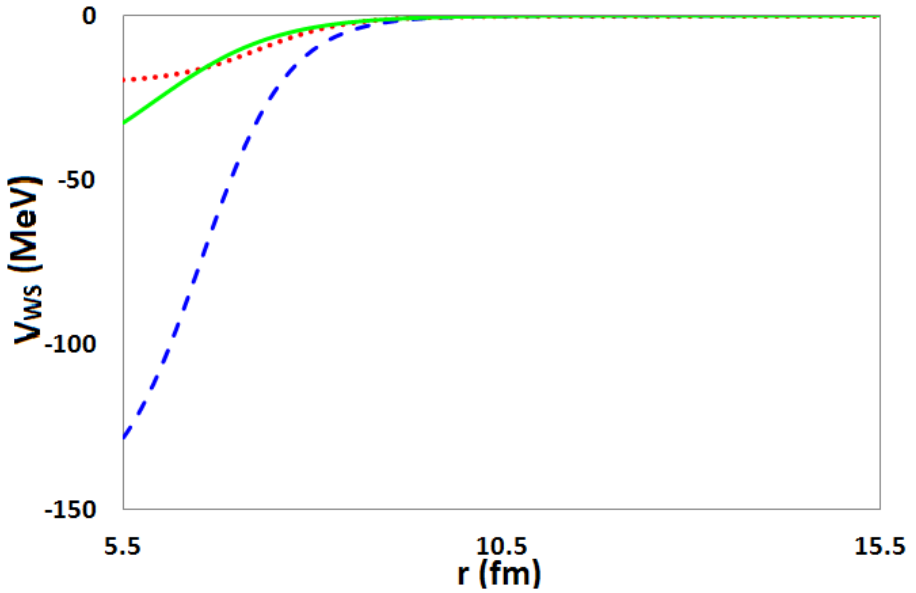

Figure 4.3: *A comparison between the real part of an optical potential using a Woods – Saxon form factor for the system ^{20}Ne + ^{28}Si at energy of 52.3 MeV. The real parts of Set 1, 2 and 4 are denoted with the blue dashed, the red dotted and the green solid line, respectively.*

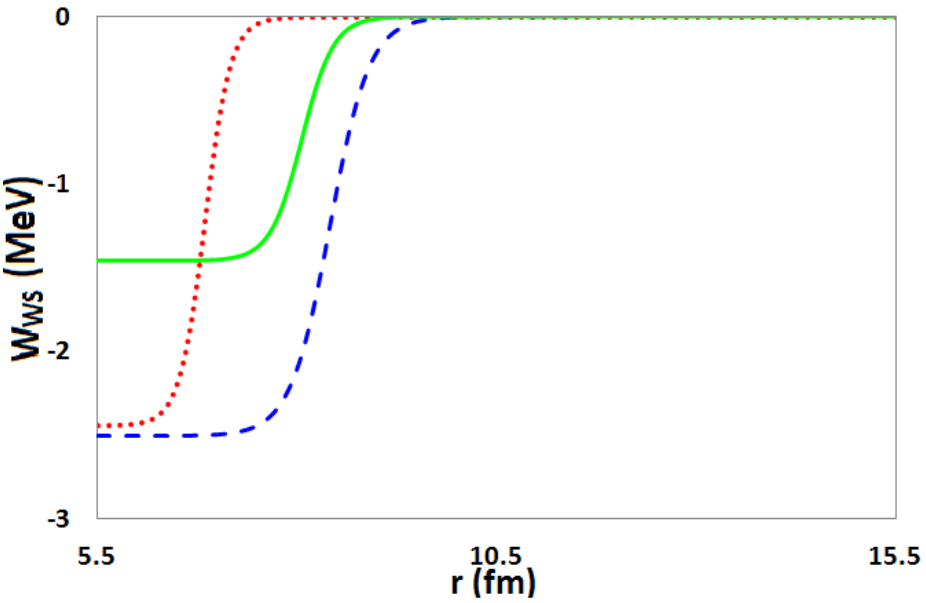

Figure 4.4: *A comparison between the imaginary part of an optical potential using a Woods – Saxon form factor for the system $^{20}Ne + ^{28}Si$ at energy of 52.3 MeV. The imaginary parts of Set 1, 2 and 4 are denoted with the blue dashed, the red dotted and the green solid line, respectively.*

4.1.4. Sensitivity test

As it was mentioned in chapter 1.8, both discrete and continuous ambiguities may exist in an optical model determination with Woods-Saxon form factors. As to determine the sensitive radial range, where the deep or the shallow potential is unique, the "Crossing point method"[23,76-78] was applied.

In particular, working separately for the real and the imaginary part of the Woods – Saxon potential (formula 1.48), it is easy to determine the sensitive radial range using this method. So, with the code ECIS, a free search for V_0 and R_v is performed, for a standard value of diffusivity α_v. This procedure must be repeated by changing the diffusivity, for example, in steps of 0.05 fm. Then, for the sets of parameters with the best χ^2 values, we calculated the V_{WS} quantity (formula 1.48) within the radial range from 0.1 to 20.0 fm in steps of 0.1 fm. The same procedure was applied to the imaginary part of the potential.

So, the V_{WS} and the W_{WS} quantities adopting the deep potential, as a function of radius r are presented in figures 4.5 and 4.6. The crossing point appears at 5.50 fm for the real part while, the sensitive radial range is approximately 8.40 fm for the imaginary part.

On the other hand, these quantities for the shallow potential, as a function of radius r in the sensitive radial range are presented in figures 4.7 and 4.8. The crossing point or the sensitive radius is about 8.04 fm for the real part V_{WS} while, it appears at 6.90 fm for the imaginary part W_{WS}.

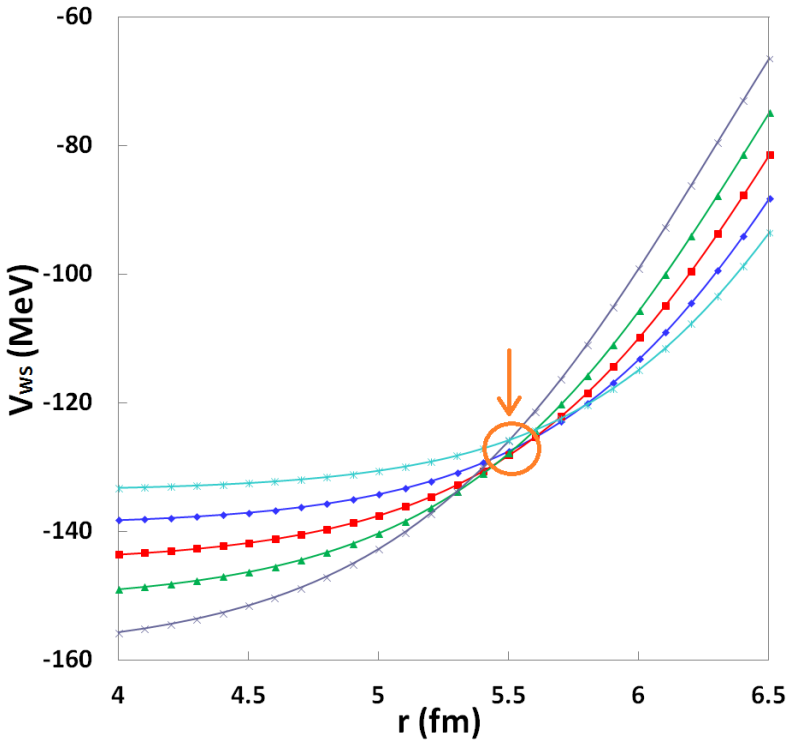

Figure 4.5: *The real part of the deep potential (Set 1) for the system $^{20}Ne+^{28}Si$, as a function of radius for five different values of the diffusivity α: 0.52, 0.54, 0.56, 0.58 and 0.60 is denoted with the turquoise blue, blue, red, green and violet line, respectively. The circled area presents the crossing point appeared at r=5.50 fm.*

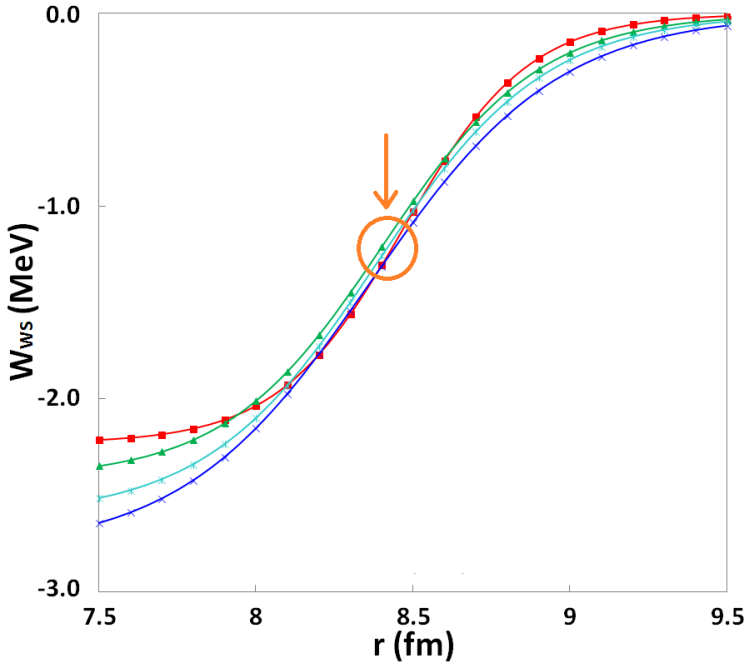

Figure 4.6: *The imaginary part of the deep potential (Set 1) for the system $^{20}Ne+^{28}Si$, as a function of radius for four different values of the diffusivity α: 0.20, 0.25, 0.27 and 0.30 is denoted with the red, green, turquoise blue and blue line, respectively. The circled area presents the crossing point appearing at about 8.40 fm.*

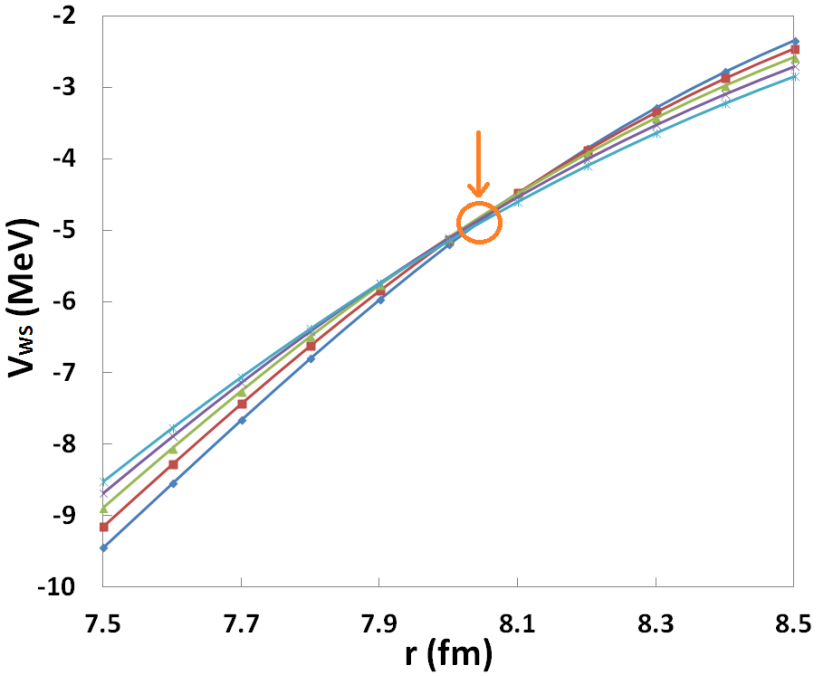

Figure 4.7: *The real part of the shallow potential for the system $^{20}Ne+^{28}Si$, as a function of radius for five different values of the diffusivity α: 0.50, 0.55, 0.60, 0.65 and 0.70 is denoted with the blue, red, green, violet and turquoise blue line, respectively. The circled area presents the crossing point appearing at r=8.04 fm.*

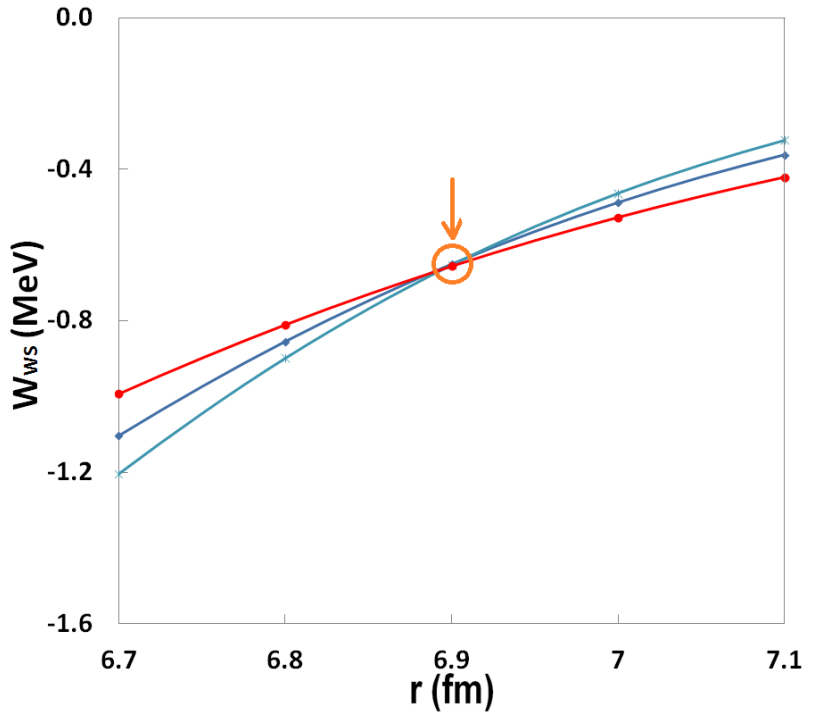

Figure 4.8: *The imaginary part of the shallow potential for the system $^{20}Ne+^{28}Si$, as a function of radius for three different values of the diffusivity α: 0.25, 0.30 and 0.40 is denoted with the turquoise blue, blue and red line, respectively. The circled area presents the crossing point appeared at r=6.90 fm.*

4.2. ^{20}Ne+^{28}Si elastic scattering at 70.0 MeV

The experimental results at the energy of 70 MeV were also compared with optical model calculations using the phenomenological potentials from the previous energy of 52.3 MeV (Figure 4.9). The transition from the energy of 52.3 MeV to 70.0 MeV, using Set 1 and Set 2, required a small variation to the potential. In particular, the most important change was an increase of the depth of the imaginary part. The new results are presented at table 4.2 and in figure 4.9. It is seen that the fits are not very good. The difficulty to fit the experimental data at this high energy occurs, probably due to an unexpected resonance in this energy region. This fact makes necessary the existence of many more experimental data.

Also, fits adopting Set 3 and Set 4 are presented in figure 4.10. It is obvious that, each set provides a different fit to the data. A reasonable explanation is that the Woods – Saxon form factor is not able to fit the BDM3Y1 interaction well enough.

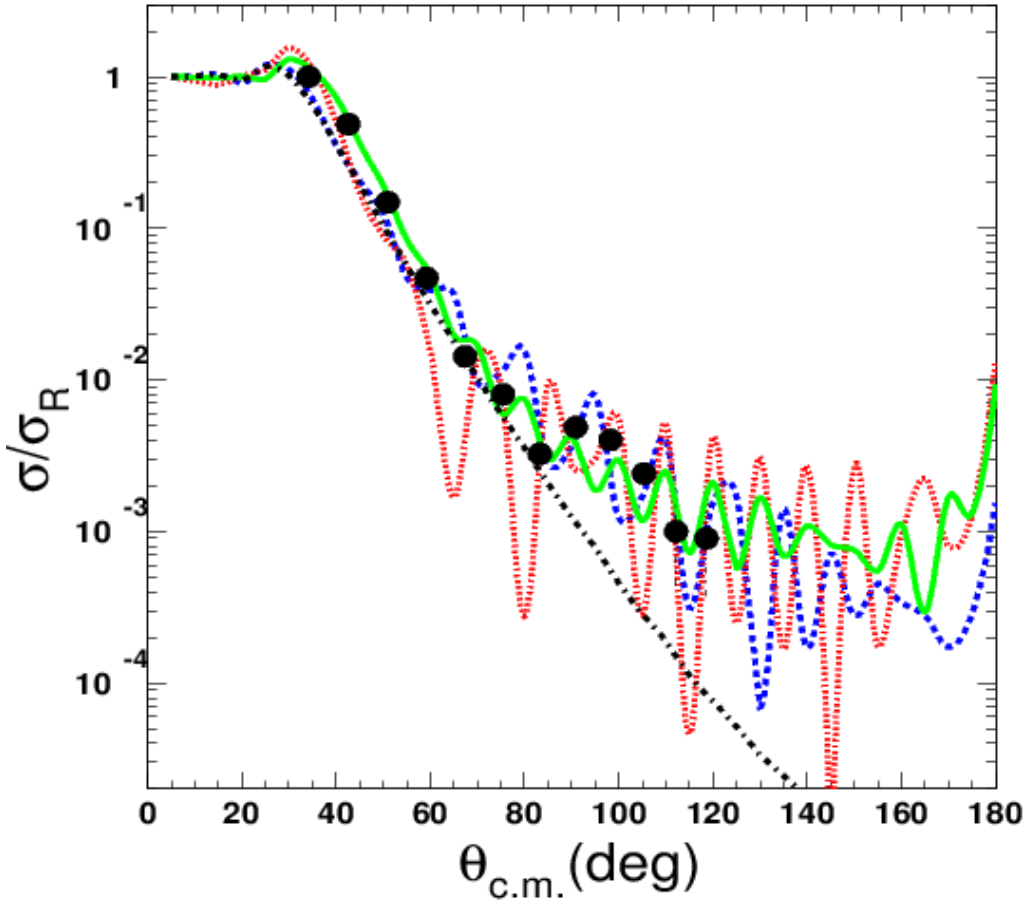

Figure 4.9: *Elastic scattering data for ^{20}Ne + ^{28}Si at energy of 70.0 MeV are compared with phenomenological calculations. Results using the Sets 1, 2 and 3 are denoted with the blue dashed, the red dotted and the green solid line respectively, while the results using a bare potential are denoted with the black dashed – dotted line.*

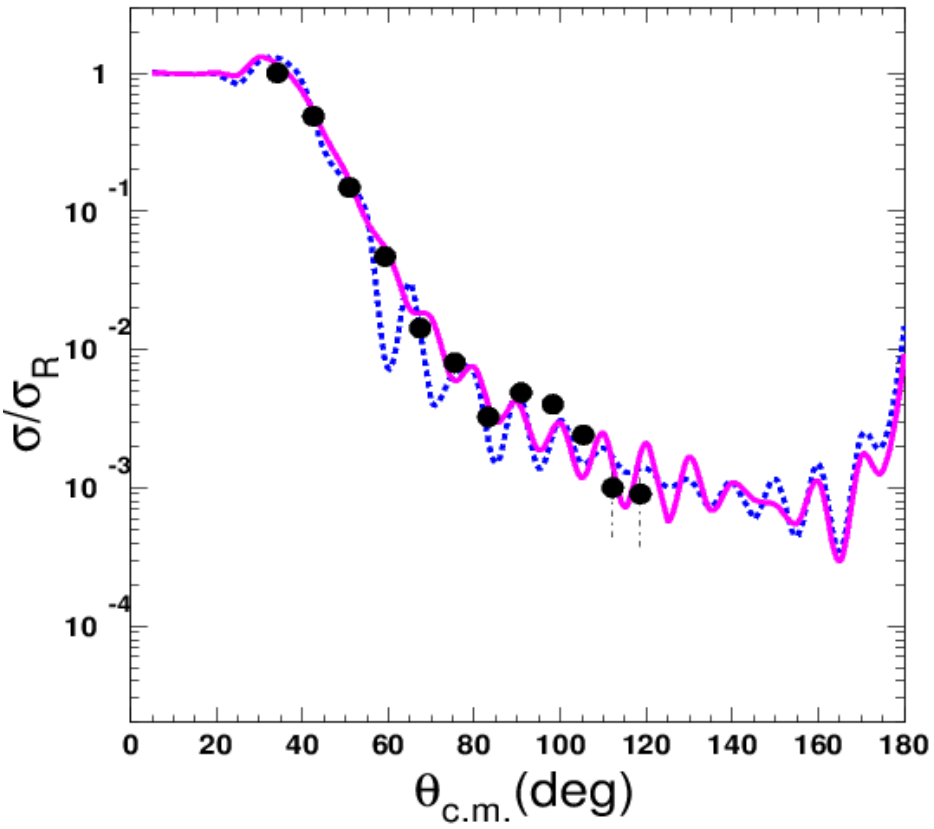

Figure 4.10: *Angular distribution data for the system ^{20}Ne + ^{28}Si at energy of 70.0 MeV are compared with optical model calculations. Results using Set 3 and Set 4 are denoted with the magenta solid line and the blue dashed line, respectively.*

4.3. ^{20}Ne+^{28}Si elastic scattering at 42.5 MeV

Finally, the data at the low energy of 42.5 MeV are compared with optical model calculations based on the potentials extracted from the data at 52.3 MeV. It should be noted that the deep potential was adequate for describing these data, while for the shallow one, some changes were necessary (table 4.2).

In this low energy, using the shallow potential, our calculations did not predict any oscillating behavior but, using the deep one, an oscillating behavior appears. Unfortunately, this prediction cannot be confirmed experimentally, due to the lack in data at backward angles (Figure 4.11). Finally, a comparison between the fits using Set 3 and Set 4 is presented in figure 4.12.

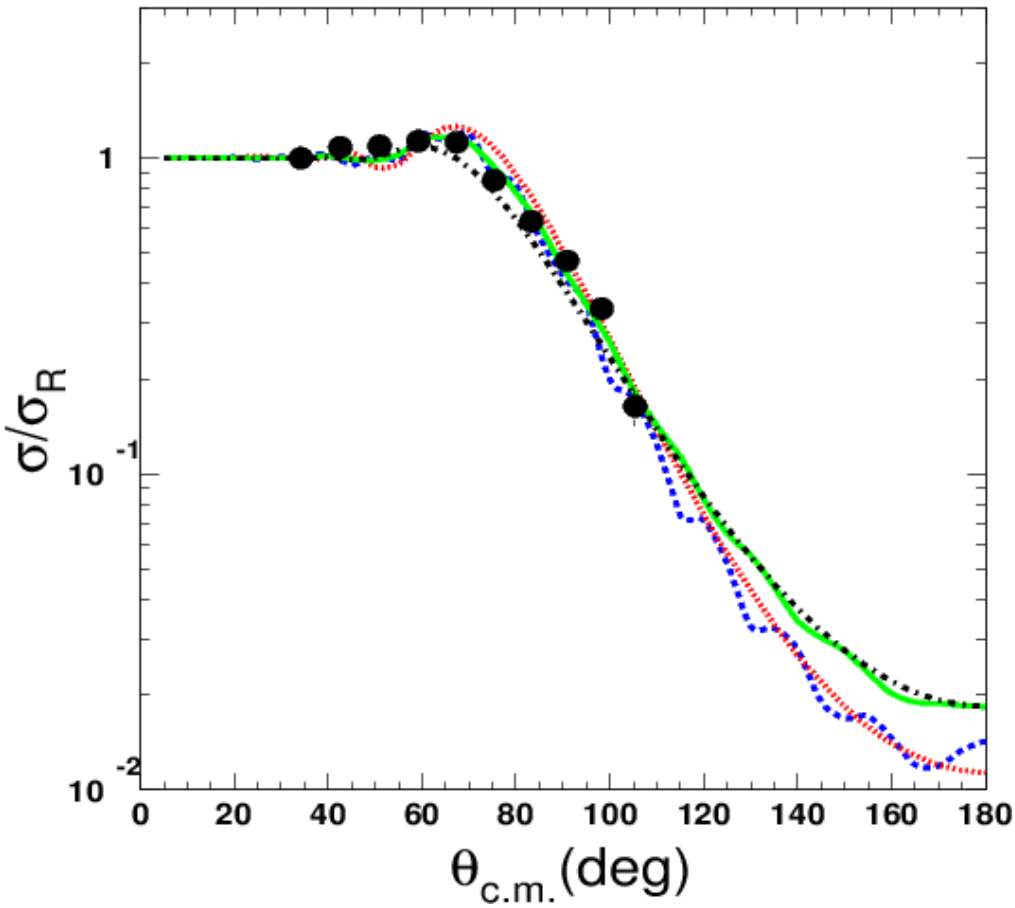

Figure 4.11: *Elastic scattering data for ^{20}Ne + ^{28}Si at energy of 42.5 MeV are compared with phenomenological calculations. Results using the Sets 1, 2 and 3 are denoted with the blue dashed, the red dotted and the green solid line respectively, while the results using a bare potential are denoted with the black dashed – dotted line.*

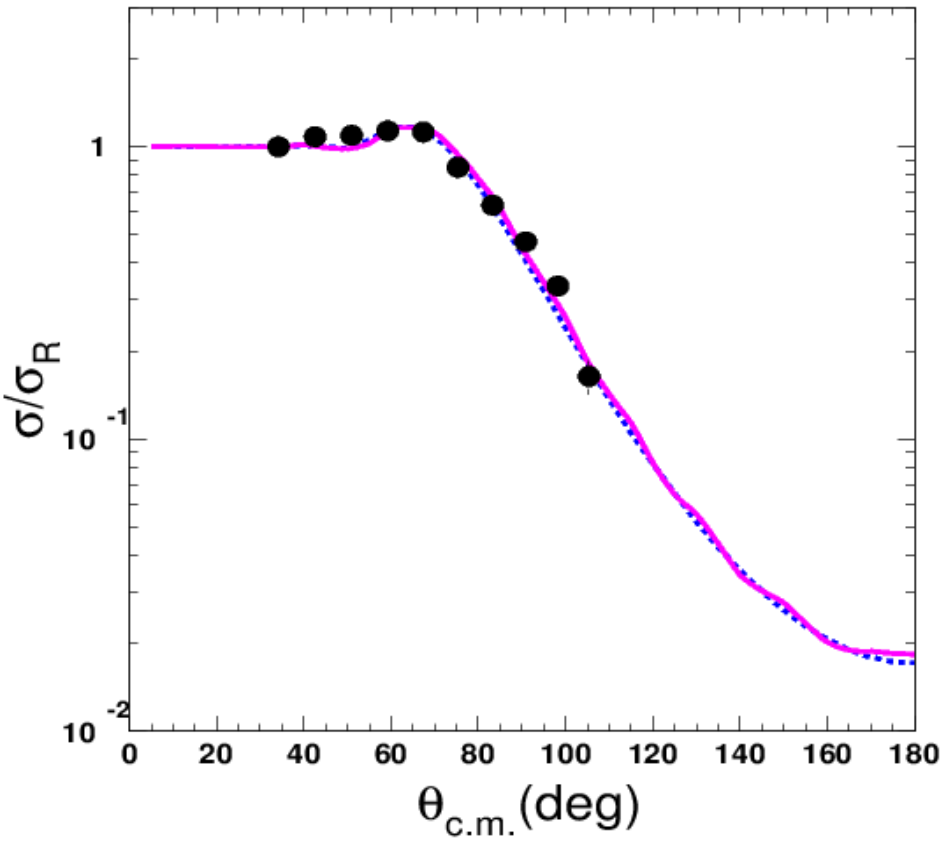

Figure 4.12: *Angular distribution data for the system ^{20}Ne + ^{28}Si at energy of 42.5 MeV are compared with optical model calculations. Results using Set 3 and Set 4 are denoted with the magenta solid line and the blue dashed line, respectively.*

Table 4.1: *The Lee – Chan and the Christensen potential for ^{20}Ne+^{28}Si. These values were obtained by fitting the potential with a Woods – Saxon form factor.*

Potential	Energy (MeV)	REAL Volume			IMAGINARY Volume		
		V (MeV)	R_v (fm)	a_v(fm)	W (MeV)	R_w (fm)	a_w(fm)
Lee – Chan		178.43	1.133	0.575	12.27	1.133	0.575
Christensen		20.41	1.268	0.570			

Table 4.2: *Optical model parameters, used in the present calculation, at 42.5, 52.3 and 70.0 MeV. Set 1 and 2 include parameters from a best fit with initial values taken from Lee – Chan and Christensen potential, respectively. Set 3 includes the parameters of the imaginary part of the potential deduced while using for the real part a BDM3Y1 interaction. The best fitted normalization factors of the real part was N_V=0.484 for 42.5 MeV, N_V=0.351 for 52.3 MeV and N_V=0.198 for 70.0 MeV. The BDM3Y1 interaction was also approximated with a Wood's Saxon form factor and the results are shown as set 4 while, Set 5 includes the parameters for the bare potential. The χ^2 value is also presented in the last column.*

Potential	Energy (MeV)	REAL Volume			IMAGINARY Volume			
		V (MeV)	R_V (fm)	a_V(fm)	W (MeV)	R_W (fm)	a_W(fm)	χ^2
Set 1	**42.5**	150.00	1.133	0.575	2.50	1.464	0.248	12.7
	52.3	150.00	1.133	0.575	2.50	1.464	0.248	299
	70.0	150.00	1.133	0.575	3.90	1.530	0.248	8.6
Set 2	**42.5**	20.41	1.298	0.570	4.44	1.190	0.160	19.2
	52.3	20.41	1.268	0.570	2.44	1.190	0.160	595
	70.0	20.41	1.238	0.570	4.84	1.190	0.160	5.2
Set 3	**42.5**				3.016	1.493	0.309	7.0
	52.3				2.162	1.493	0.309	144
	70.0				2.462	1.393	0.309	2.8
Set 4	**42.5**	63.77	1.005	0.871	3.150	1.493	0.309	8.6
	52.3	52.77	1.023	0.816	1.458	1.403	0.198	183
	70.0	32.60	1.002	0.828	1.102	1.393	0.309	19.2
Set 5	**42.5**	150.00	1.133	0.575	11.00	1.444	0.438	15,8
	52.3	150.00	1.133	0.575	11.00	1.444	0.438	32.6*****
	70.0	150.00	1.133	0.575	11.00	1.444	0.438	11.8*****

** adjusting to the first data points*

4.4. ^{20}Ne+^{28}Si elastic scattering: CRC calculations

The elastic scattering data were also analyzed in the Coupled Reaction Channels (CRC) framework by Dr. N.Keeley[62] using the code FRESCO[63]. To achieve that, the following partitions were included:

- Inelastic excitation of the 1.63 MeV 2+ state of ^{20}Ne,
- Inelastic excitation of the 4.25 MeV 4+ state of ^{20}Ne,
- Inelastic excitation of the 5.62 MeV 3– state of ^{20}Ne,
- Inelastic excitation of the 1.78 MeV 2+ state of ^{28}Si,
- Inelastic excitation of the 4.62 MeV 4+ state of ^{28}Si,
- Inelastic excitation of the 6.88 MeV 3– state of ^{28}Si,
- α particle pickup to the ^{24}Mg+^{24}Mg partition,
- α particle stripping to the ^{16}O+^{32}S partition,
- Sequential α particle pickup ^{28}Si(^{20}Ne,^{24}Mg)^{24}Mg ; ^{24}Mg(^{24}Mg, ^{28}Si)^{20}Ne,
- Sequential α particle stripping ^{28}Si(^{20}Ne, ^{16}O)^{32}S ; ^{32}S(^{16}O, ^{12}C)^{36}Ar,
- Inelastic excitation of the 1.37 MeV 2+ state of ^{24}Mg,
- Inelastic excitation of the 2.23 MeV 2+ state of ^{32}S,

- Inelastic excitation of the 4.44 MeV 2+ state of ^{12}C,
- Inelastic excitation of the 1.97 MeV 2+ state of ^{36}Ar,
- Elastic transfer of a whole ^{8}Be cluster and
- Direct stripping of a whole ^{8}Be cluster to the $^{12}C+^{36}Ar$ partition.

The optical model potentials in all partitions consisted of double folded real parts, using the M3Y interaction[75], and Woods – Saxon form factors for the imaginary parts. The imaginary parts were obtained by fitting the experimental data at energies of 42.5 and 52.3 MeV.

The data at 52.3 MeV are well described by the calculations but, the phase of some oscillations is not reproduced. Apart from that, only the inclusion of a whole ^{8}Be transfer process could produce this oscillatory structure of the data. Similar calculations predict an oscillatory structure for the angular distribution of 42.5 MeV. Such behavior has been observed at similar energies in the system $^{12}C+^{24}Mg$, and it has been suggested that it is due to an elastic transfer process[32].

In summary, Coupled Reaction Channel calculations were performed to interpret the experimental data. These calculations might therefore be considered to suggest significant ^{8}Be clustering in the ground states of ^{20}Ne, ^{28}Si, and ^{36}Ar. However, the following reasons seem to rule out this possibility:

1. The large ^{8}Be separation energies for these nuclei and
2. The spectroscopic amplitudes for the $<^{20}Ne|^{12}C + ^{8}Be>$ and $<^{28}Si|^{20}Ne + ^{8}Be>$ overlaps, required to give the best description of the data, are much larger than calculated values from the literature.

The available data evidence that the origin of the observed structure may be the compound nucleus effects rather than cluster transfer.

Finally, for the energy of 70.0 MeV, CRC calculations were also performed but, the compatibility between calculated and experimental cross sections was not satisfactory maybe due to the contribution of compound nucleus effects.

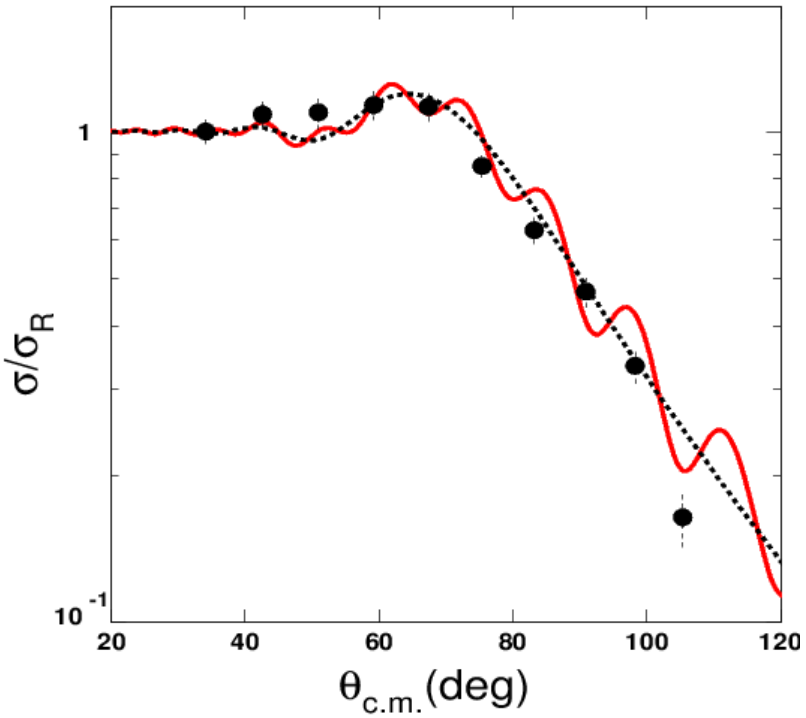

Figure 4.13: *CRC calculation compared with elastic scattering data for the system ^{20}Ne + ^{28}Si at the energy of 42.5 MeV. The red solid line denote the full calculation while, the black dashed line the calculation that do not include direct ^{8}Be-cluster elastic transfer (figure from private communication with N. Keeley).*

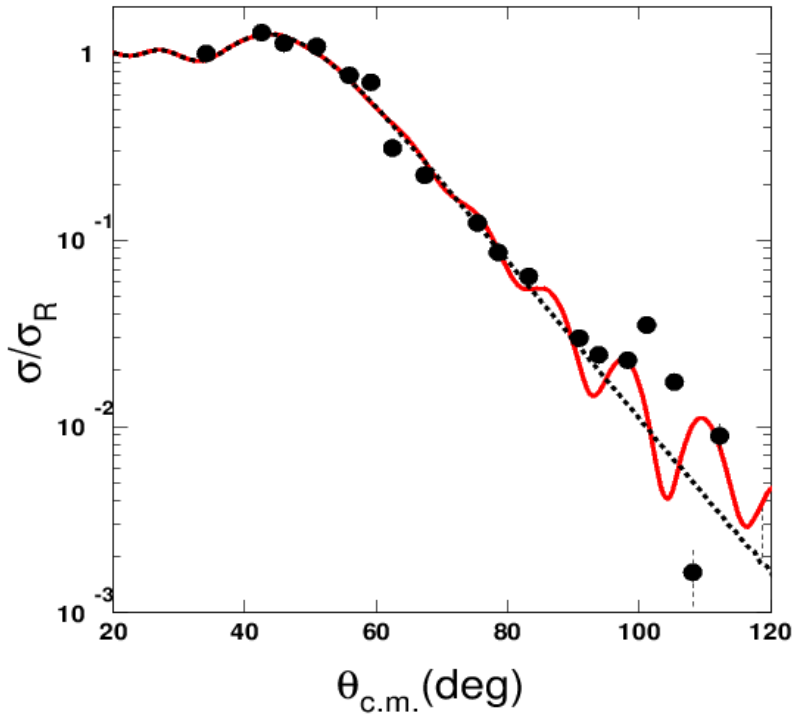

Figure 4.14: *CRC calculations compared with elastic scattering data for the system ^{20}Ne + ^{28}Si at the energy of 52.3 MeV. The red solid line denote the full calculation while, the black dashed line the calculation that do not include direct ^{8}Be-cluster elastic transfer (figure from private communication with N. Keeley).*

5. Conclusions

In summary, from the study of ^{20}Ne + ^{28}Si elastic scattering at energies E_{Lab}=42.5, 52.3 and 70.0 MeV, the following conclusions can be drawn:

1. At backward angles an anomalous raising of the differential cross sections is observed with oscillating trend, similar to the one presented by the lighter projectiles ^{12}C and ^{16}O.
2. Macroscopic potentials deduced by fitting similar data, like for example the Lee – Chan, or global potentials as the Christensen one were not adequate for explaining the oscillating behavior at backward angles. New potentials were deduced based on Woods-Saxon form factors, one with a deep and one with a shallow depth. The results were in favor of the shallow depth potential while the appropriate phase at least for the data at 52.3MeV was only described adopting for the real part of the optical potential, a microscopic – BDM3Y1 interaction.
3. The results from a sensitivity test based on the crossing point method, showed that for the shallow phenomenological potential the sensitive radius of the real part is bigger than the one of the imaginary part. On the other hand, for the deep optical potential, the sensitive radial range seems smaller than the systematic behavior of the other systems.
4. The data were described adopting the same optical potential for all three energies but with small variations, mainly at the imaginary part of it.
5. The oscillating behavior appears at energy of 52.3 MeV after $\theta_{c.m.}$~90^o while, at energy of 70.0 MeV from $\theta_{c.m.}$~70^o. At the lower energy of 42.5 MeV such a behavior cannot be confirmed due to the lack of experimental data at backward angles.
6. Coupled Reaction Channels calculations, performed by Nick Keeley, present evidence that the elastic transfer process is the main mechanism to produce the oscillatory structure of the data. However, the unusual large spectroscopic amplitudes evidence that the compound nucleus effects are also significant.

On the other hand, we can't ignore the fact that: the total errors were significant and the angular distributions were limited to a selected angular range with a poor angular resolution. Taking into consideration all the above, we conclude that a further investigation of that system is necessary, both theoretically and experimentally. From the experimental point of view it is necessary for obtaining precise cross sections at several energies and especially several angles. This can be achieved by doing the measurement in inverse kinematics and using for a good angular resolution a magnetometer.

References – Bibliography

1. *H. Feshbach,* ***Annals of Physics 5****, 357 (1958).*
2. *P. E. Hodgson,* ***Rep. Prog. Phys. 34****, 765 (1971).*
3. *G. R. Satchler and W. G. Love,* ***Phys. Reports 55****, 183 (1979).*
4. *P. Braun – Munzinger and J. Barrette,* ***Phys. Reports 87****, 209 (1982).*
5. *U. C. Voos et al.,* ***Nucl. Phys. A 135****, 207 (1969).*
6. *G. R. Satchler,* ***Nucl. Phys. A 279****, 493 (1977).*
7. *A. M. Kobos and G.R.Satchler,* ***Nucl. Phys. A 427****, 589 (1984).*
8. *W. Sciani et al.,* ***Nucl. Phys. A 620****, 91 (1997).*
9. *G. S. Mallick et al.,* ***Phys. Rev. C 73****, 054606 (2006).*
10. *E. J. Burge et al.,* ***Proc. Phys. Soc. 81****, 832 (1963).*
11. *Y. -M. You et al.,* ***Wuli Xuebao/Acta Physica Sinica 61****, 202401 (2012).*
12. *F. Schmittroth et al.,* ***Phys. Rev. C 1****, 377 (1970).*
13. *J. C. Peng et al.,* ***Nucl. Phys. A 264****, 312 (1976).*
14. *M. Paul et al.,* ***Phys. Rev. Lett. 40****, 1310 (1978).*
15. *http://www.uoi.gr/physics/npl/profile.htm*
16. *A. Pakou et al.,* ***Phys. Lett. B 556****, 21 (2003).*
17. *A. Pakou et al.,* ***Phys. Rev. Lett. 90****, 202701 (2003).*
18. *A. Pakou et al.,* ***Phys. Rev. C 69****, 054602 (2004).*
19. *A. Pakou et al.,* ***Phys. Rev. C 69****, 057602 (2004).*
20. *A. Pakou et al.,* ***Phys. Rev. C 71****, 064602 (2005).*
21. *A. Pakou et al.,* ***Journal of Phys. G 31****, S1723 (2006).*
22. *A. Pakou et al.,* ***Phys. Lett B 633****, 691 (2006).*
23. *D. Roubos et al.,* ***Phys. Rev. C 73****, 051603 (2006).*
24. *A. Pakou et al.,* ***Nucl. Phys. A 784****, 13 (2007).*
25. *A. Pakou et al.,* ***Phys. Rev. C 76****, 054601 (2007).*
26. *A. Pakou et al.,* ***Phys. Rev. C 78****, 067601 (2008).*
27. *A. Pakou et al.,* ***Eur. Phys. Journal A 39****, 187 (2009).*
28. *K. Zerva et al.,* ***Phys. Rev. C 80****, 017601 (2009).*
29. *K. Zerva et al.,* ***Phys. Rev. C 82****, 044607 (2010).*
30. *K. Zerva et al.,* ***Eur. Phys. Journal A 48****, 102 (2012).*
31. *A. Pakou et al.,* ***Phys. Rev. C 87,*** *014619 (2013).*
32. *A. Lépine – Szily et al.,* ***Phys. Rev. Lett. 82****, 3972 (1999).*
33. *F. Hoyle,* ***Astrophys. J. Suppl.1****, 121 (1954).*
34. *M. Itoh et al.,* ***Phys. Rev. C 84,*** *054308 (2011).*
35. *E. Epelbaum et al.,* ***Phys. Rev. Lett. 109****, 252501 (2012).*
36. *R. C. Fouler,* ***Phys. Rev. C 12****, 1561 (1975).*
37. *B. V. Carlson and M. P. Isidro Filho,* ***Phys. Lett. B 154****, 89 (1985).*
38. *A. Ohnishi et al.,* ***Nucl. Phys. A 538****, 429 (1992).*

39. *M. Hussein et al.,* ***Journal of Physics: Conference Series 420,*** *012069 (2013).*
40. *M. S. Hussein and K. W. McVoy,* ***Progr. Part. Nucl. Phys. 12****, 103 (1984).*
41. *W. von Oertzen et al.,* ***Phys. Reports 432****, 43 (2006).*
42. *W. von Oertzen,* ***Progr. Theor. Phys. 146****, 169 (2002).*
43. *W. von Oertzen,* ***Intern. Journal of Modern. Phys. E 20****, 765 (2011).*
44. *R. Lichtenthaler et al.,* ***Phys. Rev. C 26,*** *2487 (1982).*
45. *W. von Oertzen et al.,* ***Phys. Lett. B 26****, 291 (1968).*
46. *W. von Oertzen and H.G. Bohlen,* ***Phys. Reports 19****, 1 (1975).*
47. *A. Lépine – Szily et al.,* ***Phys. Lett. B 304****, 45 (1993).*
48. *N. Takigawa et al.,* ***Nucl. Phys. A 787****, 190c (2007).*
49. *M. C. Morais and R. Lichtenthaler,* ***Nucl. Phys. A 857****, 1 (2011).*
50. *C. K. Gelbke et al.,* ***Phys. Rev. Lett. 41****, 1778 (1978).*
51. *S. Y. Lee and Y-D Chan,* ***University of Washington preprint RLO–1388-743, unpuplished*** *(1977).*
52. *P. Braun – Munzinger et al,* ***Phys. Rev. C 24****, 1010 (1981).*
53. *A. M. Kobos et al.,* ***Nucl. Phys. A 395****, 248 (1983).*
54. *S. Kahana et al.,* ***Phys. Rev. C 28****, 1393 (1983).*
55. *M. El-Azab Farid et al,* ***Nucl. Phys. A 691****, 671 (2001).*
56. *I. Boztosun,* ***Phys. Rev. C 66****, 024610 (2002).*
57. *S.K. Agarwalla et al,* ***J. Phys. G: Nucl. Part. Phys. 32,*** *165 (2006).*
58. *S. Y. Lee,* ***Nucl. Phys. A 311****, 518 (1978).*
59. *S. Kubono et al.,* ***Phys. Lett. B 81****, 140 (1979).*
60. *http://www.slcj.uw.edu.pl*
61. *J. Jastrzębski,* ***Acta Physica Polonica B 40****, 839 (2009).*
62. *N. Keeley, private communication.*
63. *I.J. Thompson,* ***Comput. Phys. Rep. 7****, 167 (1988).*
64. *S. Jan et al.,* ***Phys. Med. Biol. 49****, 4543 (2004).*
65. *E. Stiliaris, private contact.*
66. *http://www.opengatecollaboration.org*
67. *J. Raynal,* ***Phys. Rev. C 23****, 2571 (1981).*
68. *Samuel S. M. Wong, Introductory Nuclear Physics, Wiley-VCH Verlag GmbH &Co. KGaA., 2nd edition (2004).*
69. *R. R. Roy and B. P. Nigam, Nuclear Physics Theory and Experiment, John Wiley and Sons, Inc. (1967).*
70. *H. Feshbach et al.,* ***Phys. Rev. 96****, 448 (1954).*
71. *P. R. Christensen and A. Winther,* ***Phys. Lett. B 65****, 19 (1976).*
72. *D. T. Khoa and W. von Oertzen,* ***Phys. Lett. B 304****, 8 (1993).*
73. *N. Alamanos and P. Roussel – Chomaz,* ***Ann Phys. Fr. 21****, 601 (1996).*
74. *W. D. Myers,* ***Nucl. Phys. A 204****, 465 (1973).*
75. *G. Bertsch et al.,* ***Nucl. Phys. A 284****, 399 (1977).*
76. *M. E. Cage et al,* ***Nucl. Phys. A 201****, 418 (1973).*

77. *C. Tenreiro et al.,* ***Phys. Rev. C 53****, 2870 (1996).*
78. *A. Zerwekh et al.,* ***Phys. Rev. C 58****, 3445 (1998).*
79. *J. G. Cramer and R. M. De Vries,* ***Phys. Rev. C 22****, 91 (1980).*
80. *I. Strojek, private communication.*
81. *W. R. Leo, Techniques for Nuclear and Particle Physics Experiments, Springer – Verlag, 2rd ed., 1994.*
82. *Glenn F. Knoll, Radiation Detection and Measurement, John Wiley & Sons, Inc., 3rd ed., 1999.*
83. *K. Kleinknecht, Detectors for particle radiation, Cambridge University Press, 2rd ed., 1998*
84. *A. Trzcinska, private communication.*
85. *Application software group, Computer and Networks Division, CERN Program Library, PAW-Physics Analysis Workstation, CERN, Geneva, 1995*
86. *O. B. Tarasov, D. Bazin,* ***NIM B. 266****, 4657 (2008).*
87. *V.I. Zagrebaev et al., OM code of NRV, http://nrv.jinr.ru/nrv/.*

Appendix

A. Error calculation of σ/σ_{Ruth} ratio

Define as: $X = \sigma/\sigma_{Ruth}$.

Also:

$$\frac{\sigma}{\sigma_{Ruth}} = \frac{N\Omega_m}{N_m\Omega} \tag{A.1}$$

where

N is the number of counts of each single detector or telescope,

N_m is the number of counts of monitor,

Ω is the solid angle of each single detector or telescope and

Ω_m is the solid angle of the monitor

So the error is given by the formula:

$$\sigma_{\sigma/\sigma_{Ruth}} = \sigma_X = \left[\left(\frac{\partial X}{\partial N}\sigma_N\right)^2 + \left(\frac{\partial X}{\partial N_m}\sigma_{N_m}\right)^2 + \left(\frac{\partial X}{\partial \Omega}\sigma_\Omega\right)^2 + \left(\frac{\partial X}{\partial \Omega_m}\sigma_{\Omega_m}\right)^2\right]^{1/2} \tag{A.2}$$

$$= \left[\left(\frac{\Omega_m\sigma_N}{N_m\Omega}\right)^2 + \left(\frac{N\Omega_m\sigma_{N_m}}{N_m^2\Omega}\right)^2 + \left(\frac{N\Omega_m\sigma_\Omega}{N_m\Omega^2}\right)^2 + \left(\frac{N\sigma_{\Omega_m}}{N_m\Omega}\right)^2\right]^{1/2} =$$

$$= \left[\frac{\Omega_m^2\sigma_N^2}{N_m^2\Omega^2} + \frac{\Omega_m^2N^2\sigma_{N_m}^2}{N_m^4\Omega^2} + \frac{\Omega_m^2N^2\sigma_\Omega^2}{N_m^2\Omega^4} + \frac{N^2\sigma_{\Omega_m}^2}{N_m^2\Omega^2}\right]^{1/2} =$$

$$= \frac{N\Omega_m}{N_m\Omega}\left(\frac{\sigma_N^2}{N^2} + \frac{\sigma_{N_m}^2}{N_m^2} + \frac{\sigma_\Omega^2}{\Omega^2} + \frac{\sigma_{\Omega_m}^2}{\Omega_m^2}\right)^{1/2} \Rightarrow$$

$$\Rightarrow \sigma_X = X\left(\frac{\sigma_N^2}{N^2} + \frac{\sigma_{N_m}^2}{N_m^2} + \frac{\sigma_\Omega^2}{\Omega^2} + \frac{\sigma_{\Omega_m}^2}{\Omega_m^2}\right)^{1/2} \tag{A.3}$$

However,

$$\sigma_N^2 = \left(\sqrt{N}\right)^2 = N \tag{A.4}$$

and

$$\sigma_{N_m}^2 = \left(\sqrt{N_m}\right)^2 = N_m \tag{A.5}$$

Therefore:

$$\sigma_X = X\left(\frac{1}{N} + \frac{1}{N_m} + \frac{\sigma_\Omega^2}{\Omega^2} + \frac{\sigma_{\Omega_m}^2}{\Omega_m^2}\right)^{1/2} \tag{A.6}$$

On the other hand, the solid angle Ω is calculated from alphas radiation formula:

$$\Omega = \frac{4\pi \mathrm{N}_\alpha}{Rt} \tag{A.7}$$

where:

N_α is the counts from α source (Americium),

R is the radioactivity of alphas source (40kBq) and

t is the record time

The most important errors in this formula are introduced from the N_α (statistic error = $\sigma_\alpha = \mathrm{N}_\alpha^{1/2}$) and from the time ($\sigma_t$=±30sec).

So,

$$\sigma_\Omega = \left[\left(\frac{\partial \Omega}{\partial \mathrm{N}_\alpha} \sigma_\alpha \right)^2 + \left(\frac{\partial \Omega}{\partial t} \sigma_t \right)^2 \right]^{1/2} \tag{A.8}$$

that leads to:

$$\sigma_\Omega = \left[\left(\frac{4\pi}{Rt} \sigma_\alpha \right)^2 + \left(\frac{4\pi \mathrm{N}_\alpha}{Rt^2} \sigma_t \right)^2 \right]^{1/2} =$$

$$= \frac{4\pi}{Rt} \left[(\sigma_\alpha)^2 + \left(\frac{\mathrm{N}_\alpha}{t} \sigma_t \right)^2 \right]^{1/2} =$$

$$= \frac{4\pi}{Rt} \left[\mathrm{N}_\alpha + \frac{\mathrm{N}_\alpha^2}{t^2} \sigma_t^2 \right]^{1/2} = \frac{4\pi}{Rt} \left[\mathrm{N}_\alpha + \frac{\mathrm{N}_\alpha^2}{t^2} \sigma_t^2 \right]^{1/2} \Rightarrow$$

$$\Rightarrow \sigma_\Omega = \frac{4\pi}{Rt} \left[\mathrm{N}_\alpha \left(1 + \frac{\mathrm{N}_\alpha}{t^2} \sigma_t^2 \right) \right]^{1/2} \tag{A.9}$$

$$\frac{\sigma_\Omega^2}{\Omega^2} = \frac{\left(\frac{4\pi}{Rt} \left[\mathrm{N}_\alpha \left(1 + \frac{\mathrm{N}_\alpha}{t^2} \sigma_t^2 \right) \right]^{1/2} \right)^2}{\left(\frac{4\pi \mathrm{N}_\alpha}{Rt} \right)^2} = \frac{\mathrm{N}_\alpha \left(1 + \frac{\mathrm{N}_\alpha}{t^2} \sigma_t^2 \right)}{\mathrm{N}_\alpha^2} \Rightarrow$$

$$\Rightarrow \frac{\sigma_\Omega^2}{\Omega^2} = \frac{t^2 + \mathrm{N}_\alpha \sigma_t^2}{t^2 \mathrm{N}_\alpha} \tag{A.10}$$

In the same way, the last term of the expression (A.3) is given as:

$$\frac{\sigma_{\Omega_m}^2}{\Omega_m^2} = \frac{t_m{}^2 + \mathrm{N}_{\alpha m}\sigma_{tm}^2}{t_m{}^2 \mathrm{N}_{\alpha m}} \tag{A.11}$$

Finally:

$$\sigma_{\sigma/\sigma_{Ruth}} = \frac{\sigma}{\sigma_{Ruth}} \left[\frac{1}{N} + \frac{1}{\mathrm{N}_m} + \frac{t^2 + \mathrm{N}_\alpha \sigma_t^2}{t^2 \mathrm{N}_\alpha} + \frac{t_m{}^2 + \mathrm{N}_{\alpha m}\sigma_{tm}^2}{t_m{}^2 \mathrm{N}_{\alpha m}} \right]^{1/2} \tag{A.12}$$

B. Gate simulation for the solid angle calculation

The solid angle was also calculated by the program GATE[64-66]. GATE is a simulation toolkit based on Geant4 Monte Carlo simulation. We used the code presented below and the analysis was performed by the code PAW[85].

```
#  Solid angle calculation via GATE simulation
#  for Si and gas detectors
#  UOI, December 2012

#
# V I S U A L I S A T I O N
#

/vis/open OGLSX
/vis/viewer/reset
/vis/viewer/set/viewpointThetaPhi   60  60
/vis/viewer/zoom  2.5
/vis/viewer/set/style surface
/vis/drawVolume
/tracking/storeTrajectory 1
/vis/scene/endOfEventAction accumulate
/vis/viewer/update
/gate/geometry/enableAutoUpdate

#
# W O R L D
#

/gate/world/geometry/setXLength  100 cm
/gate/world/geometry/setYLength  100 cm
/gate/world/geometry/setZLength  100 cm

#
# Detector Volumes
#

/gate/world/daughters/name SPECThead
/gate/world/daughters/insert box
/gate/SPECThead/geometry/setXLength           100.00 cm
/gate/SPECThead/geometry/setYLength           100.00 cm
/gate/SPECThead/geometry/setZLength           100.00 cm
/gate/SPECThead/placement/setTranslation    0.00  0.00  0.00 cm
/gate/SPECThead/setMaterial Vacuum
/gate/SPECThead/vis/setColor magenta
/gate/SPECThead/vis/forceWireframe


/gate/SPECThead/daughters/name mask
/gate/SPECThead/daughters/insert cylinder
/gate/mask/geometry/setRmin             0.00 cm
/gate/mask/geometry/setRmax            10.00 cm
/gate/mask/geometry/setHeight           0.50 cm
/gate/mask/placement/setTranslation   0.00  0.00 -10.50 cm
/gate/mask/setMaterial Aluminium
/gate/mask/vis/setColor grey
/gate/mask/vis/forceSolid
```

```
/gate/mask/daughters/name hole
/gate/mask/daughters/insert box
/gate/hole/geometry/setXLength             3.50 mm
/gate/hole/geometry/setYLength            10.50 mm
/gate/hole/geometry/setZLength             0.55 cm
/gate/hole/placement/setTranslation   0.00  0.00   0.00 cm
/gate/hole/setMaterial Vacuum
/gate/hole/vis/setColor magenta
/gate/hole/vis/forceWireframe


/gate/SPECThead/daughters/name tel
/gate/SPECThead/daughters/insert cylinder
/gate/tel/geometry/setRmin              00.00 cm
/gate/tel/geometry/setRmax              10.00 cm
/gate/tel/geometry/setHeight            20.00 cm
/gate/tel/placement/setTranslation    0.00  0.00  0.00 cm
/gate/tel/setMaterial Vacuum
/gate/tel/vis/setColor red
/gate/tel/vis/forceWireframe

/gate/tel/daughters/name myl1
/gate/tel/daughters/insert box
/gate/myl1/geometry/setXLength            5.00 cm
/gate/myl1/geometry/setYLength            5.00 cm
/gate/myl1/geometry/setZLength            2.50 um
/gate/myl1/placement/setTranslation   0.00  0.00   -9.90 cm
/gate/myl1/setMaterial Mylar
/gate/myl1/vis/setColor blue
/gate/myl1/vis/forceSolid

#/gate/tel/daughters/name gas
#/gate/tel/daughters/insert cylinder
#/gate/gas/geometry/setRmin               0.00 cm
#/gate/gas/geometry/setRmax               1.00 cm
#/gate/gas/geometry/setHeight             4.70 cm
#/gate/gas/placement/setTranslation   0.00  0.00   -7.50 cm
#/gate/gas/setMaterial Butane15mbar
#/gate/gas/vis/setColor yellow
#/gate/gas/vis/forceSolid

/gate/tel/daughters/name Det1
/gate/tel/daughters/insert cylinder
/gate/Det1/geometry/setRmin             0.00 cm
/gate/Det1/geometry/setRmax             1.00 cm
/gate/Det1/geometry/setHeight           0.50 mm
/gate/Det1/placement/setTranslation   0.00  0.00  -5.10 cm
/gate/Det1/setMaterial Silicon
/gate/Det1/vis/setColor green
/gate/Det1/vis/forceSolid

#/gate/tel/daughters/name single
#/gate/tel/daughters/insert cylinder
#/gate/single/geometry/setRmin           0.00 cm
#/gate/single/geometry/setRmax           1.00 cm
#/gate/single/geometry/setHeight         0.04 mm
#/gate/single/placement/setTranslation   0.00  0.00  -7.10 cm
#/gate/single/setMaterial Silicon
#/gate/single/vis/setColor green
#/gate/single/vis/forceSolid
```

```
#------------------ooooooOOOOOOOOOOOOOOOOooooo--------------------#
#                                                                  #
#             S E N S I T I V E   D E T E C T O R                  #
#                                                                  #
#                                                                  #
#------------------ooooooOOOOOOOOOOOOOOOOooooo--------------------#

#
# Crystal SD
#

/gate/systems/SPECThead/crystal/attach tel
#/gate/gas/attachCrystalSD
/gate/Det1/attachCrystalSD
#/gate/single/attachCrystalSD

#
# Phantom SD
#
# /gate/P0/attachPhantomSD
# /gate/P1/attachPhantomSD
# /gate/P2/attachPhantomSD
# /gate/Collimator/attachPhantomSD


#------------------ooooooOOOOOOOOOOOOOOOOooooo--------------------#
#                                                                  #
#     D E F I N I T I O N   A N D   D E S C R I T I O N            #
#           O F   Y O U R   P H Y S I C S                          #
#                                                                  #
#------------------ooooooOOOOOOOOOOOOOOOOooooo--------------------#

#       EM  P R O C E S S

#/gate/physics/gamma/selectRayleigh lowenergy
#/gate/physics/gamma/selectPhotoelectric lowenergy
#/gate/physics/gamma/selectCompton lowenergy

#I N A C T I V E   S E C O N D A R Y   E L E C T R O N S

# /gate/physics/setElectronCut 100 m


#I N A C T I V E   X - R A Y S

# /gate/physics/setXRayCut 1. GeV
# /gate/physics/setDeltaRayCut 1. GeV


#------------------ooooooOOOOOOOOOOOOOOOOooooo--------------------#
#                                                                  #
#     I N I T I A L I Z A T I O N   O F   Y O U R                  #
#               S I M U L A T I O N                                #
#                                                                  #
#------------------ooooooOOOOOOOOOOOOOOOOooooo--------------------#


/gate/geometry/enableAutoUpdate
/run/initialize
```

```
#------------------ooooooOOOOOOOOOOOOOOOOooooo--------------------#
#                                                                  #
#  D E F I N I T I O N   O F   Y O U R   A C Q U I S I T I O N    #
#  D I G I T I Z E R   &   C O I N C I D E N C E   S H O R T E R  #
#                                                                  #
#------------------ooooooOOOOOOOOOOOOOOOOooooo--------------------#

/gate/output/digi/enable


#A D D E R
/gate/digitizer/Singles/insert adder

#       R E A D O U T
# /gate/digitizer/Singles/insert readout
# /gate/digitizer/Singles/readout/setDepth 1


#      E N E R G Y   B L U R R I N G
/gate/digitizer/Singles/insert blurring
/gate/digitizer/Singles/blurring/setResolution 0.075
/gate/digitizer/Singles/blurring/setEnergyOfReference 662. keV


#       E N E R G Y   C U T
# /gate/digitizer/Singles/insert thresholder
# /gate/digitizer/Singles/thresholder/setThreshold 50. keV
# /gate/digitizer/Singles/insert upholder
# /gate/digitizer/Singles/upholder/setUphold 250. keV



#------------------ooooooOOOOOOOOOOOOOOOOooooo--------------------#
#                                                                  #
#                  D E F I N I T I O N   O F                       #
#               Y O U R   O U T P U T   F I L E                    #
#                                                                  #
#------------------ooooooOOOOOOOOOOOOOOOOooooo--------------------#

/gate/output/analysis/enable
/gate/output/ascii/enable
/gate/output/root/disable
/gate/output/projection/disable
/gate/output/interfile/disable

# /gate/output/sinogram/disable
# /gate/output/ecat7/disable
# /gate/output/lmf1/disable

#       C H A N G E    T H E     S E E D (1)  O R   N O T (0)
# /gate/output/root/setSaveRndmFlag 1

#       S E T U P  - R O O T  F I L E
# /gate/output/root/setFileName YourSPECTSimu
# /gate/output/root/setRootSinglesAdderFlag 0
# /gate/output/root/setRootSinglesBlurringFlag 0
# /gate/output/root/setRootSinglesThresholderFlag 0
# /gate/output/root/setRootSinglesUpholderFlag 0
```

```
#       S E T U P  - A S C I I  F I L E
# /gate/output/ascii/setOutFileSinglesAdderFlag 0
# /gate/output/ascii/setOutFileSinglesBlurringFlag 0
# /gate/output/ascii/setOutFileSinglesThresholderFlag 0
# /gate/output/ascii/setOutFileSinglesUpholderFlag 0
/gate/output/ascii/setOutFileSinglesFlag 1
/gate/output/ascii/setOutFileHitsFlag 1

#       I N T E R F I L E   P R O J E C T I O N
# /gate/output/projection/pixelSizeX 0.904 mm
# /gate/output/projection/pixelSizeY 0.904 mm
# /gate/output/projection/pixelNumberX 128
# /gate/output/projection/pixelNumberY 128
# Specify the projection plane (XY, YZ or ZX)
# /gate/output/projection/projectionPlane YZ

#-------------------oooooOOOOOOOOOOOOOOOooooo--------------------#
#                                                                 #
#                  D E F I N I T I O N   O F                      #
#            Y O U R   V E R B O S I T Y   L E V E L              #
#                                                                 #
#-------------------oooooOOOOOOOOOOOOOOOooooo--------------------#

/control/verbose 0
#/grdm/verbose 0
/run/verbose 0
/event/verbose 0
/tracking/verbose 0
/gate/application/verbose 0
/gate/generator/verbose 0
/gate/stacking/verbose 0
/gate/event/verbose 0
/gate/source/verbose 0

#-------------------oooooOOOOOOOOOOOOOOOooooo--------------------#
#                                                                 #
#                  D E F I N I T I O N   O F                      #
#                   Y O U R   S O U R C E S                       #
#                                                                 #
#-------------------oooooOOOOOOOOOOOOOOOooooo--------------------#

#          ALPHA SOURCE
/gate/source/addSource Am
/gate/source/Am/gps/type Volume
/gate/source/Am/gps/shape Cylinder
/gate/source/Am/gps/radius   0.15 cm
/gate/source/Am/gps/halfz   0.05 mm
/gate/source/Am/gps/centre   0.00  0.00   -21.75 cm
/gate/source/Am/gps/angtype iso
/gate/source/Am/setActivity  40000. Bq
/gate/source/Am/gps/particle ion
/gate/source/Am/gps/ion 2 4 2 0.0
/gate/source/Am/gps/energytype Mono
/gate/source/Am/gps/energy     5.486 MeV
/gate/source/Am/gps/mintheta   0. deg
/gate/source/Am/gps/maxtheta 180. deg
/gate/source/Am/gps/minphi     0. deg
/gate/source/Am/gps/maxphi   360. deg
```

```
#-------------------ooooooOOOOOOOOOOOOOOOooooo---------------------#
#                                                                   #
#              S T A R T   A C Q U I S I T I O N                    #
#                T I M E   P A R A M E T E R S                      #
#                                                                   #
#-------------------ooooooOOOOOOOOOOOOOOOooooo---------------------#


#
#       E X P E R I M E N T
#

#/random/setSavingFlag  0
#/random/resetEngineFrom currentEvent.rndm

/gate/application/setTimeSlice    10.00  s
/gate/application/setTimeStart     0.00  s
/gate/application/setTimeStop    840.00  s

/gate/application/startDAQ

#-----------#
#  E X I T  #
#-----------#

exit
```

C. Theoretical analysis with ECIS

As it was mentioned, the experimental results were compared with phenomenological calculations performed with the code ECIS (Equations Couplées en Itérations Séquentielles)[67]. In particular, we compared the elastic scattering data with optical model calculations using different Woods – Saxon potentials. In this case, the input file had the following form:

```
     ***20Ne+28Si elastic scattering  ***
FFFFFFTTFFFFFFFTFFFFTFFFFFFTFFttFFFFFFFFFtFFFFFFFF
TFFFFFFFFFFFFFFFFFFFtFFFFFFFFFFFFFFFFFFFFFFFFFFFF
    1 1000                    2
             22.
0.0000   +    52.30   0.00     20.000      28.00       140.00
0.00      5.000     180.00000
    1    3
f 19    1    1
  34.16000   1.00000   0.10000
  42.60000   1.29630   0.12963
  45.96000   1.13538   0.11354
  50.96000   1.09794   0.10979
  55.94000   0.76627   0.07663
  59.23000   0.70319   0.07032
  62.51000   0.31247   0.03125
  67.38000   0.22591   0.02259
  75.39000   0.12456   0.01246
  78.55000   0.08614   0.00861
  83.23000   0.06251   0.00625
  90.87000   0.02888   0.00289
  93.86000   0.02430   0.00243
  98.27000   0.02282   0.00228
 101.16000   0.03514   0.00351
 105.40000   0.01729   0.00173
 108.17000   0.00165   0.00016
 112.22000   0.00885   0.00089
 118.68000   0.00287   0.00029
  0.001      0.001     0.001
 36   38   39
    1    1    0
    1    1    0    1    0    0    0   -1   -1
 52.77         1.023     0.816
    1    1    0    2    0    0    0   -1   -1
 1.458         1.403     0.198
    1    1    0    3    0    0    0   -1
  0.           0.000     0.000
    1    1    0    4    0    0    0   -1
 0.00          0.000     0.
    1    1    0    7    0    0    0   -1   -1
 140.          1.20       .000
FIN
//
```

The explanation of each important number is giving at the following file with the red index. An extended explanation is giving at the output file.

```
     ***20Ne+28Si elastic scattering  ***
FFFFFFFTTFFFFFFFTFFFFTFFFFFFFTFFttFFFFFFFFFtFFFFFFFF
TFFFFFFFFFFFFFFFFFFFtFFFFFFFFFFFFFFFFFFFFFFFFFFFFF
    1 1000                    2
              22.
0.0000    +     52.30[1]    0.00      20.000[2]      28.00[3]       140.00[4]
0.00[5]       5.000[6]      180.00000[7]
    1     3[8]
F[9] 19[10]     1     1
  34.16000[11a] 1.00000[11b] 0.10000[11c]
  42.60000    1.29630    0.12963
  45.96000    1.13538    0.11354
  50.96000    1.09794    0.10979
  55.94000    0.76627    0.07663
  59.23000    0.70319    0.07032
  62.51000    0.31247    0.03125
  67.38000    0.22591    0.02259
  75.39000    0.12456    0.01246
  78.55000    0.08614    0.00861
  83.23000    0.06251    0.00625
  90.87000    0.02888    0.00289
  93.86000    0.02430    0.00243
  98.27000    0.02282    0.00228
 101.16000    0.03514    0.00351
 105.40000    0.01729    0.00173
 108.17000    0.00165    0.00016
 112.22000    0.00885    0.00089
 118.68000    0.00287    0.00029
  0.001[12a]        0.001[12b]      0.001[12c]
 36[13a]    38[13b]    39[13c]
    1     1     0
    1     1     0     1[14a]     0     0     0    -1    -1[15a]
 52.77[16]          1.023[17]    0.816[18]
    1     1     0     2[14b]     0     0     0    -1    -1[15b]
 1.458              1.403      0.198
    1     1     0     3[14c]     0     0     0    -1
  0.                0.000      0.000
    1     1     0     4[14d]     0     0     0    -1
 0.00               0.000      0.
    1     1     0     7[14e]     0     0     0    -1    -1
 140.[4]            1.20[19]      .000
FIN
//
```

1. Energy of the projectile.
2. Mass of the projectile (M_P).
3. Mass of the target (M_T).
4. Z_P*Z_T , where Z_P and Z_T are the atomic number of the projectile and the target, respectively.

5. Minimum angle – theta (deg).
6. Step of the angle (deg).
7. Maximum angle – theta (deg).
8. Number of the parameters which change by the ECIS.
9. The program take into account the error [11c].
10. Number of data points.
11. Angle, σ/σ_{Ruth} and error at the σ/σ_{Ruth} ratio.
12. The step at the change of each parameter. As it was mentioned at 8, in this case the ECIS change only three parameters.
13. With these numbers the code identify which are the not fixed parameters. Further information are provided at the output file.
14. With these numbers the code, we define the potential type:
    1 Real volume
    2 Imaginary volume
    3 Real Surface
    4 Imaginary Surface
    7 Coulomb
15. We don't write anything when we put the whole radius at 17: $R = R_0\left(A_P^{1/3} + A_T^{1/3}\right)$, where A_P and A_T are the atomic masses of the projectile and the target, respectively. On the other hand, we write "-1" when we want to put the R_0. Then, the ECIS calculates the R itself.
16. Depth of the Woods – Saxon potential.
17. Radius R or R_0 of the Woods – Saxon potential (further information at 15).
18. Diffusivity of the Woods – Saxon potential.
19. $Z_P * Z_T$ (see also 4).
20. Coulomb radius r_C.

Tables

***Table T2.1a**: Calibration of platform A (Table from I. Strojek – private contact).*

Platform A **15 October 2011**

deg	unit
0.0	409.60
1.0	408.61
2.0	407.62
3.0	406.62
4.0	405.63
5.0	404.64
6.0	403.64
7.0	402.65
8.0	401.66
9.0	400.67
10.0	399.67
11.0	398.68
12.0	397.69
13.0	396.69
14.0	395.70
15.0	394.71
16.0	393.72
17.0	392.72
18.0	391.73
19.0	390.74
20.0	389.75
21.0	388.75
22.0	387.76
23.0	386.77
24.0	385.77
25.0	384.78
26.0	383.79
27.0	382.80
28.0	381.80
29.0	380.81
30.0	379.82
31.0	378.82
32.0	377.83
33.0	376.84
34.0	375.85
35.0	374.85
36.0	373.86
37.0	372.87
38.0	371.87
39.0	370.88
40.0	369.89
41.0	368.90
42.0	367.90
43.0	366.91
44.0	365.92
45.0	364.92
46.0	363.93
47.0	362.94
48.0	361.95
49.0	360.95
50.0	359.96
51.0	358.97
52.0	357.97
53.0	356.98
54.0	355.99
55.0	355.00
56.0	354.00
57.0	353.01
58.0	352.02
59.0	351.02
60.0	350.03
61.0	349.04
62.0	348.05
63.0	347.05
64.0	346.06
65.0	345.07
66.0	344.08
67.0	343.08
68.0	342.09
69.0	341.10
70.0	340.10
71.0	339.11
72.0	338.12
73.0	337.13
74.0	336.13
75.0	335.14
76.0	334.15
77.0	333.15
78.0	332.16
79.0	331.17
80.0	330.18
81.0	329.18
82.0	328.19
83.0	327.20
84.0	326.20
85.0	325.21
86.0	324.22
87.0	323.23
88.0	322.23
89.0	321.24
90.0	320.25
91.0	319.25
92.0	318.26
93.0	317.27
94.0	316.28
95.0	315.28
96.0	314.29
97.0	313.30
98.0	312.30
99.0	311.31
100.0	310.32
101.0	309.33
102.0	308.33
103.0	307.34
104.0	306.35
105.0	305.36
106.0	304.36
107.0	303.37
108.0	302.38
109.0	301.38
110.0	300.39
111.0	299.40
112.0	298.41
113.0	297.41
114.0	296.42
115.0	295.43
116.0	294.43
117.0	293.44
118.0	292.45
119.0	291.46
120.0	290.46
121.0	289.47
122.0	288.48
123.0	287.48
124.0	286.49
125.0	285.50
126.0	284.51
127.0	283.51
128.0	282.52
129.0	281.53
130.0	280.53
131.0	279.54
132.0	278.55
133.0	277.56
134.0	276.56
135.0	275.57
136.0	274.58
137.0	273.58
138.0	272.59
139.0	271.60
140.0	270.61
141.0	269.61
142.0	268.62
143.0	267.63
144.0	266.64
145.0	265.64
146.0	264.65
147.0	263.66
148.0	262.66
149.0	261.67
150.0	260.68
151.0	259.69
152.0	258.69
153.0	257.70
154.0	256.71
155.0	255.71
156.0	254.72
157.0	253.73
158.0	252.74
159.0	251.74
160.0	250.75
161.0	249.76
162.0	248.76
163.0	247.77
164.0	246.78
165.0	245.79
166.0	244.79
167.0	243.80
168.0	242.81
169.0	241.81
170.0	240.82
171.0	239.83
172.0	238.84
173.0	237.84
174.0	236.85
175.0	235.86
176.0	234.86
177.0	233.87
178.0	232.88
179.0	231.89
180.0	230.89

Table T2.1b: *Calibration of platform B (Table from I. Strojek – private contact).*

Platform B **15 October 2011**

deg	unit
0.0	766.14
1.0	767.14
2.0	768.13
3.0	769.13
4.0	770.13
5.0	771.12
6.0	772.12
7.0	773.12
8.0	774.11
9.0	775.11
10.0	776.11
11.0	777.10
12.0	778.10
13.0	779.10
14.0	780.09
15.0	781.09
16.0	782.09
17.0	783.08
18.0	784.08
19.0	785.08
20.0	786.07
21.0	787.07
22.0	788.07
23.0	789.06
24.0	790.06
25.0	791.06
26.0	792.06
27.0	793.05
28.0	794.05
29.0	795.05
30.0	796.04
31.0	797.04
32.0	798.04
33.0	799.03
34.0	800.03
35.0	801.03
36.0	802.02
37.0	803.02
38.0	804.02
39.0	805.01
40.0	806.01
41.0	807.01
42.0	808.00
43.0	809.00
44.0	810.00
45.0	810.99
46.0	811.99
47.0	812.99
48.0	813.98
49.0	814.98
50.0	815.98
51.0	816.97
52.0	817.97
53.0	818.97
54.0	819.97
55.0	820.96
56.0	821.96
57.0	822.96
58.0	823.95
59.0	824.95
60.0	825.95
61.0	826.94
62.0	827.94
63.0	828.94
64.0	829.93
65.0	830.93
66.0	831.93
67.0	832.92
68.0	833.92
69.0	834.92
70.0	835.91
71.0	836.91
72.0	837.91
73.0	838.90
74.0	839.90
75.0	840.90
76.0	841.89
77.0	842.89
78.0	843.89
79.0	844.88
80.0	845.88
81.0	846.88
82.0	847.87
83.0	848.87
84.0	849.87
85.0	850.87
86.0	851.86
87.0	852.86
88.0	853.86
89.0	854.85
90.0	855.85
91.0	856.85
92.0	857.84
93.0	858.84
94.0	859.84
95.0	860.83
96.0	861.83
97.0	862.83
98.0	863.82
99.0	864.82
100.0	865.82
101.0	866.81
102.0	867.81
103.0	868.81
104.0	869.80
105.0	870.80
106.0	871.80
107.0	872.79
108.0	873.79
109.0	874.79
110.0	875.78
111.0	876.78
112.0	877.78
113.0	878.78
114.0	879.77
115.0	880.77
116.0	881.77
117.0	882.76
118.0	883.76
119.0	884.76
120.0	885.75
121.0	886.75
122.0	887.75
123.0	888.74
124.0	889.74
125.0	890.74
126.0	891.73
127.0	892.73
128.0	893.73
129.0	894.72
130.0	895.72
131.0	896.72
132.0	897.71
133.0	898.71
134.0	899.71
135.0	900.70
136.0	901.70
137.0	902.70
138.0	903.69
139.0	904.69
140.0	905.69
141.0	906.69
142.0	907.68
143.0	908.68
144.0	909.68
145.0	910.67
146.0	911.67
147.0	912.67
148.0	913.66
149.0	914.66
150.0	915.66
151.0	916.65
152.0	917.65
153.0	918.65
154.0	919.64
155.0	920.64
156.0	921.64
157.0	922.63
158.0	923.63
159.0	924.63
160.0	925.62
161.0	926.62
162.0	927.62
163.0	928.61
164.0	929.61
165.0	930.61
166.0	931.60
167.0	932.60
168.0	933.60
169.0	934.60
170.0	935.59
171.0	936.59
172.0	937.59
173.0	938.58
174.0	939.58
175.0	940.58
176.0	941.57
177.0	942.57
178.0	943.57
179.0	944.56
180.0	945.56

***Table T3.1**: Pulser and alphas peaks used in energy calibration.*

Detector	M1	M2	S1	S2	S3	S4	S5	S6	S7	T1-Si	T2-Si
Pulser	**Channel**										
0.1		133	105	115	114					99.6	107
0.2	252	260	205	227	223				223	195.87	210
0.3	376	390	306	340	331			346	331	292	314
0.4	498	516	405	453	442		359	459	440	388	417
0.5	621	644	506	564	552	523	449	573	549	483	520
0.6	744	771	606	677	660	627	538	686	658	580	623
0.7	866	897	706	788	769	731	627	799	767	675	726
0.8	989	1025	807	900	878	835	717	912	875	771	828
0.9	1112	1151	906	1012	987	939	806	1025	984	866	931
1.0	1235	1279	1006	1124	1096	1044	896	1138	1093	962	1034
2.0	2459	2545	2004	2242	2184	2083	1789	2267	2181	1917	2061
3.0	3683	3810	3003	3359	3272	3122	2681	3397	3268	2871	3089
4.0	4909	5074	4002	4476	4359	4162	3573	4527	4356	3825	4117
5.0	6134	6338	5001	5593	5447	5201	4466	5658	5444	4779	5146
6.0			6000	6708	6533	6240	5377	6789	6532	5733	6175
7.0										6688	7204
Alpha peak	300	316.7	247	262	266	246	224	254	246.5	218	234

Detector	T3-Si
Pulser	**Channel**
0.1	100
0.15	150
0.2	198
0.3	294
0.4	393
0.5	490
0.6	587
0.7	684
0.8	780
0.9	878
1.0	976
2.0	1944
3.0	2913
4.0	3883
5.0	4852
6.0	5824
7.0	6796
Alpha peak	210

Detector	T1-gas	T2-gas	T3-gas
Pulser	**Channel**		
0.03	840	774	873
0.04		1015	
0.05	1390	1242	1438
0.07	1936	1773	2004
0.1	2767	2544	2865
0.15	4110	3807	4287
0.2	5487	5068	5711
0.25	6836	6325	7130
0.3	8163	7575	
Alpha peak	342	330	358

***Table T3.2**: The relation between pulser and channel.*

Detector or Telescope	(pulser) = $A_0 + A_1X + A_2X^2 + A_3X^3 + A_4X^4 + A_5X^5$, where X=channel						α-peak (channel)	α-peak (pulser)
	A_0	**A_1**	**A_2**	**A_3**	A_4	**A_5**		
M1	-5.270E-03	8.132E-04	4.692E-10	5.253E-13	-1.739E-16	1.433E-20	300	0.238741
M2	-3.720E-03	7.790E-04	7.094E-09	-2.229E-12	3.404E-16	-1.956E-20	316.7	0.243626
S1	-4.150E-03	9.936E-04	6.534E-09	-2.313E-12	3.616E-16	-2.076E-20	247	0.241627
S2	-2.330E-03	8.885E-04	3.754E-09	-9.742E-13	1.146E-16	-4.757E-21	262	0.230694
S3	-3.790E-03	9.129E-04	3.474E-09	-8.064E-13	8.052E-17	-2.530E-21	266	0.239264
S4	-5.583E-04	9.555E-04	4.634E-09	-1.454E-12	2.081E-16	-1.101E-20	246	0.234742
S5	-3.818E-05	1.110E-03	9.091E-09	-4.860E-12	1.239E-15	-1.155E-20	224	0.249006
S6	-4.730E-03	8.793E-04	4.483E-09	-1.383E-12	1.861E-16	-9.276E-21	254	0.218872
S7	-4.810E-03	9.200E-04	-1.117E-09	5.553E-13	-1.050E-16	6.671E-21	246.5	0.221916
T1-Si	-3.810E-03	1.040E-03	5.038E-09	-1.449E-12	2.010E-16	-1.076E-20	218	0.223135
T2-Si	-3.710E-03	9.670E-04	4.849E-09	-1.525E-12	2.028E-16	-9.798E-21	234	0.222816
T3-Si	-3.120E-03	1.030E-03	3.842E-09	-1.030E-12	1.223E-16	-5.758E-21	210	0.21334
T1-gas	1.240E-04	3.520E-05	5.694E-10	-8.154E-14	2.239E-18	2.487E-22	342	0.012226
T2-gas	-5.920E-03	5.141E-05	-7.848E-09	2.200E-12	-2.757E-16	1.277E-20	330	0.010267
T3-gas	-2.230E-03	3.822E-05	-1.954E-09	5.463E-13	-7.042E-17	3.414E-21	358	0.011228

Table T3.3: *The relation between energy and channel assuming that energy is a linear function of the channel.*

Detector or Telescope	(Energy) = A*(channel) + B	
	A	B
M1	0.01876	-0.16025
M2	0.01779	-0.18490
S1	0.02273	-0.14320
S2	0.02128	-0.11858
S3	0.02107	-0.14598
S4	0.02248	-0.08169
S5	0.02463	-0.01486
S6	0.02218	-0.16673
S7	0.02273	-0.11596
T1-Si	0.02360	-0.14988
T2-Si	0.02194	-0.11551
T3-Si	0.02429	-0.10452
T1-gas	0.00139	-0.05128
T2-gas	0.00177	-0.01067
T3-gas	0.00144	-0.02364

***Table T3.4a**: Determination of cross section for the elastic scattering $^{20}Ne + ^{28}Si$ at energy of 52.3 MeV – SIDE A.*

θ_{lab} [deg]	θ_{cm} [deg]	Detector & run	DΦ	$N_{monitor}$ [counts]	N [counts]	Ω [sr]	σ [mb]	σ_{Ruth} [mb]	σ/σ_{Ruth}	error	error %	Target
20.00	**34.17**	M1	442063.89	562830	562830	1.247E-04	10210	10210	**1.00000**	0.07880	7.88%	vertical 200μg/cm^2
25.00	**42.60**	T1 [run139]	36420.42	46370	416100	2.105E-03	5429	4223	**1.28550**	0.07642	5.94%	vertical 200μg/cm^2
40.00	**67.38**	T1 [run154]	15472.98	19700	7200	2.105E-03	221.1	668	**0.33100**	0.02013	6.08%	vertical 200μg/cm^2
45.00	**75.39**	T1 [run155]	16729.67	21300	2500	2.105E-03	71.01	423	**0.16786**	0.01056	6.29%	vertical 200μg/cm^2
50.00	**83.23**	T1 [run156]	19753.58	25150	1148	2.105E-03	27.61	282	**0.09792**	0.00651	6.65%	vertical 200μg/cm^2
55.00	**90.87**	T1 [run157]	17892.11	22780	284	2.105E-03	7.542	195	**0.03868**	0.00325	8.41%	vertical 200μg/cm^2
60.00	**98.27**	T1 [run140]	43740.63	55690	340	2.105E-03	3.693	138.5	**0.02667**	0.00214	8.04%	vertical 200μg/cm^2
62.00	**101.16**	T1 [run158]	21002.41	26740	189	2.105E-03	4.276	121.7	**0.03514**	0.00330	9.40%	vertical 200μg/cm^2
65.00	**105.40**	T1 [run141,146,149]	271052.09	345100	994	2.105E-03	1.743	101.1	**0.01724**	0.00116	6.72%	vertical 200μg/cm^2
20.00	**34.17**	M1	157431.30	198280	198280	1.247E-04	10100	10100	**1.00000**	0.07883	7.88%	vertical 132μg/cm^2
25.00	**42.60**	T1 [run138]	3255.34	4100	37360	2.105E-03	5453	4150	**1.31403**	0.08080	6.15%	vertical 132μg/cm^2
30.00	**50.96**	T1 [run130,132]	75523.83	95120	356000	2.105E-03	2240	2040	**1.09794**	0.06517	5.94%	vertical 132μg/cm^2
35.00	**59.23**	T1 [run135,136]	78652.13	99060	129900	2.105E-03	784.8	1116	**0.70319**	0.04177	5.94%	vertical 132μg/cm^2
20.00	**34.17**	M1	921938.41	1173800	1173800	1.247E-04	10210	10210	**1.00000**	0.07878	7.88%	tilted by 30^o, 200μg/cm^2
27.00	**45.96**	T1 [run159,160]	200206.25	254900	1483000	2.105E-03	3520	3100	**1.13538**	0.06731	5.93%	tilted by 30^o, 200μg/cm^2
33.00	**55.94**	T1 [run161,162,163]	281576.86	358500	644800	2.105E-03	1088	1420	**0.76627**	0.04543	5.93%	tilted by 30^o, 200μg/cm^2

***Table T3.4b**: Determination of cross section for the elastic scattering $^{20}Ne + ^{28}Si$ at energy of 52.3 MeV – SIDE B*

θ_{lab} [deg]	θ_{cm} [deg]	Detector & run	DΦ	$N_{monitor}$ [counts]	N [counts]	Ω [sr]	σ [mb]	σ_{Ruth} [mb]	σ/σ_{Ruth}	error	error %	Target
20.00	**34.16**	M2	406438.66	476390	476390	1.148E-04	10210	10210	**1.00000**	0.08130	8.13%	vertical 200μg/cm^2
37.00	**62.51**	T2 [154-158]	82842.20	97100	52060	2.215E-03	283.7	908	**0.31247**	0.01979	6.33%	vertical 200μg/cm^2
40.00	**67.38**	T2 [139-140]	71230.64	83490	21560	2.215E-03	136.7	668	**0.20457**	0.01300	6.36%	vertical 200μg/cm^2
55.00	**90.87**	T2 [141,146,149]	252365.82	295800	3640	2.215E-03	6.512	195	**0.03339**	0.00218	6.53%	vertical 200μg/cm^2
57.00	**93.86**	T3 [154-158]	82842.20	97100	596	1.747E-03	4.118	169.5	**0.02430**	0.00196	8.05%	vertical 200μg/cm^2
60.00	**98.27**	T3 [139-140]	71230.64	83490	370	1.747E-03	2.973	138.5	**0.02147**	0.00186	8.66%	vertical 200μg/cm^2
75.00	**118.68**	T3 [149,141,146]	252365.82	295800	56	1.747E-03	0.127	56.85	**0.00223**	0.00034	15.05%	vertical 200μg/cm^2
20.00	**34.16**	M2	138820.85	160960	160960	1.148E-04	10100	10100	**1.00000**	0.08136	8.14%	vertical 132μg/cm^2
40.00	**67.38**	T2 [130,132,138]	70221.13	81420	20590	2.215E-03	132.4	665	**0.19907**	0.01266	6.36%	vertical 132μg/cm^2
45.00	**75.39**	T2 [135]	37413.32	43380	3660	2.215E-03	44.17	420	**0.10516**	0.00688	6.54%	vertical 132μg/cm^2
50.00	**83.23**	T2 [136]	31212.27	36190	1170	2.215E-03	16.92	279	**0.06066**	0.00423	6.97%	vertical 132μg/cm^2
60.00	**98.27**	T3 [130,132,138]	70221.13	81420	355	1.747E-03	2.894	137.3	**0.02108**	0.00184	8.73%	vertical 132μg/cm^2
65.00	**105.40**	T3 [135]	37413.32	43380	116	1.747E-03	1.775	100.2	**0.01771**	0.00205	11.59%	vertical 132μg/cm^2
70.00	**112.22**	T3 [136]	31522.75	36550	42	1.747E-03	0.763	75.6	**0.01009**	0.00171	16.92%	vertical 132μg/cm^2
20.00	**34.16**	M2	879270.51	1030600	1030600	1.148E-04	10210	10210	**1.00000**	0.08129	8.13%	tilted by 30^o, 200μg/cm^2
47.00	**78.55**	T2 [161,162,163]	270538.21	317100	18480	2.215E-03	30.84	358	**0.08614**	0.00548	6.36%	tilted by 30^o, 200μg/cm^2
50.00	**83.23**	T2 [159,160]	188549.18	221000	6596	2.215E-03	15.79	282	**0.05601**	0.00360	6.43%	tilted by 30^o, 200μg/cm^2
55.00	**90.87**	T2 [150-153]	420183.12	492500	4621	2.215E-03	4.965	195	**0.02546**	0.00165	6.48%	tilted by 30^o, 200μg/cm^2
70.00	**112.22**	T3 [159,160]	188549.18	221000	215	1.747E-03	0.653	75.6	**0.00863**	0.00084	9.72%	tilted by 30^o, 200μg/cm^2
75.00	**118.68**	T3 [150-153]	420183.12	492500	148	1.747E-03	0.202	56.85	**0.00355**	0.00038	10.75%	tilted by 30^o, 200μg/cm^2
67.00	**108.17**	T3 [161-163]	270538.21	317100	70	1.747E-03	0.148	89.8	**0.00165**	0.00023	13.81%	tilted by 30^o, 200μg/cm^2

***Table T3.5**: Determination of cross section for the elastic scattering $^{20}Ne + ^{28}Si$ at energy of 42.5 MeV, using perpendicular target 132 μg/cm^2.*

θ_{lab} [deg]	θ_{cm} [deg]	Detector & run	DΦ	$N_{monitor}$ [counts]	N [counts]	Ω [sr]	σ [mb]	σ_{Ruth} [mb]	σ/σ_{Ruth}	error	error %
20.00	**34.20**	M1	35097.76	67970	67970	1.247E-04	15530	15530	**1.00000**	0.07896	7.90%
25.00	**42.60**	T1 [run92,95,96]	3568.13	6910	51940	2.105E-03	6917	6390	**1.08244**	0.06561	6.06%
30.00	**51.00**	T1 [run97]	281.42	545	2019	2.105E-03	3409	3120	**1.09261**	0.08350	7.64%
35.00	**59.20**	T1 [run98]	594.86	1152	2414	2.105E-03	1928	1705	**1.13094**	0.07829	6.92%
40.00	**67.40**	T1 [run99]	1149.96	2227	2756	2.105E-03	1139	1015	**1.12195**	0.07376	6.57%
45.00	**75.38**	T1 [run100]	1524.84	2953	1937	2.105E-03	603.6	641	**0.94165**	0.06221	6.61%
50.00	**83.22**	T1 [run101]	1493.86	2893	1070	2.105E-03	340.3	427	**0.79705**	0.05517	6.92%
55.00	**90.86**	T1 [run102]	2416.62	4680	846	2.105E-03	166.3	295	**0.56387**	0.03950	7.00%
60.00	**98.26**	T1 [run103]	12083.09	23400	1792	2.105E-03	70.47	210	**0.33557**	0.02152	6.41%
65.00	**105.39**	T1 [run104]	11984.98	23210	652	2.105E-03	25.85	153.2	**0.16873**	0.01203	7.13%
20.00	**34.20**	M2	32549.12	58030	58030	1.148E-04	15530	15530	**1.00000**	0.08149	8.15%
45.00	**75.38**	T2 [run92, 95-98]	4225.83	7534	4719	2.215E-03	504.2	641	**0.78653**	0.05174	6.58%
50.00	**83.22**	T2 [run99-101]	3938.65	7022	2056	2.215E-03	235.7	427	**0.55193**	0.03748	6.79%
55.00	**90.86**	T2 [run102]	2212.20	3944	597	2.215E-03	121.8	295	**0.41301**	0.03175	7.69%
60.00	**98.26**	T2 [run103]	11206.81	19980	1728	2.215E-03	69.61	210	**0.33150**	0.02251	6.79%
65.00	**105.39**	T2 [run104]	10965.63	19550	592	2.215E-03	24.37	153.2	**0.15910**	0.01204	7.57%

***Table T3.6**: Determination of cross section for the elastic scattering $^{20}Ne + ^{28}Si$ at energy of 70.0 MeV.*

θlab [deg]	θcm [deg]	Detector & run	DΦ	Nmonitor [counts]	N [counts]	Ω [sr]	σ [mb]	σRuth [mb]	σ/σRuth	error	error %	Target
20.00	**34.16**	M1	1925375.62	1272500	1272500	1.247E-04	5300	5300	**1.000E+00**	0.07878	7.88%	vertical 200μg/cm^2
25.00	**42.60**	T1 [run182,183]	45785.36	30260	103200	2.105E-03	1071	2200	**4.868E-01**	0.02902	5.96%	vertical 200μg/cm^2
30.00	**50.96**	T1 [run184,185]	44196.64	29210	14890	2.105E-03	160.1	1074.5	**1.490E-01**	0.00895	6.01%	vertical 200μg/cm^2
35.00	**59.22**	T1 [run186,191]	137431.72	90830	8000	2.105E-03	27.66	587	**4.712E-02**	0.00285	6.04%	vertical 200μg/cm^2
40.00	**67.37**	T1 [run192]	79738.54	52700	1121	2.105E-03	6.680	349.5	**1.911E-02**	0.00127	6.65%	vertical 200μg/cm^2
45.00	**75.38**	T1 [run193,194]	169463.32	112000	620	2.105E-03	1.738	221	**7.866E-03**	0.00056	7.16%	vertical 200μg/cm^2
50.00	**83.22**	T1 [run195-197]	274318.74	181300	455	2.105E-03	0.788	187.5	**4.203E-03**	0.00032	7.56%	vertical 200μg/cm^2
55.00	**90.86**	T1 [run199,206]	1174441.30	776200	1270	2.105E-03	0.514	101.6	**5.057E-03**	0.00033	6.56%	vertical 200μg/cm^2
20.00	**34.16**	M2	1398330.16	850800	850800	1.148E-04	5300	5300	**1.000E+00**	8.129E-02	8.13%	vertical 200μg/cm^2
40.00	**67.38**	T2 [182-185]	65413.19	39800	600	2.215E-03	4.141	349.5	**1.185E-02**	8.926E-04	7.53%	vertical 200μg/cm^2
45.00	**75.39**	T2 [186,191-195]	302412.73	184000	1209	2.215E-03	1.805	221	**8.167E-03**	5.667E-04	6.94%	vertical 200μg/cm^2
50.00	**83.23**	T2 [196,197,199-206]	1030504.24	627000	1232	2.215E-03	0.540	187.2	**2.883E-03**	1.997E-04	6.93%	vertical 200μg/cm^2
60.00	**98.27**	T3 [182-185]	65413.19	39800	38	1.747E-03	0.264	72.35	**3.651E-03**	6.358E-04	17.41%	vertical 200μg/cm^2
65.00	**105.4**	T3 [186,191-195]	302412.73	184000	85	1.747E-03	0.128	52.85	**2.419E-03**	3.036E-04	12.55%	vertical 200μg/cm^2
70.00	**112.22**	T3 [196,197,199-206]	1030504.24	627000	84	1.747E-03	0.037	37.1	**9.991E-04**	1.259E-04	12.61%	vertical 200μg/cm^2
20.00	**34.16**	M2	2475018.08	1505900	1505900	1.148E-04	5300	5300	**1.000E+00**	8.129E-02	8.13%	tilted by 30^o, 200μg/cm^2
55.00	**90.87**	T2 [225-229]	492899.88	299900	517	2.215E-03	0.474	101.6	**4.661E-03**	3.586E-04	7.69%	tilted by 30^o, 200μg/cm^2
60.00	**98.27**	T2 [207-218]	1982118.20	1206000	1300	2.215E-03	0.296	72.35	**4.093E-03**	2.822E-04	6.89%	tilted by 30^o, 200μg/cm^2
75.00	**118.68**	T3 [225-229]	492899.88	299900	29	1.747E-03	0.027	29.65	**9.024E-04**	1.770E-04	19.61%	tilted by 30^o, 200μg/cm^2